THEORETICAL PERFORMANCE BOUNDS FOR ESTIMATION OF DROP SIZE DISTRIBUTION PARAMETERS AND RAIN RATE

A Dissertation
Presented to
The Academic Faculty

by

Jenny L. Reed

In Partial Fulfillment
of the Requirements for the Degree
Doctor of Philosophy in the
School of Electrical and Computer Engineering

Georgia Institute of Technology
December 2016

THEORETICAL PERFORMANCE BOUNDS FOR ESTIMATION OF DROP SIZE DISTRIBUTION PARAMETERS AND RAIN RATE

Approved by:

Dr. Aaron Lanterman, Advisor
School of ECE
Georgia Institute of Technology

Dr. Gregory Durgin
School of ECE
Georgia Institute of Technology

Dr. Mark Richards
School of ECE
Georgia Institute of Technology

Dr. Brani Vidakovic
School of ISyE
Georgia Institute of Technology

Dr. Douglas Williams
School of ECE
Georgia Institute of Technology

Date Approved: October 12, 2016

To my husband,

Jeremy Reed,

for putting up with me when no sane person would.

ACKNOWLEDGEMENTS

First, I would like to thank my advisor, Dr. Aaron Lanterman, for his guidance and enthusiasm throughout my doctoral studies. His support and advice have proven invaluable towards completing this dissertation. I would also like to thank my committee for their insight and support.

In addition, I would like to thank GTRI for supporting me in this endeavor, without which I may be another decade from graduating. I would also like to thank my supervisors and colleagues at GTRI that provided guidance and encouragement in the moments of frustration and exasperation that are inevitably encountered in such a pursuit.

I owe a deep debt of gratitude to my parents, Cathy and John Matthews, for their love, support, and encouragement, not just throughout my academic pursuits, but throughout my entire life. I would also like to thank my dogs, Marley and Marky, for their love, comfort, and loyalty, along with the desperately needed moments of levity they have provided through the years. Next, I'd like to thank Dylan Reed, my sweet son, who taught me that sleep is optional, and who brings an insurmountable joy to my life every time I see him smile. Lastly, I'd like to thank my husband, Jeremy Reed, who supported my decision to go back to school and pursue my PhD, despite the fact that he knew the time and effort it would require. Without all the love and support you have provided throughout these years, I would be far from where I am today.

TABLE OF CONTENTS

DEDICATION . . . . . **iii**

ACKNOWLEDGEMENTS . . . . . **iv**

LIST OF TABLES . . . . . **x**

LIST OF FIGURES . . . . . **xi**

SUMMARY . . . . . **xiii**

I INTRODUCTION **1**

1.1 Organization 2

1.2 DSD, Rain Rate, and LWC 3

1.2.1 Drop Size Distribution 3

1.2.2 Rain Rate 4

1.2.3 Liquid Water Content 5

II OPERATION AND PHENOMENOLOGY OF THE NEXRAD (WSR-88D) WEATHER RADAR **6**

2.1 Overview 6

2.2 Basic Radar Phenomenology 7

2.2.1 Range 7

2.2.2 Range Resolution 8

2.2.3 Cross-Range Resolution 8

2.2.4 Radar Range Equation 9

2.2.5 Thermal Noise 11

2.2.6 Doppler Frequency 12

2.2.7 Polarization 13

2.2.8 Attenuation 16

2.2.9 Clutter and Anomalous Propagation 17

2.3 Operation of the WSR-88D 18

2.3.1 Signal Processing Chain 18

2.3.2 Coordinate System and Propagation 19
2.3.3 Radar Parameters 20
2.3.4 Volume Coverage Patterns 23
2.3.5 Legacy Resolution versus Super Resolution 24
2.3.6 Dual-Polarization 25
2.4 Weather Radar Data Products 26
2.4.1 Reflectivity 27
2.4.2 Radial Velocity 29
2.4.3 Spectral Width 31
2.4.4 Differential Reflectivity 32
2.4.5 Co-polar Correlation Coefficient 34
2.4.6 Differential Phase 36
2.5 Dual-Pol Radar Parameters for Tornado Detection 38
2.6 Summary 39
III STATE OF THE FIELD 40
3.1 Overview 40
3.2 Raindrop Scattering Basics 40
3.3 DSD Parameter Estimation 41
3.3.1 Beta Method 41
3.3.2 Constrained-Gamma Method 42
3.3.3 Neural Network Approach 44
3.4 Evaluation of DSD Estimators 45
3.4.1 Data Merits 46
3.4.2 Measures of Estimator Performance 47
3.5 Rain Rate Estimation 48
3.5.1 DSD-Based Approaches 48
3.5.2 Non-DSD-Based Approaches 49
3.6 Evaluation of Rain Rate Estimators 51

3.7 Summary 51

IV MAPPING DSD PARAMETERS TO RADAR MEASUREMENTS 53

4.1 Overview 53

4.2 Scattering Properties of Individual Raindrops 54

4.3 Raindrop Shape Model 57

4.3.1 Mean Axis Ratio 58

4.3.2 Axis Ratio Distribution 59

4.3.3 Orientation 61

4.4 Scattering Properties of a Raindrop Ensemble 62

4.4.1 Reflectivity 62

4.4.2 Differential Reflectivity 63

4.4.3 Specific Differential Phase 63

4.4.4 Co-polar Correlation Coefficient 64

4.5 Proposed Mathematical Formulation 64

4.6 Coefficient Estimation 66

4.7 Results 68

4.8 Conclusions 70

4.9 Summary 71

V VARIANCE BOUNDS FOR ESTIMATION OF DSD PARAMETERS 72

5.1 Overview 72

5.2 Signal Model 72

5.2.1 Model for a Single Resolution Volume 72

5.2.2 Model for Multiple Resolution Volumes 74

5.2.3 Mapping DSD Parameters to Radar Measurements 75

5.3 Cramér-Rao Lower Bound of DSD Parameters 76

5.3.1 CRLB of P_h, P_v, ρ, and ϕ 77

5.3.2 CRLB of P_h, P_v, ρ, and Δ_ϕ 78

5.3.3 CRLB of η_h, η_v, ρ, and K_{DP} 79

5.3.4 CRLB of N_o, μ, and Λ 80
5.4 Maximum Likelihood Estimate 84
5.5 Results 86
5.5.1 Experimental Set-up 86
5.5.2 Eigenanalysis of CRLB and MLE 90
5.6 Summary 95

VI PARAMETRIC ANALYSIS OF VARIANCE BOUNDS AND MLE PROPERTIES FOR DSD PARAMETERS 96

6.1 Overview 96
6.2 Experimental Set-up 97
6.3 CRLB and MLE Analysis 98
6.4 CRLB for Different Raindrop Shape Models 102
6.5 Summary 106

VII VARIANCE BOUNDS FOR THE ESTIMATION OF RAIN RATE AND LWC 108

7.1 Overview 108
7.2 Cramér-Rao Lower Bounds 108
7.2.1 CRLB of Rain Rate 109
7.2.2 CRLB of Liquid Water Content 110
7.3 Experimental Set-up 111
7.4 CRLB and MLE Analysis 112
7.5 CRLB for Different Raindrop Shape Models 116
7.6 Analysis of Results 118
7.7 Summary 122

VIII SUMMARY, CONCLUSIONS, AND FUTURE WORK 123

8.1 Summary of Contributions 123
8.2 Conclusions 124
8.3 Future Work 125

APPENDIX A — TABLES OF COEFFICIENTS 127

APPENDIX B — GOODNESS OF FIT OF APPROXIMATIONS 129

REFERENCES 134

VITA 142

LIST OF TABLES

1 WSR-88D Parameters 12

2 Coefficients of determination for approximation of data products using LLSE coefficients 69

3 Coefficients of determination for approximation of data products using NLSE coefficients 69

4 Terms in $\boldsymbol{\delta}$ Matrix 83

5 MLE Statistics 90

6 Square root of diagonal terms of CRLB of DSD parameters 90

7 Eigendecomposition of MLE sample covariance matrix of DSD parameters 91

8 Eigendecomposition of inverse FIM of DSD parameters 91

9 Singular values of the Jacobian $\frac{\partial Y}{\partial X}$ 95

10 Singluar values and condition numbers of the Jacobian $\frac{\partial Y}{\partial X}$ for all nine axis ratio models 106

11 Angle of Jacobians $\frac{\partial R_r}{\partial X}$ and $\frac{\partial W}{\partial X}$ with respect to DSD CRLB direction of minimum variance 121

12 Coefficients for axis ratio integral of horizontal reflectivity (ζ_h) 127

13 Coefficients for axis ratio integral of vertical reflectivity (ζ_v) 128

14 Coefficients for axis ratio integral of specific differential phase (K_{DP}) 128

15 Coefficients for axis ratio integral of the CC (ρ) 128

LIST OF FIGURES

1 WSR-88D Directivity Pattern 9
2 WSR-88D Attenuation vs. Rain Rate 17
3 Volume Coverage Pattern Example (VCP 11) 24
4 Example Radar Reflectivity Image 27
5 Example Radar Radial Velocity Image 30
6 Oblate Raindrop 33
7 Radar data products for an EF3 tornadic storm 39
8 Raindrop Scattering Coefficients 57
9 Models for the Mean Axis Ratio of Raindrops 59
10 Models for the Standard Deviation of Raindrop Axis Ratios 61
11 Simulation Flow Diagram 89
12 Concentration ellipses: N_o vs. μ 92
13 Concentration ellipses: N_o vs. Λ 93
14 Concentration ellipses: μ vs. Λ 94
15 CRLB and MLE statistics of DSD parameters versus N_o 99
16 CRLB and MLE statistics of DSD parameters versus μ 100
17 CRLB and MLE statistics of DSD parameters versus Λ 101
18 CRLB of DSD parameters for different axis ratio models versus N_o . 103
19 CRLB of DSD parameters for different axis ratio models versus μ . . 104
20 CRLB of DSD parameters for different axis ratio models versus Λ . . 105
21 CRLB and MLE statistics of rain rate and LWC versus N_o 113
22 CRLB and MLE statistics of rain rate and LWC versus μ 114
23 CRLB and MLE statistics of rain rate and LWC versus Λ 115
24 CRLB of R_r for different axis ratio models 116
25 CRLB of W for different axis ratio models 117
26 Square root of CRLB of rain rate versus rain rate 119
27 Square root of CRLB of LWC versus LWC 120

28 Goodness of fit of horizontal reflectivity (Z_H) approximation 129
29 Goodness of fit of vertical reflectivity (Z_V) approximation 130
30 Goodness of fit of differential reflectivity (Z_{DR}) approximation 131
31 Goodness of fit of specific differential phase (K_{DP}) approximation . . 132
32 Goodness of fit of CC (ρ) approximation 133

SUMMARY

Radar is an indispensable tool in the observation, analysis, and prediction of weather. The Weather Surveillance Radar 1988-Doppler (WSR-88D) is the primary source of weather radar data in the United States (U.S.), providing dual-polarimetric (dual-pol) radar measurements for the inference of meteorological phenomena.

A classic estimation problem in radar meteorology is the estimation of rain rate. Taking this problem one step further, a number of approaches have been suggested for estimating the parameters of the drop size distribution (DSD) of rain (or clouds). While various methodologies have been suggested for rain rate and DSD estimation, and numerous studies have evaluated these estimators, no fundamental limit has yet been established for how well these estimators could perform given the available dual-pol data.

One of the primary contributions of this dissertation is to derive fundamental performance bounds for the variance of any unbiased estimator of the DSD parameters given the dual-pol measurements recorded by operational weather radars, e.g., the WSR-88D. This dissertation further establishes similar bounds for the estimation of rain rate and liquid water content (LWC).

First, this dissertation presents a comprehensive background on weather radar and the WSR-88D. Then, the current state of the field for DSD and rain rate estimation is reviewed, along with the methods by which such estimators are typically evaluated. To establish variance bounds for the estimation of DSD parameters, this dissertation begins by finding a closed-form expression that suitably approximates the complicated mathematical mapping between the DSD parameters of rain (or clouds) and the expected value of the dual-pol radar measurements. With these expressions and

an appropriate dual-pol signal model, the Cramér-Rao lower bound (CRLB) of the DSD parameters is derived. This result is then applied to determine the CRLB of rain rate and LWC as well. Then, to test the existence of an efficient estimator for each of these quantities, which is both unbiased and achieves the CRLB, an approach for determining their maximum-likelihood estimates (MLE) is proposed and applied. Further, an extensive parametric analysis of the CRLB and MLE of the DSD parameters, rain rate, and LWC is performed to gather more substantial conclusions regarding the derived bounds. This dissertation concludes with an in-depth analysis of the efficacy of the dual-pol radar measurements for estimation of the DSD parameters, rain rate, and LWC.

CHAPTER I

INTRODUCTION

Radar plays a key part in the observation, analysis, and prediction of severe weather events and other meteorological phenomena. The Weather Surveillance Radar 1988-Doppler (WSR-88D) is the primary source of weather radar data in the United States (U.S.) and U.S. territories, with 155 WSR-88D network sites (and an additional five non-network WSR-88Ds), operated by the Departments of Commerce, Transportation, and Defense [58]. These radars are commonly referred to as the NEXRAD (Next-Generation Radar) network.

Originally, the WSR-88D was deployed as a horizontally polarized radar. However, for many years, the weather radar community has encouraged the application of dual-polarization (dual-pol) radar measurements to increase the utility of weather radar. With the recent dual-pol upgrade to the WSR-88D [59], there has been revitalized interest in the application of such measurements [70, 46, 48, 47].

A classic estimation problem in radar meteorology, which may benefit from the additional measurements available from a dual-pol radar (as opposed to a single-polarimetric radar), is the estimation of rain rate. Taking this problem one step further, a number of approaches have been suggested for estimating the parameters that describe the drop size distribution (DSD) of rain. While various methodologies have been suggested for rain rate and DSD estimation, and studies have been performed to evaluate these estimators, no fundamental limit has yet been established for how well these estimators may perform given the available dual-pol data.

One of the primary contributions of this dissertation is to derive fundamental bounds for the variance of any unbiased estimator of the DSD parameters given the

standard dual-pol measurements recorded by operational weather radars, e.g., the WSR-88D. Once the desired bound for the DSD parameters is found, this dissertation further establishes similar bounds for other intrinsic quantities of interest, specifically rain rate and liquid water content (LWC). Moreover, to determine whether an efficient estimator exists for each of these quantities, an approach for finding the maximum-likelihood estimate (MLE) of the DSD parameters, rain rate, and LWC is proposed. Lastly, analysis of the resulting bounds provides insight to the utility of dual-pol radar measurements for estimating the DSD, rain rate, and LWC.

1.1 Organization

The remainder of this chapter discusses the definition and significance of the DSD, rain rate, and LWC. Chapter 2 provides a firm understanding of weather radar and a comprehensive background on the WSR-88D. Chapter 3 reviews the current state of the field for DSD and rain rate estimation along with the methods by which such estimators are typically evaluated. To establish variance bounds for the DSD parameters, a function that maps the DSD parameters to the expected value of the radar measurements is required; thus, Chapter 4 establishes closed-form expressions that suitably approximate the complicated mathematical relationship between the DSD parameters and the dual-pol measurements provided by an S-band weather radar. Chapter 5 develops an appropriate signal model for the dual-pol measurements and applies the expressions obtained in Chapter 4 to derive the Cramér-Rao lower bound (CRLB) of the DSD parameters. Moreover, a method for finding the MLE of the DSD parameters is proposed and applied to test the existence of an efficient estimator for the DSD parameters. Then, Chapter 6 performs an extensive parametric analysis of the CRLB and MLE of the DSD parameters to gather more substantial conclusions regarding the derived bounds. Chapter 7 expands on these results by deriving similar bounds for both rain rate and LWC. A parametric analysis of the CRLB and MLE of

rain rate and LWC is performed as well. Lastly, Chapter 8 summarizes the conclusions and contributions of this dissertation, in addition to discussing a logical path forward for future research.

1.2 DSD, Rain Rate, and LWC

1.2.1 Drop Size Distribution

The DSD of falling rain (or a cloud) describes both the concentration of raindrops (or cloud droplets) and the probability density function (PDF) of drop diameters.[1] The interest in DSD estimation stems from its relation to the microphysical processes of precipitation and application in estimating other fundamental quantities of interest, e.g., rain rate and LWC. In its most general form, the DSD is defined as [15]

$$N\left(D_e; X\right) = N_t p_{D_e}\left(D_e; X\right), \tag{1}$$

where N_t is the total number of drops in a unit volume and $p_{D_e}\left(D_e; X\right)$ is the PDF of the volume-equivalent drop diameters,[2] D_e, given the deterministic DSD parameter set, X.[3] While initial models represented the DSD with an exponential distribution [53], it is now widely accepted that the gamma distribution is the most appropriate for modeling the instantaneous DSD of rain events [83]:

$$N\left(D_e; X\right) = N_o D_e^{\mu} e^{-\Lambda D_e} \qquad D_e > 0, \tag{2}$$

where $X = \left[N_o \ \mu \ \Lambda\right]^T$ is the parameter set of the DSD, where $\bullet^T$ denotes the transpose. Recall from (1) that the DSD does not integrate to one, but to the number of drops

[1] Throughout this dissertation, DSD may be used interchangeably to describe the DSD of rain and the DSD of clouds.

[2] The volume-equivalent diameter of a raindrop is the diameter of a spherical raindrop that has the same volume as a non-spherical raindrop. From this point forward, the volume-equivalent diameter, D_e, of a spheroidal raindrop shall simply be referred to as diameter. Further, throughout this dissertation, the variable D shall be used to describe the diameter of raindrops when the simplifying assumption of spherical (versus spheroidal) raindrops is made.

[3] Here, the notation $p_Y\left(Y; X\right)$ indicates the dependence of the PDF of Y on the deterministic parameter set X whereas the notation $p_{Y|X}\left(Y|X\right)$ shall be used to indicate the dependence of the PDF of Y on the random variable X.

in a unit volume. Thus, these parameters define not only the mean drop diameter,

$$E\left[D_e\right] = \frac{\mu + 1}{\Lambda}, \tag{3}$$

and drop diameter variance,

$$\sigma_{D_e}^2 = \frac{\mu + 1}{\Lambda^2}, \tag{4}$$

but also the drop concentration, i.e., the number of drops per unit volume:

$$N_t = \frac{N_o \Gamma\left(\mu + 1\right)}{\Lambda^{\mu+1}}, \tag{5}$$

where $\Gamma\left(\bullet\right)$ is the gamma function.

Another parameterization of the gamma DSD, frequently used in the literature, expresses $N\left(D_e; X\right)$ in terms of physically meaningful quantities [81, 90]:

$$N\left(D_e; X'\right) = N_w f_\mu\left(\mu\right) \left(\frac{D_e}{D_o}\right)^\mu e^{-(3.67+\mu)\frac{D_e}{D_o}}, \tag{6}$$

where $X' = \left[N_w \ \mu \ D_o\right]^T$ is an alternative DSD parameter set. In (6), $f_\mu\left(\mu\right)$ is a normalization term, D_o is the median-volume diameter, and N_w is the intercept of an exponential distribution with the same water content and median-volume diameter as the gamma DSD.

1.2.2 Rain Rate

Rain rate is a measure of the rate at which rain falls to the earth's surface. Rain rate estimation is of interest for a variety of applications such as meteorology, agriculture, the environment, and sewage systems of urban areas [7]. While rain rate may be better estimated by instruments other than radar (e.g., rain gauges or distrometers[4]), radar has the unique benefit of providing vast quantities of data over a large region in a short period of time. As a result, accurate rain rate estimation has long been a goal of radar meteorology. Given that rain rate is a direct function of the rain DSD

[4]A disdrometer is an instrument used to measure the drop size distribution and velocity of falling hydrometeors.

and the terminal velocity of raindrops, DSD estimation is a natural first step in the estimation of rain rate.

Reflectivity, a measurement proportional to the received power from a reflecting object (e.g., rain drops), was initially the only measurement available to estimate rain rate. However, different DSDs can yield identical measured reflectivity values while yielding very different rain rates [73]. As a result, reflectivity-based rain rate estimators are prone to large errors. The dual-pol upgrade of the WSR-88D offers a new set of measurements (discussed in detail in Chapter 2), in addition to reflectivity, that may serve to improve the quality of rain rate estimators.

1.2.3 Liquid Water Content

LWC is a measure of the amount of cloud water in a unit volume. Estimation of LWC is of interest because it relates to the microphysical processes occuring within clouds, and knowledge of these processes may provide insight into the phenomena occuring within those clouds. For example, updraft speeds and storm intensities are related to the amount of latent heat released by production of water within clouds [25]. Another reason LWC is of interest is because high concentrations of cloud water can impact jet aircraft engines by causing them to "flame out" due to ingesting too much water [25].

LWC estimation can benefit from the newly available dual-pol radar measurements in the same way that rain rate estimation does. Like rain rate, it is a direct function of the cloud DSD, and, hence, LWC estimation is a logical progression after estimating the cloud DSD.

CHAPTER II

OPERATION AND PHENOMENOLOGY OF THE NEXRAD (WSR-88D) WEATHER RADAR

2.1 Overview

The network of WSR-88Ds spanning the U.S. is the primary source of weather radar data used by the National Weather Service (NWS) and other commercial interests to extrapolate valuable information regarding precipitation and severe weather events. There are a number of other commercial and experimental weather radars [82]; most notably, the MPAR (Multifunction Phased-Array Radar) program [49, 89, 39] is investigating the potential of a phased-array radar with the capability to aid in remote weather observation, air traffic control, air route surveillance, and homeland defense tasks. However, for the time being, the WSR-88D is the most extensively utilized and accessible source of weather radar data for governmental, commercial, and research applications. Further, the intent for the WSR-88D to continue as a primary source of remote weather observations is evidenced by the recent WSR-88D modernization efforts, which include both the dual-pol and super-resolution upgrades that have been completed in recent years [59]. Hence, along with providing a firm understanding of the basic phenomenology of weather radar in general, this chapter aims to provide a comprehensive description of WSR-88D parameters and operation.

This chapter is organized as follows. Section 2.2 reviews fundamental radar phenomenology with an emphasis on applications in meteorology. Section 2.3 describes WSR-88D parameters and operation. Section 2.4 discusses the various types of data provided by the WSR-88D and how they relate to the physical parameters of observed scatterers. Lastly, Section 2.5 exemplifies the utility of dual-pol data in the event of

severe weather.

2.2 Basic Radar Phenomenology

Many of the concepts and terminology in this section apply to the subject of radar in general. They are reviewed here, in part, to establish notation.

A monostatic radar transmits radio frequency (RF) electromagnetic (EM) waves into a region of interest and receives EM waves reflected back by objects in this region [72]. The signals received by the radar include energy reflected by objects of interest, referred to as targets, and objects that are not of interest, referred to as clutter. In the case of weather radar, the objects of interest are meteorological scatterers such as raindrops, hail, or even tornadic debris. For many radar applications, including weather radar, clutter often includes backscatter from terrain, trees, and buildings. In contrast, weather is often the clutter that obscures the target signal in other radar applications.

2.2.1 Range

A pulsed-wave radar, the type employed in meteorological applications, periodically transmits a discrete pulse of short duration and then stops transmitting while waiting to receive the reflected pulse. The time it takes for the pulse to be received directly relates to the distance traveled by the pulse, i.e., twice the range of the reflecting object. Since the pulse travels at the speed of light, $c = 2.998 \times 10^8$ m/s, the range is computed as

$$R = \frac{c\Delta t}{2}, \tag{7}$$

where Δt is the round trip time of the pulse between the radar and the reflecting object. The set of received data samples for a single pulse corresponds to a series of range bins along the EM wave's path of propagation and is often referred to as a fast-time sequence.

2.2.2 Range Resolution

Range resolution is the minimum range between two objects such that the objects are still resolvable by the radar. The bandwidth of the transmitted waveform determines the range resolution of the radar:

$$\Delta R = \frac{c}{2\beta_w}, \tag{8}$$

where β_w is the bandwidth in Hertz. In the case of a simple rectangular pulse at a constant carrier frequency, as used in the WSR-88D [38], the waveform bandwidth may be approximated as

$$\beta_w \approx \frac{1}{\tau}, \tag{9}$$

where τ is the pulse duration in seconds.

2.2.3 Cross-Range Resolution

The amount of energy transmitted by the radar in a given direction is determined by the antenna directivity pattern. The directivity pattern of the WSR-88D is shown in Figure 1.[1] Maximum energy is transmitted broadside, i.e., $\theta = \varphi = 0°$, where θ and φ are the azimuth and elevation angles, respectively, relative to the antenna normal. The two-sided antenna beamwidth is defined as the difference, in degrees, between the half power points on either side of the pattern maximum and is often referred to as the two-sided half-power (or three dB) beamwidth. Together, the half-power beamwidths in azimuth and elevation define the solid angle of primary illumination from the antenna beam.

The half-power beamwidth determines the cross-range resolution, i.e., the resolution in the azimuthal and elevation dimensions. Cross-range resolution is the minimum separation between two objects in either of the two angular dimensions

[1] While the directivity pattern in Figure 1 is plotted versus azimuth, the WSR-88D directivity pattern is axis symmetric and is, therefore, similar in the elevation dimension.

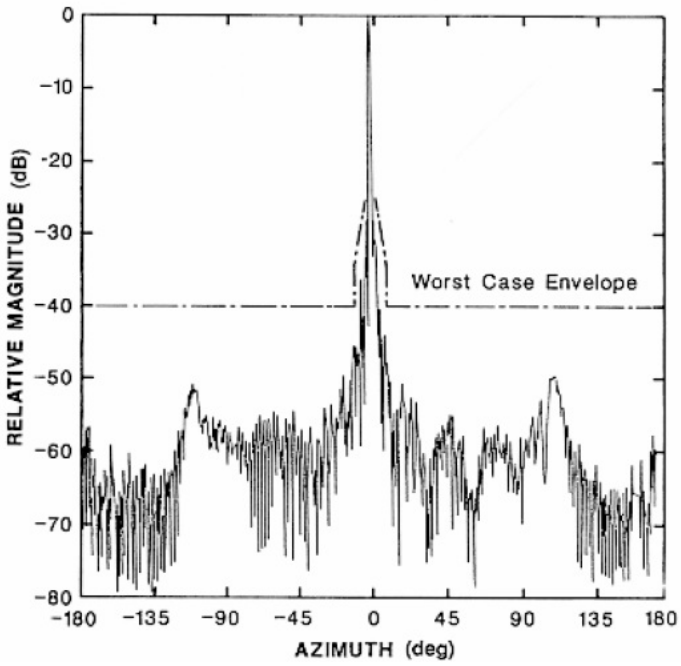

Figure 1: Representative directivity pattern for the WSR-88D and worst case sidelobe envelope. Typically, the sidelobes of the WSR-88Ds are several dB below the envelope. Source: [60].

such that the objects are still resolvable. It may be computed for the azimuthal and elevation dimensions, respectively, as

$$\Delta CR_\theta = R \sin \theta_3 \approx R\theta_3 \tag{10}$$

and

$$\Delta CR_\varphi = R \sin \varphi_3 \approx R\varphi_3, \tag{11}$$

where θ_3 is the azimuthal half-power beamwidth and φ_3 is the elevation half-power beamwidth in radians. The approximations in (10) and (11) are valid for sufficiently small beamwidths.

2.2.4 Radar Range Equation

The radar range equation (RRE) predicts the amount of power received by the radar from a reflecting object. This section starts with a generic form of the RRE [1] and develops the weather version of the RRE.

In general, the power, in Watts, received by a monostatic radar from a point target is

$$P_r = \frac{P_t G^2 \lambda^2 \sigma}{(4\pi)^3 R^4 L^2(R) L_s}, \tag{12}$$

where P_t is the peak transmit power in watts, G is the unitless gain of the antenna on transmit and receive, λ is the transmit wavelength in meters, $L(R)$ is the one-way propagation loss over range R, L_s includes all system and processing losses, and σ is the radar cross section (RCS) of the object in meters squared. The RCS of an object corresponds to the reflective strength of a target, defined as the effective area of the target as seen by the radar assuming the reflected EM wave is isotropic. However, since objects do not reflect energy isotropically, the physical scattering area of an object is not the sole governing factor in determining RCS; size, shape, orientation, and composition of the reflecting object are influencing factors as well.

For weather radar applications, there are usually many scatterers within a resolution volume, e.g., water droplets, ice crystals, and biological scatterers. Assuming uncorrelated scatter between objects and neglecting multiple scattering, the RRE can be rewritten as

$$P_r = \frac{P_t G^2 \lambda^2}{(4\pi)^3 R^4 L^2 (R) L_s} \sum_i \sigma_i, \tag{13}$$

where the equation sums over the contributions of several scatters within a resolution volume. Most often, the weather RRE is written as a function of reflectivity, or RCS per unit volume:

$$\eta = \frac{1}{\Delta_V} \sum_i \sigma_i, \tag{14}$$

where Δ_V is the radar resolution volume and η is given in units of $\frac{\text{mm}^2}{\text{m}^3}$.

The beam of the WSR-88D is axis-symmetric [60], i.e., $\theta_3 = \varphi_3$; thus, the resulting resolution volume is roughly cylindrical in shape [82, 25]. Recalling the equations for range and cross-range resolution, (8) and (10), respectively, the resolution volume can

be approximated as [82]

$$\Delta_V \approx \pi \left(\frac{R\theta_3}{2}\right)^2 \left(\frac{c\tau}{2}\right). \tag{15}$$

Using (14) and (15), the final form of the weather RRE is

$$P_r = \left(\frac{1}{2\ln(2)}\right) \frac{P_t G^2 \lambda^2 \theta_3^2 c\tau\eta}{512\pi^2 R^2 L^2(R) L_s}, \tag{16}$$

where a factor of $\frac{1}{2\ln(2)}$ has been included to account for the non-uniform Gaussian directivity pattern of the WSR-88D over the radar resolution volume [82].

2.2.5 Thermal Noise

All target echoes received by the radar compete with receiver thermal noise. Thermal noise is modeled as an additive, zero-mean white, circular, complex Gaussian process. The noise power of the radar receiver is

$$P_n = k_b T_s B = k_b T_0 F B, \tag{17}$$

where $k_b = 1.38\times10^{-23}$ J/K is Boltzmann's constant, T_0 is the standard temperature of 290 K, F is the receiver noise figure, $T_s = T_0 F$ is the system equivalent noise temperature[2] in kelvin, and B is the instantaneous receiver bandwidth. Under most circumstances, $B = \beta_w$.

Accurate estimates of the system noise power are essential to properly estimate the power of the received signal, especially since WSR-88D specifications require reflectivity and velocity estimates at signal-to-noise ratios (SNR) as low as -3 dB [91]. Based on (17) and the parameters in Table 1, the WSR-88D receiver noise power is expected to be −114 dBm. Measurements have yielded a comparable value of −113 dBm [25].

[2] T_s, in (17), refers to the system equivalent noise temperature, a term common in radar, which is related to the standard temperature, T_0, and the system effective temperature, T_e, by the equation $T_s = T_0 + T_e$.

Table 1: Key WSR-88D Parameters. Source: [60].

Antenna Subsystem	
Gain	45 dB
Polarization	Simultaneous HH and VV
Beam Width	0.93°
First Sidelobe Level	-29 dB
Elevation Steerability	+0.5° to +19.5°
Maximum Rotation Rate	30 $^\circ s^{-1}$
Transmitter Subsystem	
Transmit Frequency	2.7 to 3.0 MHz
Peak Power	750 kW
Short Pulse Width	1.57 μs
Long Pulse Width	4.5 μs
Short Pulse PRF	318 to 1304 Hz
Long Pulse PRF	318 to 452 Hz
Receiver Subsystem	
Noise Temperature	450 K
Receiver Bandwidth	0.63 MHz

2.2.6 Doppler Frequency

The WSR-88D has a coherent quadrature receiver [60], meaning it can measure the phase of a received sinusoidal wave relative to the radar's stable local oscillator (STALO). Coherence over multiple transmitted pulses yields two main advantages. First, it can offer an increased SNR. The exact gain in SNR is a function of the number of pulses in a coherent processing interval (CPI) along with the rate at which the signal decorrelates over the duration of the CPI.[3] Second, coherence facilitates measurement of the Doppler frequency:

$$f_d \equiv \frac{2V_r}{\lambda}, \tag{18}$$

[3]Throughout this disseration, a CPI refers to a sequence of transmitted pulses whose return echoes have a non-zero correlation from pulse-to-pulse. The term dwell shall be used to refer to a sequence of transmitted pulses whose return echoes are uncorrelated from pulse-to-pulse.

where V_r is radial velocity of the target in m/s. The Doppler frequency is measured over a series of pulses in a CPI. This sequence of pulses is often referred to as a slow-time sequence. The time between consecutive transmitted pulses in a CPI is referred to as the pulse repetition interval (PRI). The pulse repetition frequency (PRF) is the sampling rate of the slow-time sequence:

$$PRF = \frac{1}{PRI}. \tag{19}$$

The range of Doppler frequencies that can be measured without ambiguity is determined by the Nyquist criterion:

$$-\frac{PRF}{2} \leq f_d \leq \frac{PRF}{2}. \tag{20}$$

The magnitude of the discrete Fourier transform of the slow-time sequence for a given resolution volume provides an estimate of the target Doppler frequencies in that resolution volume. For a single scatterer with constant RCS and radial velocity over the duration of a CPI, the samples of the slow-time sequence are perfectly correlated and the magnitude of the Doppler spectrum has a narrow peak at the Doppler frequency of the target. A target with exponentially distributed, perfectly correlated echoes from pulse to pulse is a Swerling I target [79]. A Swerling II target model refers to a target with exponentially distributed echoes that completely decorrelate from pulse to pulse, resulting in a white Doppler spectrum. At the PRIs utilized in weather radars, raindrop scatter only partially decorrelates from pulse to pulse and cannot be modeled as a Swerling I or Swerling II target. The Doppler spectrum of rain scatter is commonly modeled as Gaussian with the spectral width being related to the rate of decorrelation.

2.2.7 Polarization

The EM waves transmitted by a radar are associated with a vector quantity, E, which lies in a plane orthogonal to the direction of the EM wave's propagation. Assuming

the EM waves travel along the z-axis of a Cartesian coordinate system, the electric field vector, varying sinusoidally in time and space, has the form

$$E = E_x \cos(2\pi f_t t - kz) + E_y \cos(2\pi f_t t - kz + \psi_t), \tag{21}$$

where E_x and E_y are vectors in the x (i.e., horizontal) and y (i.e., vertical) directions, respectively, with norms equal to the amplitude of sinusoidal variation in their respective directions, k is the wavenumber (spatial frequency in radians per meter), f_t is the transmitted frequency, and ψ_t is the relative phase of the x and y components upon transmission. The orientation of the electric field vector defines the polarization of the wave. If the wave only has a horizontal component (i.e., parallel to the earth's surface and orthongonal to the direction of propagation), it is horizontally linearly polarized. Similarly, if the wave only has a vertical component (i.e., orthogonal to the earth's surface and the direction of propagation), the wave is vertically linearly polarized. The wave may also be linearly polarized at an angle other than horizontal or vertical. Other forms of polarization include circular, elliptical, or unpolarized. The WSR-88D simultaneously transmits and receives horizontally and vertically polarized waves [60]. More details on the dual-pol operation of the WSR-88D are provided in Section 2.3.6. For a more in-depth discussion on polarization and its applications in radar, see [87].

In general, the backscatter RCS of a target depends on the polarization of the incident EM wave. The RCS of spheres and spheroids are of particular interest in weather radar as they are often used as shape models for reflecting hydrometeors, e.g., raindrops and some hail. In the case of a perfect sphere, the RCS is independent of polarization and related to the sphere diameter. However, given an oblate or prolate spheroid, the RCS becomes a function of polarization. Denoting the transmit and receive polarizations as t-type and r-type, respectively, where r and t are either h for horizontal or v for vertical, the polarization-dependent RCS σ_{rt} is related to the

scattering coefficient S_{rt} through the equation[4]

$$|\sigma_{rt}|^2 = 4\pi |S_{rt}|^2 . \tag{22}$$

The polarization-dependent scattering coefficients are often written in a scatter matrix, S:

$$\begin{bmatrix} E_s^h \\ E_s^v \end{bmatrix} = \frac{e^{-jkR}}{R} \underbrace{\begin{bmatrix} S_{hh} & S_{hv} \\ S_{vh} & S_{vv} \end{bmatrix}}_{S} \begin{bmatrix} E_i^h \\ E_i^v \end{bmatrix}, \tag{23}$$

where $E_i^\bullet$ is an incident electric field component, $E_s^\bullet$ is a scattered electric field component, $\bullet^h$ indicates horizontal polarization, and $\bullet^v$ indicates vertical polarization. The $\frac{e^{-jkR}}{R}$ term is the spherical wave factor which accounts for the phase change and spreading of the EM wave as a function of R from the object of incidence. The scattering matrix reveals how the reflecting object affects the incident wave in terms of polarization, amplitude, and phase shifts.

When a sphere's radius is significantly smaller than the wavelength of the incident EM field, it lies in the Rayleigh scattering regime [84], and its RCS directly relates to the sphere's radius. Similarly, Rayleigh[5] theory can also be applied to define the RCS of an oblate spheroidal raindrop, in which case the effective RCS is largest if the plane of polarization is the same as the plane of the spheroid's semi-major axes. This phenomenon is used in meteorological applications to infer information regarding the size, shape, composition, and orientation of detected hydrometeors, as discussed in more detail in Section 2.4.

[4]In general, the scattering coefficient is a function of the direction of scatter. For the purposes of this chapter, unless otherwise stated, the scattering coefficients refer to backscatter in the direction of the radar.

[5]In the weather radar literature, the Rayleigh scattering of spheroids is termed Rayleigh-Gans scattering after Gans who derived the equations for Rayleigh scattering of spheroids [15]. This unfortunate terminology is not used in this dissertation to avoid confusion with actual Rayleigh-Gans scattering, an approximation for the scattering of small particles with an index of refraction near unity [84].

2.2.8 Attenuation

When EM waves travel through the atmosphere, the waves are attenuated by gases, water vapor, and hydrometeors due to absorption and scattering. At the frequency band of many weather radars (S-band), attenuation is low enough that the radar is able to see into and through significant precipitation; however, attenuation is substantial enough that it cannot be neglected [25]. The total attenuation loss due to rain in a unit volume is

$$\begin{aligned} k_p &= \int_0^\infty \left[\sigma_a(D) + \sigma_{ts}(D)\right] N(D) dD \\ &= \int_0^\infty \sigma_e(D) N(D) dD, \end{aligned} \tag{24}$$

where σ_a is the effective absorption cross section, σ_{ts} is the total effective scattering cross section, $\sigma_e = \sigma_a + \sigma_{ts}$ is the extinction cross section, and $N(D)$ is the DSD.[6] The total attenuation over the path of propagation is a function of range. In the case of small raindrop diameter-wavelength ratios [25], the absorption effect is more dominant than the scattering effect and can be approximated as

$$\sigma_a = \frac{\pi^2 D^3}{\lambda} \Im(K), \tag{25}$$

where D is the raindrop diameter, $\Im$ denotes the imaginary component of a complex number, and K is

$$K = \frac{m_r^2 - 1}{m_r^2 + 2}, \tag{26}$$

where $m_r = n_r - j n_r \kappa_a$ is the complex refractive index of water, where the real part, n_r, is often referred to as simply the refractive index and κ_a is the attenuation index. The rate of attenuation, usually expressed in dB/km, has been characterized for a range of rain rates, DSDs, and frequencies [82]. For WSR-88D operations, attenuation due to rain is traditionally estimated based on the reflectivity factor, or equivalently,

[6] For notational simplicity, the dependence of the DSD on the parameter set, X, is not shown here. This convention is followed throughout Chapter 2.

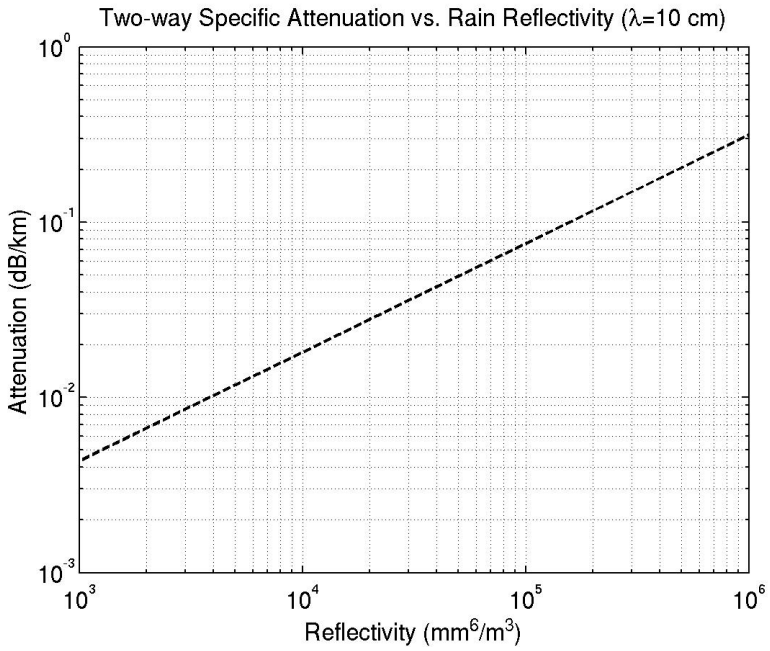

Figure 2: Specific two-way attenuation versus reflectivity as assumed in WSR-88D calculations.

the RCS of rain (discussed in detail in Section 2.4.1) as observed and estimated by the WSR-88D [60]. The presumed reflectivity-attenuation relationship is shown in Figure 2.

2.2.9 Clutter and Anomalous Propagation

The signal received by a weather radar is sometimes contaminated with clutter, echoes from objects that are not of interest and interfere with the signal the user would like to observe [1]. In many radar applications, clutter includes echoes from precipitation, whereas remote sensing of precipitation is a primary goal of weather radars. In meteorological applications, clutter frequently includes objects such as terrain, buildings, and trees.[7] Under normal circumstances, clutter only contaminates the WSR-88D signal when the antenna is at a low elevation angle [25]. However, on rare occasions, abnormally significant departures from the atmosphere's typical refractive

[7]Technically, clutter also includes signals from birds and insects. However, in application, echoes from birds and insects are distinguished from stationary clutter and are given a separate classification of "biological scatterers."

index gradient may result in a phenomenon referred to as anomalous propagation (AP). AP occurs when significant temperature inversions or large moisture gradients cause abnormally large refractive index gradients, which in turn bend the path of the transmitted wave back towards Earth.

Since clutter consists of returns from nominally stationary objects, the clutter slow-time spectrum is centered at zero velocity with a narrow spectral width. These two attributes are often used to discriminate clutter from meteorological echoes[60]. In the case of AP, it may not be possible to recover any usable meteorological signals from the contaminated resolution volumes. However, in other cases, clutter mitigation is often achieved by applying a notch filter to the slow-time data sequence. Rather than apply the notch filter indiscriminately, a site-specific clutter map might be used to determine not only which portions of the data require a clutter filter but also the parameters of the clutter filter (i.e., null width and depth) [61].

2.3 Operation of the WSR-88D

The WSR-88D was originally designed as a single frequency (S-band), horizontally polarized radar. All WSR-88Ds have since been modified to support dual-pol capability [82, 59], transmitting and receiving both horizontally and vertically polarized waves simultaneously. The simultaneous transmission is achieved by transmitting a linearly polarized wave at a 45° angle. The horizontal and vertical components of the wave are then simultaneously received in the horizontal and vertical receive channels of the radar, respectively. The network of WSR-88Ds has also been upgraded to include a super-resolution mode that yields data points on a finer range-azimuth grid than the legacy resolution [82].

2.3.1 Signal Processing Chain

To generate data for a set of resolution volumes along a single radial (i.e., along range), the WSR-88D transmits a series of pulses in a CPI, receives the reflected pulses

through a coherent quadrature receiver, and applies a matched filter to the received signal. The result is a two-dimensional $N_r \times N_p$ range-pulse map of complex (i.e., I-Q) data. This I-Q data is often referred to as level I data. For each resolution volume, the N_p pulses are used to estimate the first three spectral moments of the data. The zero moment corresponds to the average power reflected by scatterers in a given resolution cell, while the first and second moments correspond to estimates of the mean and standard deviation of the underlying distribution of scatterer radial velocities. Both the first and second moments are estimated using pulse-pair processing, as described in Sections 2.4.2.2 and 2.4.3.2. These three measurements are the classic single-polarization level II data products[8] and are among the most rudimentary level of data recorded operationally [62].

2.3.2 Coordinate System and Propagation

The WSR-88D collects data from a full three-dimensional volume by mechanically steering in azimuth and elevation. Each complete volume scan is composed of a series of constant elevation scans, referred to as cuts, with each cut consisting of a full 360° in azimuth and ranges up to 460 km. The resulting data is stored in a three-dimensional array, with the dimensions corresponding to the spherical coordinates of the radar. Azimuth is measured in degrees clockwise from due north, elevation is measured in degrees from the altitude line of the radar, and range is defined as the slant range in meters from the radar. Computing the ground range and height of a particular data point cannot be accomplished with a simple spherical-to-Cartesian conversion since the atmosphere's refractive index has a discernable impact on EM wave propagation. The wave follows a curved path with curvature proportional to the derivative of the refractive index. In general, the refractive index is assumed to be horizontally homogeneous and change only as a function of height [25]. Thus, the

[8] In the weather radar literature, the term "product" can describe both level II data and other quantities derived from such level II data, but it is rarely used to refer to level I data.

curvature of the path of propagation is usually expressed as

$$C_p = -\frac{dn_r}{dh}, \tag{27}$$

where n_r is the refractive index and h is the height above sea level. To account for the curved path of propagation, it is common to use an equivalent Earth model [25], where the radius of Earth is assumed to be

$$R_e^E = k_e R_e, \tag{28}$$

where R_e is the true radius of the Earth and $k_e = \frac{4}{3}$. With this model, the ground range is approximated by

$$R_g = R_e^E \sin^{-1}\left(\frac{R\cos\theta}{R_e^E + h}\right), \tag{29}$$

where R is the slant range (or simply range) to a scatterer and the height above sea level, h, is approximated as

$$h = \sqrt{R^2 + {R_e^E}^2 + 2RR_e^E \sin\theta} - R_e^E. \tag{30}$$

2.3.3 Radar Parameters

The quality, resolution, and volume coverage of the WSR-88D level II data is dependent on the operational parameters of the radar. Many of these parameters are adjustable and chosen based on current weather conditions. Most adjustable parameters are set by selecting a volume coverage pattern (VCP), described in detail in Section 2.3.4. There are a variety of VCPs, each defined for specific meteorological conditions. The most notable parameters varied in VCPs are PRF, pulse width, cut elevation angles, and antenna rotation rate; these parameters are described below.

2.3.3.1 PRF

The PRF is the frequency at which the radar transmits pulses. In addition to determining the unambiguous velocity interval (as discussed in Section 2.2.6), the PRF

also determines the maximum range at which objects can be detected unambiguously. If an object is far enough in range, then it is possible that the reflected pulse will not be received until after the next pulse has been transmitted. The reflection of the first pulse from a far-range object is indistinguishable from a reflection of the second pulse from a near-range object, resulting in range ambiguity. Choosing the PRF involves trading off unambiguous velocity against unambiguous range. Recall from (20) that the maximum unambiguous target velocity is directly proportional to the PRF, whereas the maximum unambiguous range is inversely proportional to PRF:

$$R_{ua} = \frac{cPRI}{2} = \frac{c}{2PRF}, \tag{31}$$

where R_{ua} is the maximum unambiguous detection range in meters. The apparent range of any target beyond the maximum unambiguous range is

$$R_a = R \bmod R_{ua}, \tag{32}$$

where R is the true target range and "mod" denotes the modulo operation. Using two or more PRFs, target ranges can be disambiguated. By applying algorithms based on the Chinese remainder theorem, range measurements across different PRFs are aligned [71]. Power and velocity measurements are then compared to determine the range of the dominant return [63].

2.3.3.2 Pulse Width

The WSR-88D has two pulse width options, a short pulse of 1.57 μs and a long pulse of 4.5 μs [60]. The short pulse provides better range resolution and is used in high PRF modes for a greater span of unambiguous velocity measurements. The long pulse, on the other hand, yields higher average signal power,[9] evidenced by how received power scales with pulse width in (16).

[9] Although weather radars could simultaneously achieve high resolution and high SNR by exploiting more sophisticated waveforms than simple rectangular pulses [56], the current waveform set of the WSR-88D is likely to remain standard for the foreseeable future.

Traditional fast-time filters are matched to the shape and duration of the transmitted waveform. The matched filter implementation in the WSR-88D samples the fast-time data at the range resolution of the short pulse ($\approx$ 250 meters) and uses the short-pulse waveform in the filtering process, regardless of which pulse length is transmitted. When the long pulse is transmitted, a three-sample coherent block average is applied to the "matched" filter output, reducing the data to the approximate range resolution of the long pulse. This procedure, which simplifies the design of the hardware (as described in Section 4.8 of [63]) well approximates traditional matched filtering and downsampling.

2.3.3.3 Cut Elevation Angles

The term cut refers to a set of recorded data over all azimuth and range for a single elevation angle. Cut elevation angles are selected based on a number of factors including the type, rate of change, range, and extent of weather being observed. For example, if significant weather is observed at far ranges, a VCP with a greater number of low elevation cuts may be selected to obtain sufficient vertical sampling at those ranges. If meteorological conditions are changing rapidly, a VCP with fewer elevation cuts may be selected to maintain a certain volume coverage rate. In clear weather, a VCP with relatively few elevation cuts scanned at a slower rate may be selected to maintain a minimum volume coverage rate while obtaining an increased sensitivity by increasing the duration of a CPI.

2.3.3.4 Antenna Rotation Rate

The WSR-88D scans a single elevation cut at a time, mechanically scanning in azimuth. The antenna rotation rate and PRF determine the maximum number of pulses in a CPI, which is equal to the number of pulses transmitted during an antenna rotation of one beamwidth, i.e.,

$$N_p \leq \frac{\theta_3 PRF}{\frac{d\theta}{dt}}, \tag{33}$$

where N_p is the number of pulses in a CPI and $\frac{d\theta}{dt}$ is the rotation rate of the antenna in radians per second. This criterion ensures that the antenna beam overlaps for all pulses in a CPI. Hence, lower rotation rates provide higher SNR and improved velocity resolution at the expense of slower volume coverage.

In traditional radar applications, in which the target is a point target, scanning the antenna over the course of a CPI results in a signal processing loss from the amplitude modulation of the beam as it scans over the target. This is referred to as beamshape loss. However, in weather radar, in which the target is volumetric, it is common to assume the target uniformly fills the radar resolution volume, and the effects of scanning are modeled as in increase in the effective beam size [24].

2.3.4 Volume Coverage Patterns

A VCP is a scan strategy that designates the parameters of the volume scan, specifically the elevation angles at which cuts are taken, the types of cuts taken, and the radar parameters used for those cuts.

The WSR-88D employs three types of cuts: split, batch, and contiguous Doppler X (CDX) [63]. Split cuts scan a particular elevation slice twice, once in a contiguous surveillance (CS) mode and once in a contiguous Doppler (CD) mode. The CS mode uses a low PRF for collecting intensity (i.e., power) data over maximum range extent, while the CD mode uses a high PRF for better velocity resolution. The CS mode is also used to disambiguate range-folded CD data. Furthermore, split cuts facilitate clutter suppression; thus, they are often used at elevation angles below 1.65° where efficient clutter suppression is a necessity. Batch cuts alternate between high and low PRFs in a single cut. They offer many of the benefits of split cuts, without requiring a second scan of the same elevation slice. Batch cuts are employed for middle elevation angles (i.e., between 1.8° and 6.5°) where clutter contamination is less problematic. CDX cuts employ a high PRF with a quick-rotating antenna at elevation angles above

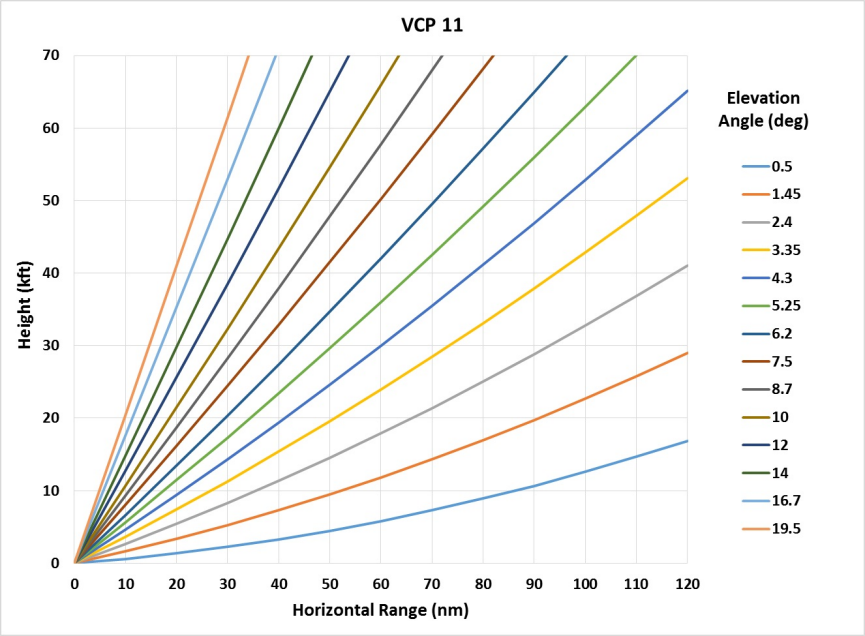

Figure 3: VCP 11 samples fourteen elevation angles in five minutes. The lowest two angles use "split cut" (CS/CD), middle angles use batch, and higher angles use Contiguous Doppler (CDX) mode. The beams shown represent the beam height as a function of range and account for both the earth's curvature and standard atmospheric refraction of the beam.

6.5°. CDX cuts do not require range unfolding since little reflectivity arises from far ranges at these elevation angles. The highest elevation angle setting for any VCP is 19.5°. The space above this angle is referred to as the cone of silence, which is the vicinity above the radar where no radar observations are made.

VCPs are composed of a combination of split, batch, and CDX cuts. The VCP is usually selected automatically based on the type and range of significant weather patterns that have already been detected. An example VCP is show in Figure 3.

2.3.5 Legacy Resolution versus Super Resolution

Traditionally, for each cut of data in a volume scan, the WSR-88D generates a range-azimuth grid sampled at the approximate resolution of the radar, 250 (or 750) meters by 1° for the short (or long) pulse. The 1° azimuthal resolution corresponds to the approximate beamwidth of the WSR-88D and is the result of choosing the maximum

length CPI that satisfies (33). By choosing the maximum length CPI, the best possible velocity resolution is attained and statistical variations of the radar measurements are minimized. This is referred to as legacy resolution.

While both batch and CDX cuts still operate at legacy resolution, the split cuts now operate in the new super-resolution mode. The motivation for super-resolution surveillance is described in detail in [18] and [17], which show that certain severe storm reflectivity and Doppler signatures are better and more frequently identified by generating a grid with an azimuthal sampling rate of 0.5° (i.e., super-resolution mode) rather than 1°, i.e., legacy resolution. The term "super resolution," when referring to the WSR-88D, simply refers to the ability to collect more CPIs at an increased azimuthal sampling rate.[10] It does not refer to an actual increase in the radar resolution. Rather, the increased azimuthal sampling is achieved by decreasing the duration of a CPI by half. The negative consequence of a shorter CPI is an increase in the standard deviation of the reflectivity and Doppler estimates. Since the purpose of super-resolution mode is increased spatial resolution, this mode always uses the short-pulse waveform for increased range resolution.

2.3.6 Dual-Polarization

All WSR-88Ds have been upgraded in recent years to include a dual-pol capability, i.e., the ability to simultaneously transmit and receive both horizontally and vertically polarized waves [82]. Details of the initial dual-pol performance analysis and calibration process can be found in [54]. Since the WSR-88D is not capable of switching polarizations (as in a polarization-diversity radar) or waveform diversity (as in a polarization-agile radar) [51], the WSR-88D does not measure all four scattering coefficients of a target, but rather measures the sum of the co-pol and cross-pol powers

[10]This terminology is contrary to its traditional usage in signal processing applications in which it refers to autoregressive processing techniques that achieve super resolution by assuming a specific form for a signal to be estimated.

received in each channel, i.e., $S_{hh}^2 + S_{hv}^2$ and $S_{vv}^2 + S_{vh}^2$. For applications involving rain drops, the cross-polarization terms are often considered negligible since most rain drops fall with a nearly vertical axis of symmetry [6]. For applications involving more complex scatterers (e.g., snowflakes, birds, and tornadic debris), it is common to resort to data mining algorithms to predict the dual-pol returns.

With the dual-pol upgrade, three new measurements are now included as part of the level II data products. These include differential reflectivity, the co-polar correlation coefficient, and (specific) differential phase. The primary motivation for these supplementary data products is the added ability to discriminate various hydrometeors and improve quantitative forecasts by inferring the size, shape, distribution, and concentration of scatters. For example, spherical hydrometeors have a similar RCS for both horizontal and vertical polarizations; however, raindrops become more oblate as they grow in size, and hence, yield greater differences between the scattered waves of the two polarizations. The three dual-pol products measure these differences in various ways and are explored in more detail in Section 2.4.

Despite the addition of the vertically polarized channel, all three of the original level II data products (i.e., reflectivity, radial velocity, and spectral width) are still measured from the horizontally polarized channel. The vertical channel is simply employed to generate the three new dual-pol products.

2.4 Weather Radar Data Products

Level II data products include any quantity derived directly from the I-Q data of the radar. The WSR-88D records six level II data products for each resolution volume: reflectivity, mean radial velocity, spectral width, differential reflectivity, the co-polar correlation coefficient, and differential phase. Reflectivity, radial velocity, and spectral width are the classic single-polarization data products, whereas differential reflectivity, the co-polar correlation coefficient, and differential phase are the more recently

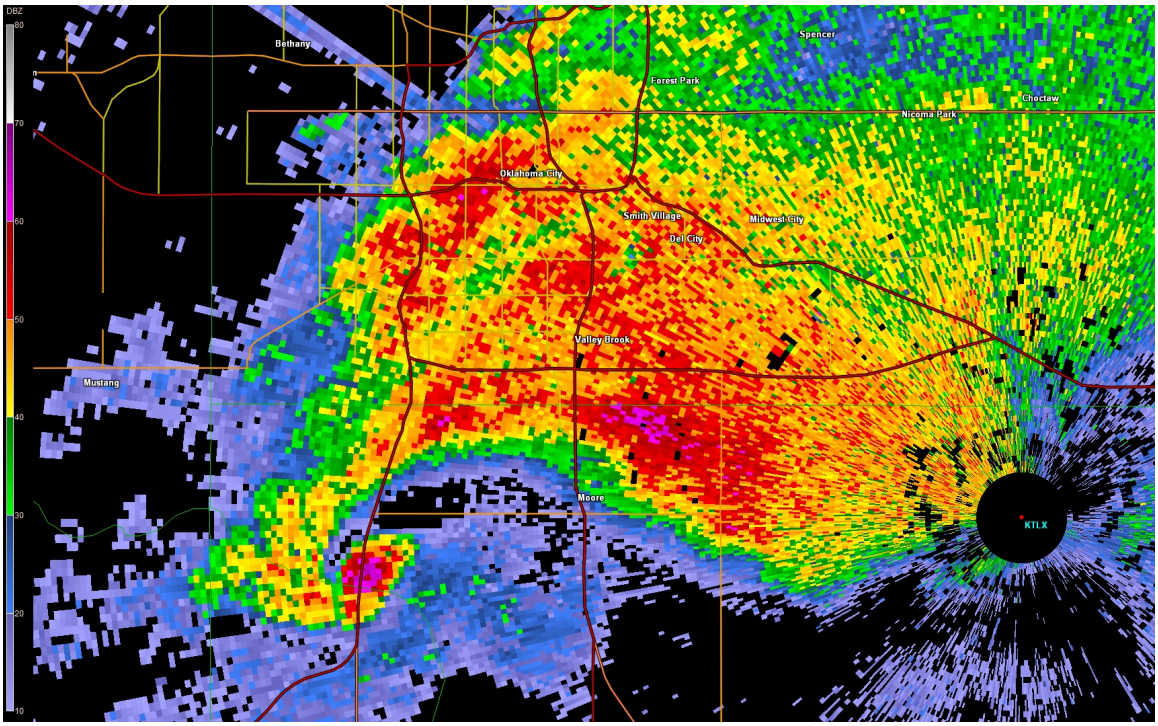

Figure 4: A radar reflectivity image of a classic supercell containing a violent tornado near Oklahoma City, Oklahoma on May 20, 2013.

added dual-pol data products.

2.4.1 Reflectivity

Reflectivity is a measure of the efficiency of a target in intercepting and reflecting radio energy back towards the radar [62]. More specifically, it is a measure of the per unit area or per unit volume (in the case of meteorological scatterers) RCS of objects observed by the radar [1]. For a single hydrometeor, reflectivity is a function of size, shape, physical state (e.g., water or ice), and aspect angle. However, some simplified models are often used to model the RCS of certain hydrometeor types. This section focuses specifically on rain.

An example reflectivity image for a classic tornadic supercell, which affected Oklahoma City, OK during the afternoon of May 20, 2013, is shown in Figure 4. The main body of the supercell is the large area of high reflectivity, depicted by yellows and reds, in the center of the figure. At the bottom left of the main supercell, a “hook”

and possible "debris ball" can be seen. An area of lower reflectivity, indicating inflow into the tornado, is positioned to the right and above the hook and debris ball.

2.4.1.1 Phenomenology

In the simplest case, raindrops and small hail are modeled as perfect spheres that act as Rayleigh scatterers. With these assumptions, the RCS of an individual raindrop is [15, 84]

$$\sigma = \frac{\pi^5 |K|^2 D^6}{\lambda^4}. \tag{34}$$

It is this model that gives rise to the term reflectivity factor, defined as

$$\zeta = \frac{1}{\Delta V} \sum_i D_i^6 = \frac{\lambda^4 \eta}{\pi^5 \left|K\right|^2}. \tag{35}$$

Reflectivity factor is given in units of $\frac{\text{mm}^6}{\text{m}^3}$; however, due to the large range of possible values of reflectivity factor, it is traditionally expressed on a dB scale, $Z = 10 \log_{10} \zeta$, with units of dBz.[11] Placing reflectivity in the weather RRE yields

$$P_r = \left(\frac{1}{2 \ln (2)} \right) \frac{P_t G^2 \theta_3^2 c \tau \pi^3 |K|^2 \zeta}{512 \lambda^2 R^2 L^2 \left(R\right) L_s}. \tag{36}$$

The value of $|K|^2$ in the weather RRE depends on the physical state of observed hydrometeors. However, for a reasonable range of temperatures (0° to 20° C) and wavelengths (3 to 10 cm), the values of $|K|^2$ can be approximated as

$$|K|^2 \approx 0.93 \tag{37}$$

for water and

$$|K|^2 \approx 0.197 \tag{38}$$

for ice [82]. The physical state is usually hypothesized based on factors such as temperature and the altitude of the melting layer in stratiform events.[12] However,

[11] From this point forward, reflectivity factor shall simply be referred to as reflectivity, as is common in meteorological jargon.

[12] Stratiform precipitation results from the forced lifting of air. As the air rises, it cools, causing the air mass to saturate, form clouds, and eventually precipitate. Stratiform events are most often characterized as wide-spread, homogeneous rain events with less intense rain rate than convective events.

the actual computation of reflectivity usually assumes a refractive index of water regardless of the conjectured hydrometeor phase [82].

While the Rayleigh scattering model of a sphere is a good approximation for the RCS of small raindrops and hail, large raindrops tend to have an oblate shape resulting in polarization-dependent RCS properties. Also, hail can grow large enough in diameter such that it falls into the nonlinear Mie scattering regime; i.e., the Rayleigh scattering approximation is no longer valid.

2.4.1.2 Calculation

Using the weather RRE, the power received by the radar can be equated to a reflectivity value. To estimate the reflectivity, the average received power is estimated as a linear average over multiple pulses in one or more resolution volumes [25]:

$$\widehat{P}_r = \frac{1}{N_p}\sum_{i=1}^{N_p}|x_i|^2 - \widehat{P}_n, \tag{39}$$

where $\widehat{\bullet}$ denotes an estimate, x_i is the measurement of a single pulse for a single resolution volume, and $\widehat{P}_n$ is the estimated noise power of the radar. The exact number of averaged samples depends on the VCP of the radar, which dictates spatial and temporal resolution requirements. Reflectivity is then estimated as

$$\begin{aligned}\widehat{Z} &= 10\log_{10}\widehat{\zeta} \\ &= 10\log_{10}\left[2\ln(2)\frac{512\widehat{P}_r\lambda^2R^2L^2\left(R\right)L_s}{P_tG^2{\theta_3}^2c\tau\pi^3|K|^2}\right],\end{aligned} \tag{40}$$

where $\widehat{\zeta}$ is the estimated linear scale reflectivity and $\widehat{Z}$ is $\widehat{\zeta}$ converted to dBz.

2.4.2 Radial Velocity

The radial velocity reported by the WSR-88D signal processor is an estimate of the reflectivity-weighted average motion of targets towards or away from the radar within a given resolution volume. An example radial velocity image from the May 20, 2013

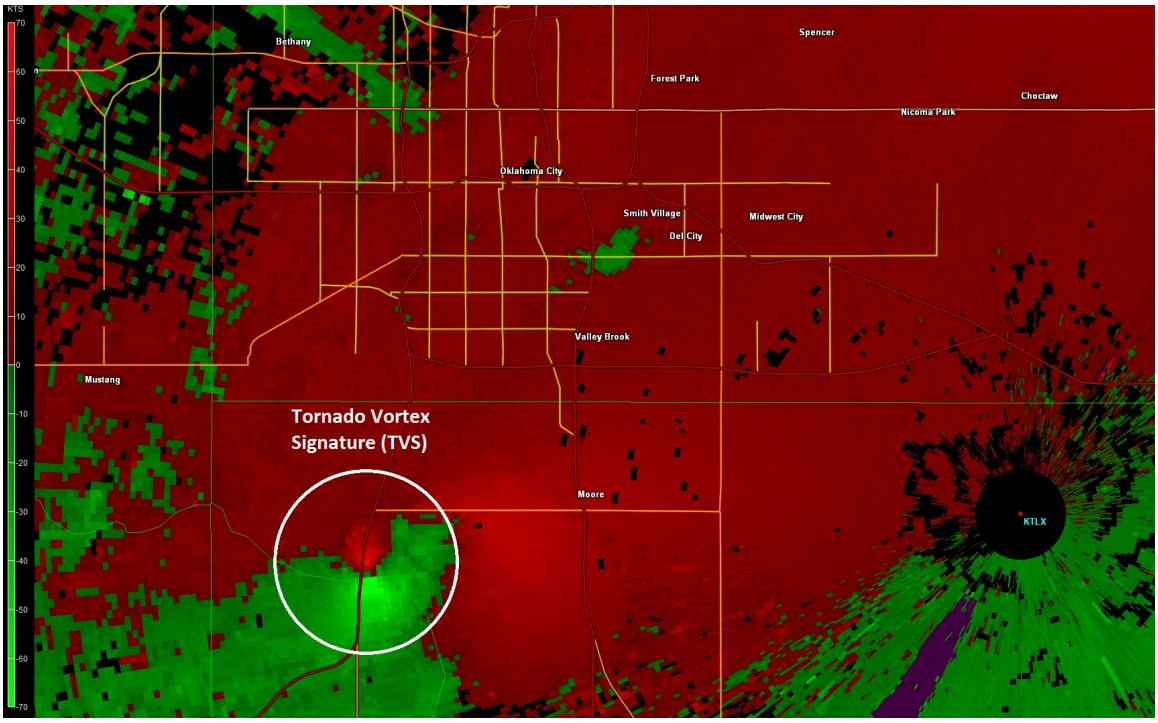

Figure 5: A radar radial velocity image containing a tornadic vortex signature (TVS). The TVS is marked by a significant gradient in the velocity field.

tornadic supercell (discussed in Section 2.4.1) is shown in Figure 5. The radial velocities of the supercell show a large scale circulation both towards the radar (depicted in green) and away from the radar (depicted in red). Within the area circled in white, a tight couplet of red and green indicates an area of increased circulation in the vicinity of the tornado core. Comparing Figures 4 and 5, it's evident that this couplet is co-located with the area of increased reflectivity ascribed to the "debris ball" in Figure 4.

Several independent mechanisms contribute to the apparent motion of the numerous hydrometeors in a resolution volume. Based on the Central Limit Theorem, it is common to model the power spectrum of the coherent pulse sequence as Gaussian. In fact, it is estimated that over 75% of all observed spectra are Gaussian shaped [44].

2.4.2.1 Phenomenology

Scatterer velocity is determined by measuring the Doppler frequency. As mentioned previously, the radar is only capable of measuring the radial velocity component of a target. The measured radial velocity is a linear combination of the line-of-sight components of the horizontal and terminal-fall velocities of hydrometeors in the antenna beam width and can be computed as

$$V_r = -V_{h_x} \cos(\theta) \, cos(\varphi) - V_{h_y} \sin(\theta) \cos(\varphi) + V_f \sin(\varphi), \tag{41}$$

where V_{h_x} and V_{h_y} are the horizontal hydrometeor velocities in the x and y directions, respectively, and V_f is the fall speed of the hydrometeor [19].

2.4.2.2 Calculation

The average radial velocity of the power spectrum for a given resolution volume is estimated using pulse-pair processing [95], which assumes a Gaussian-shaped power spectrum. The mean velocity is estimated from the phase angle of the first lag of the autocorrelation of the slow-time signal:

$$\widehat{V}_r = -\frac{\lambda}{4\pi PRI} \arg \widehat{R}_x \, [1], \tag{42}$$

where $\widehat{R}_x$ is the estimated autocorrelation function of the measured slow-time sequence and "arg" denotes the angle of a complex number.

2.4.3 Spectral Width

Spectral width is a measure of the dispersion of the scatterer velocities within the radar resolution volume and is defined as the standard deviation[13] of the velocity power spectrum [62]. It is also a measure of the reliability of the estimated radial

[13]Here, we use the term "standard deviation" as a mathematical description of the spread of the power spectrum; the power spectrum itself is not a probability density, although the power spectrum is expected to be related to the probability density of the underlying hydrometeor velocities.

velocity. Before the advent of dual-pol, spectral width was often used to identify areas of tornadic debris.

2.4.3.1 Phenomenology

Spectral width, σ_{V_r} is modeled as a sum of independent broadening mechanisms [78, 25]:

$$\sigma_{V_r}^2 = \sigma_s^2 + \sigma_\alpha^2 + \sigma_f^2 + \sigma_o^2 + \sigma_t^2, \tag{43}$$

where σ_s^2 is due to radial shear, σ_α^2 is due to antenna motion, σ_f^2 is due to variation in hydrometeor fall speed, σ_o^2 is due to oscillation and orientation changes of hydrometeors, and σ_t^2 is due to turbulence.

2.4.3.2 Calculation

Similar to the computation for average radial velocity, the width of the slow-time power spectrum is estimated using pulse-pair processing[14] [95]:

$$\widehat{\sigma}_{V_r} = \frac{\lambda}{2\pi PRI\sqrt{2}} \ln\left(\frac{\widehat{R}_x[0] - \widehat{P}_n}{|\widehat{R}_x[1]|}\right). \tag{44}$$

2.4.4 Differential Reflectivity

Differential reflectivity is the ratio of the horizontally and vertically polarized power returns from a given resolution volume [62]. It is considered to be a good indicator of raindrop shape, which is highly correlated with drop size. Differential reflectivity is deemed helpful in estimating rain rate since reflectivity does not have a one-to-one relation with rain rate.

2.4.4.1 Phenomenology

While small raindrops are approximately spherical, aerodynamic and viscous forces cause larger raindrops to have an oblate (i.e., oriented with the major axis in the

[14] It is possible for the term inside the logarithm to be negative. In that case, the estimate is not valid.

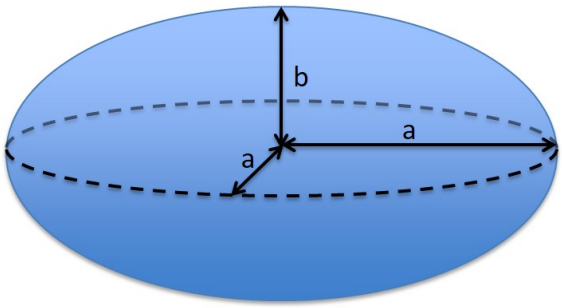

Figure 6: An oblate raindrop with a radius of b along the vertical axis of symmetry and a horizontal equatorial radius equal to a.

horizontal dimension) spheroidal shape as shown in Figure 6. A number of numerical models have been suggested for relating raindrop size to the axis ratio,

$$r = \frac{b}{a}, \tag{45}$$

where b is the radius along the axis of symmetry and a is the equatorial radius.

As discussed in Section 2.2.7, when reflecting spheroids are in the Rayleigh scattering region, the increased horizontal radius of the oblate raindrop results in an increased reflectivity in the horizontal channel relative to the vertical channel. A good but biased approximation relating the power-weighted average axis ratio,

$$\tilde{r} = \frac{\int_0^\infty r \left|S_{hh}\right|^2 p_r(r) dr}{\int_0^\infty \left|S_{hh}\right|^2 p_r(r) dr}, \tag{46}$$

and the differential reflectivity, ζ_{dr}, of an ensemble of oblate spheroidal raindrops, is [40]

$$\zeta_{dr} = \tilde{r}^{\frac{7}{3}}, \tag{47}$$

where $p_r(r)$ is the PDF of raindrop axis ratios.

2.4.4.2 Calculation

Differential reflectivity is reported in dBz and is estimated as the ratio of the horizontal and vertical linear reflectivity estimates, i.e.,

$$\begin{aligned} \hat{Z}_{DR} &= 10 \log_{10} \hat{\zeta}_{dr} \\ &= 10 \log_{10} \frac{\hat{\zeta}_h}{\hat{\zeta}_v} \\ &= \hat{Z}_H - \hat{Z}_V, \end{aligned} \tag{48}$$

where $\hat{\zeta}_h$ and $\hat{\zeta}_v$ are the linear estimated reflectivity values of the horizontal and vertical channels, respectively, and $\hat{Z}_H$ and $\hat{Z}_V$ are the corresponding reflectivity estimates reported in dBz.

2.4.5 Co-polar Correlation Coefficient

In the weather radar community, the co-polar correlation coefficient, usually referred to as *the* correlation coefficient (CC), is the magnitude of the statistical correlation between the reflected horizontally and vertically polarized signals, i.e.,

$$\rho = \left| \frac{E\left[S_{hh} S_{vv}^*\right]}{\sigma_{hh} \sigma_{vv}} \right|, \tag{49}$$

where the superscript asterisk denotes the complex conjugate, S_{hh} and S_{vv} are the zero-mean random-valued amplitude returns corresponding to the co-polar scattering coefficients of the ensemble of hydrometeors, and $\sigma_{hh} = \sqrt{E[|S_{hh}|^2]}$ and $\sigma_{vv} = \sqrt{E[|S_{vv}|^2]}$.

The CC is considered to be a good indicator of the homogeneity or heterogeneity of scatterers in a resolution volume. A value of $\rho \approx 1$ indicates highly homogeneous scatterers whereas smaller values of ρ indicate more heterogeneous scatterers.

2.4.5.1 Phenomenology

In general, differential reflectivity is considered a good indication of the average oblateness of spheroidal scatterers. It does not, however, provide any information

regarding the distribution of scatterer shape and orientation. The CC, on the other hand, when considered in conjunction with differential reflectivity, can be related to the variance of the ratios of the amplitude returns at horizontal and vertical polarization [41]. Consider the amplitude ratios of the echoes from a single hydrometeor,

$$\Upsilon_H = \frac{S_{hh}}{S_{vv}} \tag{50}$$

and

$$\Upsilon_V = \frac{S_{vv}}{S_{hh}}. \tag{51}$$

Assuming a spheroidal scatterer, the variances of Υ_H and Υ_V are a function of the linear differential reflectivity, ζ_{dr}, and the correlation coefficient, ρ [41]:

$$\sigma^2_{\Upsilon_H} = \zeta_{dr}\left(1-\rho^2\right) \tag{52}$$

and

$$\sigma^2_{\Upsilon_V} = \zeta^{-1}_{dr}\left(1-\rho^2\right). \tag{53}$$

Furthermore, in the case of equilibrium-shaped raindrops (i.e., theoretical raindrops whose shapes are no longer changing due to forces acting on the raindrop), Jameson et al. [41] has shown that the diameter variance of an ensemble of raindrops is

$$\sigma^2_D = 2.23\zeta^{-1}_{DR}\left(1-\rho^2\right). \tag{54}$$

Thus, the CC and differential reflectivity provide an approximation of the first two moments of the DSD.

2.4.5.2 Calculation

The CC estimate is simply the magnitude of the zero-lag correlation between the received signals in the horizontally and vertically polarized channels. It is estimated as

$$\hat{\rho} = \left| \frac{\frac{1}{N_p}\sum_{i=1}^{N_p} x_{h_i}(x^v_{v_i})^*}{\hat{\sigma}_{hh}\hat{\sigma}_{vv}} \right|, \tag{55}$$

where x_{h_i} and x_{v_i} are samples of the received signal in the horizontal and vertical channels, respectively,

$$\hat{\sigma}_{hh} = \sqrt{\frac{1}{N_p}\sum_{i=1}^{N_p}|x_{h_i}|^2}, \tag{56}$$

and

$$\hat{\sigma}_{vv} = \sqrt{\frac{1}{N_p}\sum_{i=1}^{N_p}|x_{v_i}|^2}. \tag{57}$$

2.4.6 Differential Phase

The WSR-88D differential phase product (or instantaneous differential phase) is the difference in phase between the received signals in the horizontally and vertically polarized channels [62]. It corresponds to the angle of the co-polar correlation term at zero lag, i.e.,

$$\phi = \arg\left[\frac{E\left[S_{hh}S_{vv}^*\right]}{\sigma_{hh}\sigma_{vv}}\right]. \tag{58}$$

While the differential phase alone is not very informative, a derived product referred to as the specific differential phase, which is the range derivative of the instantaneous differential phase, i.e.,

$$K_{DP} = \frac{d\phi}{dR}, \tag{59}$$

is a function of the scattering properties of rain [43].

2.4.6.1 Phenomenology

When an EM wave is scattered forward by raindrops, a polarization-dependent phase shift occurs over the path of propagation.[15] An incident horizontal wave on an oblate spheroid will result in a larger RCS, greater attenuation, and bigger phase shift than an incident vertical wave. The difference between the phase shifts of the forward-scattered wave in the horizontal and vertical channels is the specific differential phase.

[15] A similar polarization-dependent phase shift occurs upon backscatter, but this phase shift is considered negligible [42].

Assuming the backscatter phase shift is negligible, the one-way specific differential phase shift in radians per unit distance is

$$K_{DP} = \frac{2\pi}{k} \int_0^\infty \Re\{S_{hh}(D) - S_{vv}(D)\} N(D) dD, \tag{60}$$

where S_{hh} and S_{vv} are the forward scatter coefficients and $\Re$ denotes the real part of a complex number. An approximation relating specific differential phase, in degrees per kilometer, to underlying meteorological parameters is [43]

$$K_{DP} = \frac{108}{\pi^2} W \lambda C \left[1 - \check{r}\right],$$

where W is the LWC in units of g/m^3, C is a value that depends on the radar operational frequency, and $\check{r}$ is the mass-weighted mean axis ratio of the raindrop ensemble, i.e.,

$$\check{r} = \frac{\int_0^\infty r D^3 N(D) dD}{\int_0^\infty D^3 N(D) dD}. \tag{61}$$

2.4.6.2 Calculation

Instantaneous differential phase is estimated from the angle of the zero-lag co-polar correlation term, i.e.,

$$\hat{\phi} = \arg\left[\frac{1}{N_p} \sum_{i=1}^{N_p} x_{h_i} x_{v_i}^*\right]. \tag{62}$$

Specific differential phase is estimated as the range derivative of the differential phase, sometimes averaged over several resolution volumes along range to reduce statistical variations, i.e.,

$$\hat{K}_{DP} = \frac{\hat{\phi}_a - \hat{\phi}_b}{2\Delta_R}, \tag{63}$$

where ϕ_a and ϕ_b denote the instantaneous differential phase in range bins R_a and R_b, respectively, and $\Delta_R = R_a - R_b$. The factor of two in the denominator of (63) is required because the measured instantaneous differential phase at the radar is a result of the two-way path of propagation. In some cases, a least squares fit may also be used to estimate the specific differential phase.

2.5 Dual-Pol Radar Parameters for Tornado Detection

The measurements available as a result of the dual-pol upgrade are being incorporated into operational use by the NWS. This section illustrates the utility of some of these new measurements by discussing their application in detecting tornadic storms.

Dual-pol parameters, such as the CC and differential reflectivity, are being combined operationally with more traditional NEXRAD output, such as standard reflectivity and radial velocity, to detect low-end tornadic storms. These storms are fairly common in the winter and early spring in the southeastern U.S. They often occur late at night, are wrapped in rain, and exhibit less vertical development than storms seen later in the spring and summer severe weather season. For these reasons, these early storms are often difficult to detect by direct observation or by using the original (non-dual-pol) NEXRAD data products.

Analyzing the NEXRAD output for dual-pol tornado debris signatures (DPTDS) is a promising method for detecting these storms. DPTDS are produced by the debris that is lofted when a tornadic storm touches the ground. In addition to observing a high reflectivity value and radial velocity couplet, the data can be examined for relevant values of ρ and Z_{DR}. Specifically, areas indicative of lofted tornado debris tend to contain very low values of ρ, as the debris consists of objects with a wide variety of sizes and shapes lofted by the tornado. In addition, Z_{DR} tends to be near zero, indicating no specific preferred orientation of the debris.

Figure 7 shows reflectivity, radial velocity, differential reflectivity, and the CC for an EF3 tornadic storm that occurred near Adairsville, GA on 30 January 2013. The area affected by the tornadic storm is enclosed in the white circle in all four plots. The reflectivity plot shows a long line of storms along a squall line, but no distinctive supercell thunderstorm. Radial velocity shows a large area of circulation, but a tight couplet is not seen. There is, however, a distinct area of near-zero Z_{DR} and low ρ within the area of interest. These strong signals, associated with high reflectivity

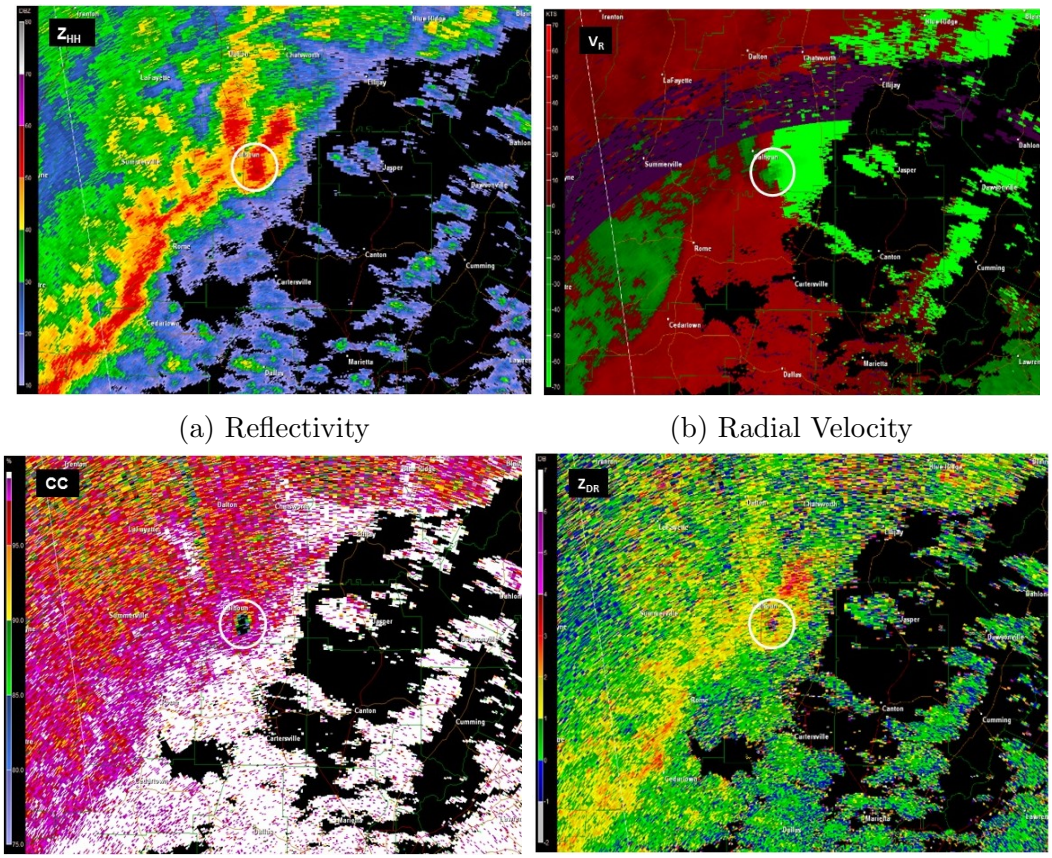

(a) Reflectivity (b) Radial Velocity

(c) Correlation Coefficient (d) Differential Reflectivty

Figure 7: Radar data products for an EF3 tornadic storm near Adairsville, GA on 30 January 2013.

and indications of rotation in the radial velocity image, allow for the detection of a tornado on the ground.

2.6 Summary

This chapter reviews the basic phenomenology of radar meteorology and the operation of the WSR-88D. The concepts described herein provide guidance on the physical significance of the level II data products provided for meteorological applications. These physical concepts provide intuition on how these data products may be applied to problems such as hydrometeor characterization, clutter identification, rain rate estimation, and detection of tornadic vortex signatures.

CHAPTER III

STATE OF THE FIELD

3.1 Overview

The purpose of this chapter is to establish the current state of the field for estimation of DSD parameters and rain rate. It provides background on current approaches and demonstrates the weather radar community's present mindset for solving these problems, which often contrasts with the principled approach used to establish performance bounds later in this dissertation.

This chapter is organized as follows. First, Section 3.2 discusses some basic concepts related to the scattering of raindrops, which are central to the estimation techniques reviewed in later sections. Section 3.3 examines various approaches for DSD estimation, and Section 3.4 follows with a discussion of the methods by which such estimators are frequently evaluated. Similarly, common approaches for rain rate estimation and evaluation of rain rate estimators are summarized in Sections 3.5 and 3.6, respectively.

3.2 Raindrop Scattering Basics

All approaches presented in this section depend on the ability to model the scattering properties of raindrops. At the operational transmit frequency of the WSR-88D ($2.7 - 3$ GHz) [60], the scattering of individual raindrops is well approximated by Rayleigh scattering theory [64]. At higher frequencies, other approaches are used, e.g., the T-matrix method [55]. For scattering calculations, the shape of a raindrop is routinely modeled as an oblate spheroid, which is fully defined by its diameter D_e and axis ratio r. Furthermore, raindrop shape models commonly assume that

a deterministic relationship exists between drop diameter and axis ratio, i.e., $r = f_r(D_e)$. This stems from the fact that larger raindrops tend to be more oblate (i.e., have a smaller axis ratio) due to various forces acting on the raindrop as it falls.

3.3 DSD Parameter Estimation

Since the advent of the WSR-88D dual-pol upgrade and the formulation of the gamma DSD model, three primary approaches have been suggested for estimating the parameters of a gamma DSD from dual-pol measurements: the beta method, the Constrained-Gamma (CG) method, and a neural network approach. Each is distinguished not only by the applied technical methodology but also by the modeling assumptions employed as part of the problem formulation.

3.3.1 Beta Method

3.3.1.1 Model Assumptions

Recall from Section 3.2 that it is standard to assume a known relationship between r and D_e of a raindrop. The beta method [31, 32, 29, 13] assumes a linear model for this relationship:

$$r = 1.03 - \beta D_e, \tag{64}$$

where β is a slope parameter. This relation is consistent with the model of Pruppacher and Beard [65], one of the first empirical fits ever proposed for relating r and D_e, where $\beta = 0.62$. The beta method, however, treats the slope parameter as an unknown variable that is estimated from the radar observables along with the DSD parameters. Gorgucci et al. [31] believes this technique accounts for effects due to different canting distributions and modes of raindrop oscillation in various meteorological conditions.

3.3.1.2 Technical Approach

The beta method applies nonlinear regression analysis to simulated data to estimate the functional relationship between the unknown parameters, $X = [\beta\ N_o\ \mu\ \Lambda]^T$, and

the radar measurements, $Y = [Z_H\ Z_{DR}\ K_{DP}]^T$. Regression is the statistical process of estimating the model coefficients, ω, that define the relationship between the observed data, Y, and the model parameters, X; e.g., the estimate of X given ω is

$$\hat{X}_{nlr} = g_{nlr}\left(Y;\omega\right). \tag{65}$$

In the case of nonlinear regression, the relationship is modeled by a nonlinear function, $g_{nlr}\left(Y;\omega\right)$, of the estimated coefficients.

The beta method solution requires training on a simulated data set. Thus, the resulting solution is in part determined by the prior distribution on X that was employed to generate the simulated data. The chosen priors, however, are not necessarily representative of the true distribution of model parameters [11]. They are simply selected to include the range of values expected to be encountered in realistic DSDs. Clearly, the beta method solution is dependent on the selection of the prior since it proposes to solve for four unknown model parameters given three radar measurements. In the context of this approach, it might be more appropriate to treat β as a nuisance parameter[1] in a Bayesian framework and choose priors with more discretion.

3.3.2 Constrained-Gamma Method

3.3.2.1 Model Assumptions

The CG method [94, 21, 22] uses the radar observables $Y = [Z_H\ Z_{DR}]^T$, choosing not to use K_{DP} since it cannot be derived from a single resolution volume. Accordingly, to make DSD estimation a two-parameter problem, the CG method applies a constraint on the values of μ and Λ, a relationship supported by numerous independent disdrometer data collections. The constraining mathematical $\mu - \Lambda$ relation is approximated from experimental data by a second-order polynomial with coefficients

[1] A nuisance parameter is an unknown parameter that is not of interest but merely complicates the estimation problem [45].

determined by linear regression [10]:

$$\Lambda(\mu) = 1.935 + 0.735\mu + 0.0365\mu^2. \tag{66}$$

For the $r - D_e$ relation, the CG model uses a deterministic function, $r = f_r(D_e)$ that is also based on experimentally collected disdrometer data.

3.3.2.2 Technical Approach

The original CG method [94] uses an "iterative procedure" to solve the system of equations relating the DSD parameter set, $X = [N_o\ \mu]^T$ (or, equivalently, $X = [N_o\ \Lambda]^T$), with the expected value of the radar measurements, $Y = [Z_H\ Z_{DR}]^T$. Given that the radar measurements are MLEs of their true expected values [76], the CG solution corresponds to the MLE of the DSD parameter set under the CG model. This follows from the functional invariance property of the MLE [45]. The MLE is the value of the model parameters that maximizes the likelihood of the observed data, i.e.,

$$\hat{X}_{mle} = \arg\max_X p_Y(Y; X), \tag{67}$$

where Y is the observed data and X is the unknown parameter set.

The CG model has also been applied using a Bayesian approach [21]. In the Bayesian paradigm, the posterior probability of the unknown random parameter set, $X = [N_o\ \mu]^T$, given the observations, $Y = [Z_H\ Z_{DR}]^T$, is

$$p_{X|Y}(X|Y) = \frac{p_{Y|X}(Y|X)\, p_X(X)}{p_Y(Y)}, \tag{68}$$

where $p_{Y|X}(Y|X)$ is the likelihood of the data given the parameter set X, $p_X(X)$ is the prior distribution on the unknown parameters, and $p_Y(Y)$ is the marginal probability of the observed data. Assuming the model of Cao et al. [21] is valid, the provided solution is the minimum mean-square error (MMSE) estimate of X, i.e.,

$$\begin{aligned} \hat{X}_{mmse} &= \arg\max_\chi \int_0^\infty ||X - \chi||^2\, p_{X|Y}(X|Y)\ dX \\ &= \int_0^\infty X p_{X|Y}(X|Y)\ dX, \end{aligned} \tag{69}$$

where $||\cdot||$ denotes the l^2 norm. However, the model employed by Cao et al. [21] is an ad hoc approximation for the true joint distribution of the radar measurements.

Most recently, the CG model has been incorporated into a variational scheme as well [22]. This approach is a method for spatial data assimilation in which one strives to minimize a cost function. Based on certain assumptions, such as a Gaussian error structure and exponential spatial correlation of the model variables, the posterior distribution may be written as

$$P_{X|Y}\left(X|Y\right) = \frac{1}{Q} e^{-C(X,Y)}, \tag{70}$$

where $C\left(X,Y\right)$ is the cost function and Q is a normalization factor. In the variational scheme, X and Y refer to the model parameters and measurements, respectively, for several radar resolution volumes over a multi-dimensional grid. Under the given model, minimization of the cost function provides the joint maximum a posteriori (MAP) estimate for the DSD parameters over that grid. The MAP estimate is the value of the model parameters that maximizes the posterior probability of the unknown model parameters, i.e.,

$$\hat{X}_{map} = \arg\max_{X} p_{X|Y}\left(X|Y\right). \tag{71}$$

3.3.3 Neural Network Approach

3.3.3.1 Modeling Assumptions

The modeling assumptions applied in the neural network approach [88] are fairly straightforward. A set of well-known, experimentally established deterministic models is chosen to relate the raindrop diameter and axis ratio. Based on this fact, there is a deterministic mapping from the DSD parameters, $X = \left[N_o\ \mu\ \Lambda\right]^T$, to the expected value of the radar measurements, $Y = \left[Z_H\ Z_{DR}\ K_{DP}\right]^T$.

3.3.3.2 Technical Approach

Using simulated data, Vulpiani et al. [88] trains a neural network to estimate the DSD parameters, $X = [N_o\ \mu\ \Lambda]^T$, from the radar measurements, $Y = [Z_H\ Z_{DR}\ K_{DP}]^T$. A neural network is a specific type of nonlinear regression model performed in multiple stages that is designed to model the operation of neurons in the human brain [35]. Given a set of inputs, Y, a nonlinear function, $g_{nn}(\bullet)$, called a node, computes a set of derived features, $A_1 = [A_1(1)...A_1(M)]^T$. The m^{th} derived feature of the input layer is

$$A_1(m) = g_{nn}\left(w_{1,m}^0 + w_{1,m}^H Y\right), \tag{72}$$

where $w_{1,m}$ and $w_{1,m}^0$ signify a weight vector and bias term, respectively, which are estimated using regression, $\bullet^H$ denotes the Hermitian (i.e., conjugate transpose), and the subscript one signifies the set of input nodes is the first "layer" of the neural network. In a multi-layer architecture, the first layer of derived features, obtained from the input, feeds another layer that generates a new set of derived features, and so on; i.e., the m^{th} feature of the l^{th} layer is

$$A_l(m) = g_{nn}\left(w_{l,m}^0 + w_{l,m}^H A_{l-1}\right). \tag{73}$$

The estimated parameters, $\hat{X}_{nn}$, are expressed as a linear combination of the final layer of derived features,

$$\hat{X}_{nn} = w_L^0 + w_L^T A_L, \tag{74}$$

where A_L signifies the derived features of the final hidden layer of an L-layer neural network.

3.4 Evaluation of DSD Estimators

As of yet, little consideration has been given to the theoretical treatment of DSD estimator performance. Typically, to evaluate DSD parameter-estimation performance,

estimators are applied to one of two types of data: simulated [29, 88, 2] or experimentally collected [13, 11, 94, 88, 2, 10]. Then, a set of metrics is applied to benchmark estimator performance. A discussion of the merits and vices of simulated and experimentally collected data is given in Section 3.4.1. Then, Section 3.4.2 summarizes the metrics frequently used to describe estimator performance.

3.4.1 Data Merits

Simulated data is generally inexpensive to generate, and the quality of the data is often more easily verified than experimentally collected data. For this reason, simulated data is frequently used for the evaluation and comparison of the techniques described in Section 3.3 [29, 88, 2]. The primary drawback of simulated data, however, is that it requires a known model to generate the data. For DSD estimation, each of the three techniques presented in Section 3.3 operate under different modeling assumptions. By choosing a particular model to perform a simulation, one inherently elects the best estimator. Furthermore, a Monte Carlo simulation requires the adoption of a prior distribution on the model parameters. In many cases, the selection of the prior is likely to have a direct impact on the outcome of the performance analysis. Most often, simulated data is generated assuming independent uniform prior distributions on $\log_{10}(N_w)$, D_o, and μ. While these priors include the span of values likely to be encountered in precipitation, they are unlikely to be representative of the true distribution [11].

The primary advantage of experimentally collected data is that a known data model is not required. Rather, the validity of the proposed models may be tested. Nevertheless, reliable experimentally collected data is often difficult to obtain. It requires collection of radar data and corresponding disdrometer measurements as ground truth, the temporal and spatial synchronization of which is often a challenge. Additionally, measurements are subject to experimental error. Further, it is difficult,

if not impossible, to verify that the collected data is representative of the gamut of DSD parameter values that may be encountered in the diverse array of possible climatological settings.

3.4.2 Measures of Estimator Performance

A number of metrics are usually computed to assess estimator performance. These include the statistical correlation between true and estimated parameter values, the sample mean of the estimator bias, the root mean-square error (RMSE), and the coefficient of determination [94, 88, 2]. While these metrics summarize estimator performance over the parameter set represented by the test data, they do not provide a method for reliably characterizing performance as a function of all variables that influence estimator results, e.g., DSD and radar parameters.

As mentioned previously, the theoretical treatment of DSD estimator error is scant in the current literature. However, Brandes et al. [11] does apply error propagation to examine the impact of measurement errors on DSD parameters for the beta method. Error propagation is a method of analysis for understanding how the error or uncertainty of random variables may impact functions of that random variable. For nonlinear functions $X = f_X(Y)$, where $Y = [Y(1)\, Y(2) \ldots Y(M)]^T$, the analysis may be performed by applying a first-order Taylor series expansion about a point, Y^o:

$$f_Y(Y) \approx f_Y(Y^o) + \sum_{m=1}^{M} \frac{df_Y(Y^o)}{dY(m)} (Y - Y^o). \tag{75}$$

Then, with the simplifying assumption made by Brandes et al. [11] that the measurement errors are independent, the variance of $X = f_Y(Y^o)$ is approximated as

$$\sigma_X^2 \approx \sum_{m=1}^{M} \left| \frac{df_Y(Y^o)}{dY(m)} \right|^2 \sigma_{Y(m)}^2, \tag{76}$$

where $\sigma_{Y(m)}^2$ is the measurement error variance. However, the assumption of independent measurement errors is frequently invalid. Furthermore, error propagation

operates under the assumption that the only source of estimation errors are the result of measurement errors. Contrastingly, the beta method model estimates four unknown parameters from three measurements, which makes such a relationship impossible.

3.5 Rain Rate Estimation

Rain rate estimation is a fundamental problem of interest in radar meteorology, which is inherently related to DSD estimation. As such, a number of techniques have been proposed to estimate rain rate from radar measurements. These approaches are divided into two categories. The first category estimates the DSD and then proceeds to extrapolate rain rate based on the retrieved DSD parameters. The second category seeks to parametrically relate rain rate directly to radar measurements, bypassing DSD estimation as a step.

3.5.1 DSD-Based Approaches

The approaches described in this section are based on the idea that once DSD parameters are estimated from radar measurements, rain rate is easily inferred from the DSD parameters. Thus, the procedures described in this section are merely the DSD estimation approaches discussed in Section 3.3, but extended to the rain rate estimation problem.

Bringi et al. [16] extends the beta method to provide a power-law estimator for rain rate. They suggest that the relationship between rain rate and reflectivity is well modeled as

$$\hat{R}_r\left(Z_H\right) = a\left(X\right)\zeta_h^{1.5}, \tag{77}$$

where $\hat{R}_r$ is the estimated rain rate and $a\left(X\right)$ is a function of the retrieved DSD parameters estimated using the beta method.[2]

[2]While power-law estimators may use the linear scale measurements, e.g., ζ_h, as input, it is common notation to signify the rain rate estimator as a function of their logarithmic counterpart,

To estimate rain rate, DSD parameters estimated with the CG method [94, 10] and the neural network approach [88] have been applied to a direct mapping between rain rate and the DSD parameters (i.e., $R_r = f_{R_r}(X)$). Given that the CG method yields the MLE of the DSD parameters, the rain rate estimate is also the MLE under that model.

3.5.2 Non-DSD-Based Approaches

The methods described in this section are among the more conventional rain rate estimators. In these approaches, DSD estimation is not a preliminary step in the estimation process; however, this is not to say that the role of the DSD in rain rate is ignored. Radar measurements are often collected or simulated for a range of realistic DSD parameters such that a direct relationship between rain rate and radar measurements can be estimated. General nonlinear regression, neural networks, and the probability matching method (PMM) are all technical approaches that have been applied in this context for rain rate estimation.

3.5.2.1 Nonlinear Regression

Several estimators that parametrically relate radar measurements to instantaneous rain rate through a power-law relation have been determined using nonlinear regression. Since the WSR-88D was first deployed as a single-polarization radar, reflectivity was originally the only available radar-based measurement for inferring rain rate, leading to several estimators of the form

$$\hat{R}_r(Z_H) = a\zeta_h^b, \tag{78}$$

where a and b are the regression coefficients. The coefficients used in (78) are highly variable. Countless variants for the estimator coefficients of (78) have been recommended in the literature [4]. Most often, the specific set of coefficients chosen is based

e.g., $\hat{R}_R(Z_H)$.

on the type of precipitation under observation, e.g., stratiform, convection, or orographic. In general, such estimates are subject to large errors since a unique mapping between reflectivity and rain rate does not exist.

After the dual-pol upgrade of the WSR-88D, improvements in rain rate estimation came in the form of other power-law estimators similar to (78), but with the addition of other data products, e.g., $\hat{R}_r\left(Z_H, Z_{DR}\right)$ [28], $\hat{R}_r\left(K_{DP}\right)$ [75], and $\hat{R}_r\left(K_{DP}, Z_{DR}\right)$ [9].

3.5.2.2 Neural Networks

Neural networks have been applied for estimating rain rate from radar measurements as well [52, 92, 88]. As explained in Section 3.3.3, neural networks are also a form of nonlinear regression; however, they have a specific parametric form modeled after the operation of neurons in the human brain. The relationship between radar measurements and rain rate can be well approximated by a neural network given appropriate training data. As cited in Vulpiani et al. [88], it has been proven that a single hidden layer neural network is capable of representing any continuous nonlinear function.

3.5.2.3 Probability Matching Method

PMM [74, 20] strives to match the sample cumulative distribution functions (CDF) of rain rate, $F_{\hat{R}_r}\left(\hat{R}_r\right)$, and reflectivity, $F_{Z_H}\left(Z_H\right)$. PMM assumes reflectivity is related to rain rate by a unique monotonic function (i.e., $R_r = g_{pmm}\left(Z_H\right)$) such that

$$F_{R_r}\left(R_r\right) = F_{Z_H}\left(g_{pmm}^{-1}\left(R_r\right)\right), \tag{79}$$

where $g_{pmm}^{-1}\left(\bullet\right)$ denotes the inverse function of $g_{pmm}\left(\bullet\right)$. Given the sample CDFs of rain rate and reflectivity, the function $g_{pmm}\left(Z_H\right)$ is estimated (usually non-parametrically) so that (79) holds true for the sample CDFs. An extension to traditional PMM [30], applying both Z_H and Z_{DR}, has been implemented as well.

One of the more attractive features of PMM is that it does not require temporal

or spatial synchronization of radar measurements with rain gauge records when collecting data to characterize the CDFs of rain rate and reflectivity. However, given the possible variations in DSDs, the assumption of a unique monotonic function relating Z_H and R_r is clearly invalid.

3.6 Evaluation of Rain Rate Estimators

The methods and metrics normally used for the evaluation of rain rate estimators are consistent with those used for DSD estimation. Estimators are applied to either simulated [28, 8] or experimentally collected [16, 10, 52, 92] data. Then, performance is quantified with metrics such as statistical correlation between true and estimated rain rate, the sample mean of the estimator bias, the RMSE, and the coefficient of determination [10, 16, 28, 52, 92, 8].

Little work has been done in terms of theoretical performance bounds of rain rate estimation. However, for power-law estimators, error propagation has been considered as a method of evaluating the impact of measurement errors on estimator performance [23]. For example, given a simple power-law estimator, $\hat{R}_r\left(Z_H\right) = a\zeta_h^b$, the estimator variance that results from measurement errors distributed with zero-mean and variance of $\sigma_{\zeta_h}^2$, is

$$\sigma_{\hat{R}_r(Z_H)}^2 = \sigma_{\zeta_h}^2 a^2 b^2 \zeta_h^{2(b-1)}. \tag{80}$$

This method provides the estimator variance resulting from measurement error. However, since a unique mapping relating rain rate to reflectivity does not exist, additional errors are present in reflectivity-based estimators. Error propagation does not account for this fact.

3.7 Summary

This chapter reviewed various suggested approaches for estimation of DSD parameters and rain rate, along with the methods by which these estimators are often evaluated.

Further, it demonstrated the extensive effort put forth by the weather radar community to find solutions to these problems. Despite all the effort put forth to solve these problems, no one as yet attempted to determine potentially how well any of these estimators could perform given the available dual-pol data. Thus, this chapter also sets the stage for the remainder of this dissertation, which strives to establish performance bounds for these estimators.

CHAPTER IV

MAPPING DROP SIZE DISTRIBUTION PARAMETERS TO RADAR MEASUREMENTS

4.1 Overview

Regardless of the approach taken to estimate DSD parameters, a functional mapping relating the dual-pol radar measurements to the DSD parameters is the ultimate goal of the DSD estimation problem. This mapping may be determined explicitly based on the underlying physics, or it may be learned implicitly via data mining techniques. In general, data mining approaches are suitable for estimation problems in which the physical models are unavailable. Despite the fact that the physical scattering properties of raindrops are well understood, the data mining approach is still frequently used [13, 29, 88] because the complicated mathematical relationships between these quantities are difficult to work with directly.

The objective of this chapter is to establish closed-form mathematical expressions that suitably approximate the mathematical relationship between the DSD parameters of rain and the expected value of the dual-pol radar measurements. To our knowledge, the only previous attempt to do something similar is [94], where the scattering coefficients of raindrops, assuming a deterministic relationship between raindrop size and shape, are fit to a power law. However, [94] makes no effort to extend this mapping to other models for the axis ratio of raindrops. Further, the quality of the approximations provided in [94] is not quantified.

To develop the proposed relationship, Section 4.2 begins by reviewing the scattering properties of individual raindrops. Section 4.3 discusses the shape model for individual raindrops so the applicable scattering theory may be applied. Section 4.4

applies the shape model and scattering theory to an ensemble of raindrops, formulating how each each of the dual-pol radar measurements relate to the properties of the raindrop ensemble. The resulting mathematical relationships developed in this section involve an integral that is only computable via numerical integration. Thus, Section 4.5 proposes closed-form expressions that approximate the mathematical formulations presented in Section 4.4. Then, Section 4.6 seeks to estimate the parameters that yield the best approximations for the proposed closed-form expressions. Next, Section 4.7 evaluates how well the proposed approximations model the actual relationship between the DSD parameters and radar measurements. Lastly, Section 4.8 summarizes our conclusions.

4.2 Scattering Properties of Individual Raindrops

In general, properties of a scattered EM wave depend on the scattering object's attributes (such as size, shape, composition, and orientation) and characteristics of the incident EM wave (such as polarization and frequency). Recall from Section 2.2.7 that the polarization-dependent scattering of an incident EM wave can be expressed in terms of a scattering matrix, S:

$$\begin{bmatrix} E_h^s \\ E_v^s \end{bmatrix} = \frac{e^{-jkR}}{R} \underbrace{\begin{bmatrix} S_{hh} & S_{hv} \\ S_{vh} & S_{vv} \end{bmatrix}}_{S} \begin{bmatrix} E_h^i \\ E_v^i \end{bmatrix}. \tag{81}$$

The scattering matrix, which is also a function of the direction of scatter, reveals how the reflecting object affects the incident wave in terms of polarization, amplitude, and phase shifts [57]. This section presents the scattering coefficients of a raindrop.

The scattering coefficients of raindrops are commonly computed assuming spheroidally shaped raindrops with diameter D_e and axis ratio r. Also, since raindrops are significantly smaller than the wavelength of many weather radars, the Rayleigh approximation is frequently used for computing their scattering coefficients. The Rayleigh

scattering model is valid as long as the incident EM field penetrates the entire raindrop sufficiently fast that an electrostatic solution is a valid approximation. This requires the particle size be "small" compared to the wavelength of the EM field. For a sphere, this requirement is stated as

$$\left|\frac{\pi D}{\lambda}\right| \ll 1, \tag{82}$$

where D is the sphere diameter and λ is the wavelength. A second criterion is [84]

$$\left|\frac{\pi D}{\lambda}\sqrt{\epsilon_r}\right| \ll 1, \tag{83}$$

where ϵ_r is the dielectric constant of the scatterer. Of the two criteria, (83) is the more stringent condition for this application since water has a refractive index approximately equal to nine (or, equivalently, a dielectric constant of 81) at S-band, the operational frequency band of many weather radars, e.g., the WSR-88D. Nonetheless, the Rayleigh approximation of the RCS of a raindrop has been verified to be within 1.5 dB of the true RCS value at S-band as long as $D_e < 0.07\lambda$ [4]. This equation is satisfied for the range of realistic drop sizes as raindrops rarely exceed 6 mm in diameter [15].

In the Rayleigh regime, the forward and backward scattering coefficients of raindrops with a vertically oriented axis of symmetry are identical; therefore, the equations in this section may be employed for both forward and backward scatter [64]. For a raindrop with a vertically oriented axis of symmetry, the off-diagonal entries of the scattering matrix (i.e., S_{hv} and S_{vh}) are zero and the diagonal entries are given as [15]

$$S_{hh}\left(r, D_e, \psi\right) = \frac{k^2}{4\pi} V \alpha_h\left(r\right) = \frac{k^2}{24} D_e^3 \alpha_h\left(r\right) \tag{84}$$

and

$$S_{vv}\left(r, D_e, \psi\right) = \frac{k^2}{4\pi} V \alpha_v\left(r\right) = \frac{k^2}{24} D_e^3 \alpha_v\left(r\right), \tag{85}$$

where $k = \frac{2\pi}{\lambda}$ is the wave number, V is the volume of the raindrop, $\alpha_h\left(r\right)$ and

$\alpha_v(r)$ are the axis ratio-dependent part of the polarizability terms,[1] and ψ denotes the direction of scatter as either forward ($\psi = 0$) or backward ($\psi = \pi$).[2] The axis ratio-dependent part of the polarizability terms are

$$\alpha_h(r) = \frac{(\epsilon_r - 1)}{1 + \frac{1}{2}(1 - \lambda_z)(\epsilon_r - 1)} \tag{86}$$

and

$$\alpha_v(r) = \frac{(\epsilon_r - 1)}{1 + \lambda_z(\epsilon_r - 1)}, \tag{87}$$

where λ_z is the depolarizing factor. The depolarizing factor for an oblate ($r < 1$) and prolate ($r > 1$) spheroid are

$$\lambda_z = \frac{1 + \varepsilon_o^2}{\varepsilon_o^2}\left(1 - \frac{1}{\varepsilon_o}\tan^{-1}(\varepsilon_o)\right) \tag{88}$$

and

$$\lambda_z = \frac{1 - \varepsilon_p^2}{\varepsilon_p^2}\left(-1 + \frac{1}{2\varepsilon_p}\ln\left(\frac{1 + \varepsilon_p}{1 - \varepsilon_p}\right)\right), \tag{89}$$

respectively, where the spheroid eccentricities are

$$\varepsilon_o = \sqrt{\frac{1}{r^2} - 1} \tag{90}$$

and

$$\varepsilon_p = \sqrt{1 - \frac{1}{r^2}}. \tag{91}$$

The scattering coefficients of a 1 mm diameter raindrop, computed from these equations, are plotted as a function of axis ratio in Figure 8.

The above equations indicate some primary concepts for inferring information regarding the size and shape of raindrops. First, a horizontally (or vertically) polarized incident wave remains horizontally (or vertically) polarized upon reflection. Second, as raindrop size increases, the scattering coefficients increase. Lastly, as the axis ratio

[1]The polarizability term is the product of V and $\alpha_h(r)$ or $\alpha_v(r)$, i.e., $V\alpha_h(r)$ and $V\alpha_v(r)$.

[2]While the scattering coefficients are identical for forward and backward scatter and, therefore, not written as a function of ψ, this dissertation uses this notation to delineate between the phenomena of forward and backward scatter as they relate the radar measurements.

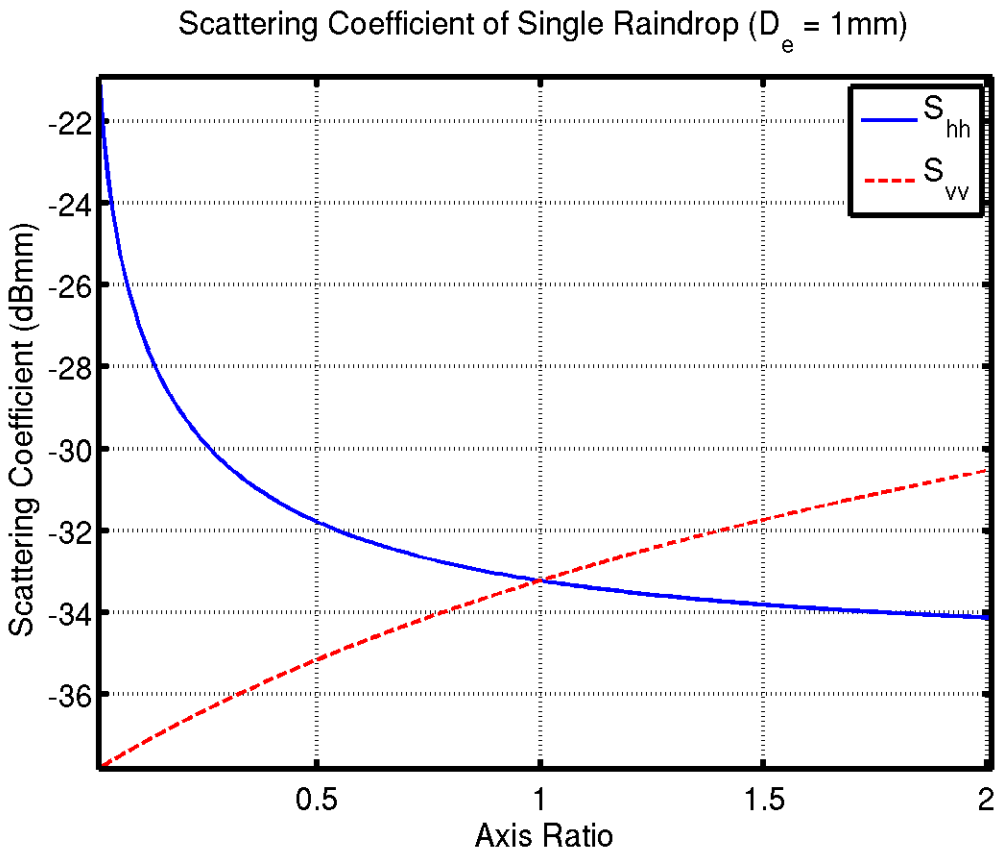

Figure 8: Horizontal and vertical scattering coefficients of 1 mm diameter raindrop as a function of axis ratio

of the raindrop decreases, the horizontal scattering coefficient increases relative to the vertical scattering coefficient. These facts, combined with the phenomenology for relating raindrop size and shape (discussed in Section 4.3), are the primary enabling concepts for inferring the DSD from dual-pol radar measurements.

4.3 Raindrop Shape Model

The shape of raindrops influences their scattering coefficients and, thus, impacts the relationship between the DSD parameters and radar measurements. Due to the limited number of observable measurements provided by a dual-pol radar, the weather radar community has exerted significant effort in defining constraining relationships between raindrop size and shape. This section provides a survey of current models

for these relationships.

4.3.1 Mean Axis Ratio

While small raindrops are approximately spherical, larger raindrops take on a more oblate shape due to surface tension, hydrostatic pressure, and aerodynamic forces. The shape of a raindrop falling at terminal velocity with all forces in balance is termed the equilibrium shape. Multiple theoretical models for the equilibrium axis ratio of spheroidal raindrops have been developed [65, 33, 5]. However, it is now widely accepted that most raindrops do not fall in perfect equilibrium. Thus, to characterize the mean axis ratio of raindrops as a function of diameter, large quantities of disdrometer data have been collected. Using the collected data, several numerical models based on polynomial least-squares fits have been suggested for relating the diameter of a raindrop to its expected axis ratio. For the mathematical relationships derived in this chapter, we consider three different models for the mean axis ratio of a raindrop: Beard and Chuang [5], Andsager et al. [3] (which combines Beard and Chuang's model with empirical data), and Brandes et al. [9]. These three models are plotted in Figure 9.

The Beard and Chuang model is one of the more commonly used theoretical equilibrium models and is given by [5]

$$\mu_r\left(D_e\right) = 1.012 - 0.01445 D_e - 0.01028(D_e^2). \tag{92}$$

The Andsager model [3] suggests applying the Beard and Chuang equilibrium model, given in (92), to raindrops between one and four millimeters in diameter and, for raindrops outside this range, applying their empirical fit to experimental data, given by

$$\begin{aligned}\mu_r\left(D_e\right) = 1.0048 + 5.7 \times 10^{-4} D_e - 2.628 \times 10^{-2} D_e^2 \\ + 3.682 \times 10^{-3} D_e^3 - 1.677 \times 10^{-4} D_e^4.\end{aligned} \tag{93}$$

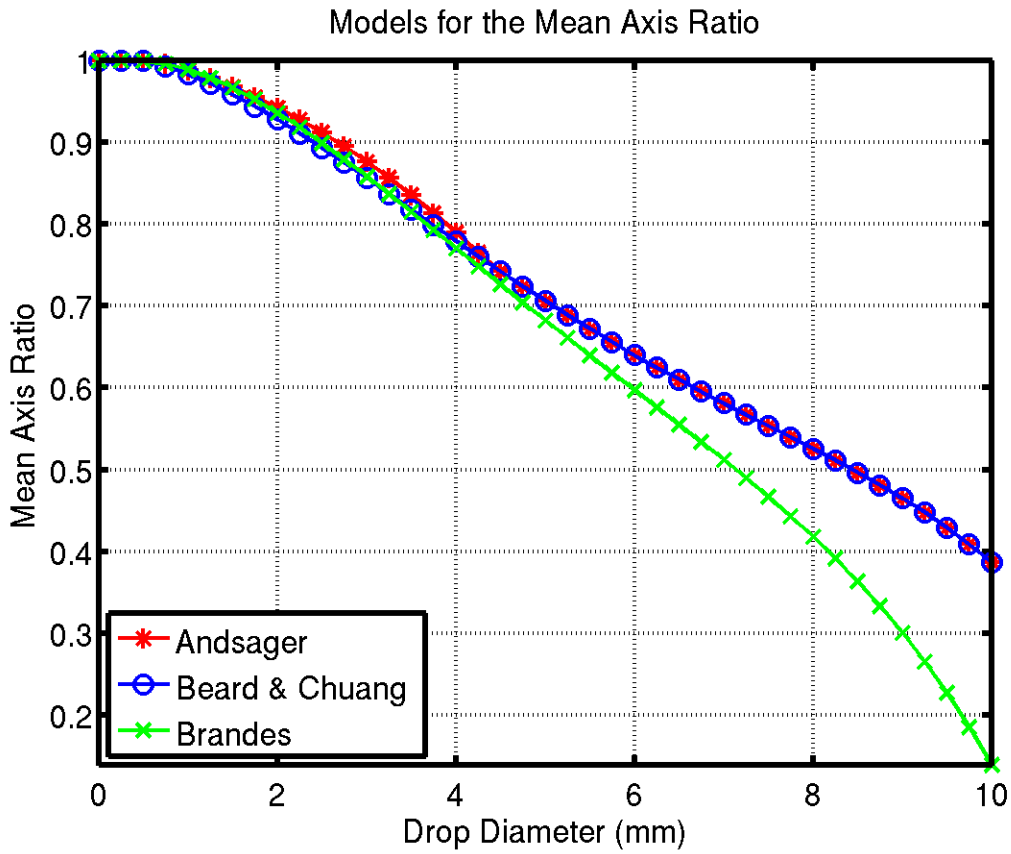

Figure 9: Models for the mean axis ratio of a raindrop as a function of drop diameter

The resulting model accommodates for the apparent upward shift in mean axis ratios observed in experimentally collected data relative to the theoretical equilibrium axis ratio. Another empirical axis ratio model, applied in DSD estimation, is the model of Brandes et al. [9]:

$$\mu_r\left(D_e\right) = 0.9951 + 0.0251 D_e - 0.03644 D_e^2 + 0.00503 D_e^3 - 0.0002492 D_e^4. \tag{94}$$

For $D_e \leq 4$ mm, this model yields values similar to the other more commonly used models presented in this section. However, the curve deviates considerably for larger drop diameters, modeling large drops as extremely oblate.

4.3.2 Axis Ratio Distribution

While the mean axis ratio models described in Section 4.3.1 may well approximate the average axis ratio of a raindrop as a function of size, shape oscillations typically

occur, which result in a distribution of axis ratios for a given drop size. Much of the original literature disregards the random variation of raindrop axis ratios, implicitly assuming an axis ratio standard deviation of zero, i.e., $\sigma_r = 0$. Based on collected data, however, axis ratios are well approximated by a Gaussian distribution with a non-zero variance. Two primary models have been suggested in the literature for the standard deviation of raindrop axis ratios. Bringi et al. [14] suggests a standard deviation proportional to the expected axis ratio of a raindrop,

$$\sigma_r\left(D_e\right) = 0.068\mu_r\left(D_e\right), \tag{95}$$

regardless of drop size, while Jameson [40] suggests a standard deviation of

$$\sigma_r\left(D_e\right) = \begin{cases} 0.13 - 0.025D_e & : \quad D_e < 2.755 \\ -0.016 + 0.028D_e & : \quad D_e \geq 2.755\ . \end{cases} \tag{96}$$

In general, the PDF of the raindrop axis ratio is conditioned on the diameter of the rain drop:

$$p_{r|D_e}(r|D_e) = \frac{1}{Q} e^{-\frac{(r-\mu_r(D_e))^2}{2\sigma_r^2(D_e)}} \qquad r > 0, \tag{97}$$

where Q is a normalization factor, $\mu_r\left(D_e\right)$ is the diameter-dependent mean axis ratio, and $\sigma_r\left(D_e\right)$ is the diameter-dependent standard deviation. The Gaussian distribution is truncated here due to the lack of physical meaning associated with a negative axis ratio.

For the numerical model presented in this chapter, we consider the truncated Gaussian PDF of (97) with three different models for the axis ratio standard deviation: the zero-variance model, the proportional model of Bringi et al. [14] given in (95), and the model of Jameson [40] given in (96). The standard deviation as a function of the axis ratio is shown in Figure 10 for each standard deviation model. The proportional model of Bringi et al. is plotted for each of the mean models, since it depends on the model used for the mean axis ratio.

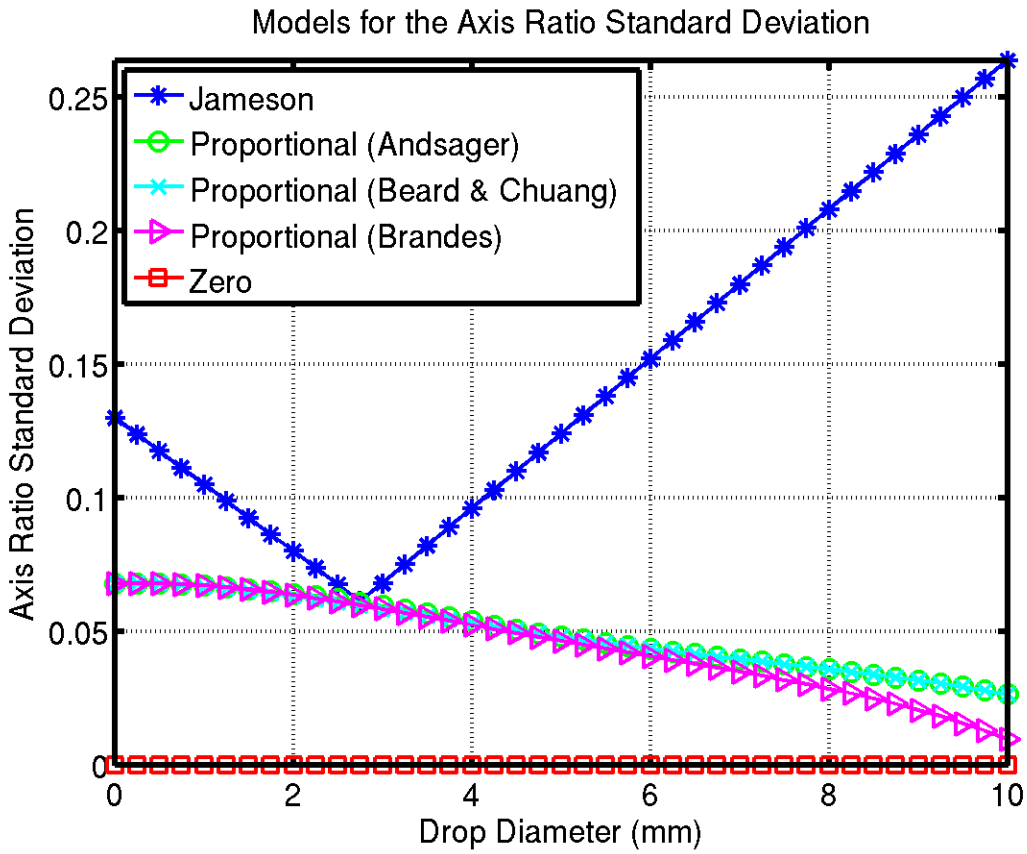

Figure 10: Models for the standard deviation of the axis ratio of a raindrop as a function of drop diameter

4.3.3 Orientation

Equations (84) and (85) for the scattering coefficients of a raindrop assume a vertically oriented axis of symmetry. However, raindrops rarely fall with a perfectly vertical orientation, and the true canting angle of a raindrop alters its scattering coefficients. Nonetheless, theoretical distributions in conjunction with observations indicate that raindrop canting angles are narrowly distributed with a mean near zero [6]. As a result, the effects of canting are considered negligible and are ignored in common practice [37, 77]. This dissertation follows this convention. As a result,

cross-polarization returns are considered insignificant.[3]

4.4 Scattering Properties of a Raindrop Ensemble

Of the six level II data products reported by the WSR-88D, four are relevant to the DSD estimation problem: horizontal reflectivity factor, vertical reflectivity factor (or differential reflectivity), specific differential phase, and the CC. How each measurement is mathematically related to the DSD is discussed in detail in this section. Based on scattering phenomenology and raindrop shape models, a functional relationship between the DSD of rain (i.e., the raindrop ensemble) and the radar measurements is given.

4.4.1 Reflectivity

Recall from Section 2.4.1 that reflectivity of rain is proportional to the expected value of the per unit volume RCS of rain:

$$\zeta = \frac{\lambda^4 \eta}{\pi^5 \left|K\right|^2}. \tag{98}$$

This relation is true for the co-polarized returns in both the horizontal and vertical channels; i.e., $\zeta_h \propto \eta_h$ and $\zeta_v \propto \eta_v$, where η_h and η_v are the expected unit volume RCSs and ζ_h and ζ_v are the linear reflectivity values for the horizontal and vertical polarizations, respectively.

While the unit volume RCS is a random variable due to randomized constructive and destructive interference of multiple scatterers, its expected value, η, is equal to the sum (or integral) of the RCS of all individual scatterers (assuming non-coherent scatter). Given the DSD of the observed raindrop ensemble, $N\left(D_e; X\right)$, and the raindrop axis ratio PDF, $p_{r|D_e}\left(r|D_e\right)$, the expected unit volume RCS of rain in the

[3]Since the cross-polarization returns due to rain are considered negligible, the remainder of this dissertation refers to the returned signal from horizontal transmit, horizontal receive as simply horizontal and to the returned signal from vertical transmit, vertical receive as simply vertical.

horizontal channel is

$$\eta_h = 4\pi \int_0^\infty \int_0^\infty |S_{hh}(r, D_e, \pi)|^2 N(D_e; X) p_{r|D_e}(r|D_e)\, dr\, dD_e. \tag{99}$$

The expected unit volume RCS in the vertical channel, $\eta_v(X)$, is analogous to (99), simply replacing $S_{hh}(r, D_e, \pi)$ with $S_{vv}(r, D_e, \pi)$.

4.4.2 Differential Reflectivity

The discussion of reflectivity in Section 4.4.1 is valid for both horizontal and vertical polarizations. However, it is standard practice to report differential reflectivity, ζ_{dr}, in place of vertical reflectivity. Recall from Section 2.4.4, differential reflectivity is the ratio of the power received in the horizontal and vertical polarization channels. Given the horizontal reflectivity, the conversion between ζ_{dr} and ζ_v is straightforward. For mathematical simplicity, this dissertation works directly with vertical reflectivity rather than differential reflectivity. However, it is an aspiration of this research that the mathematical approximations sought for horizontal and vertical reflectivity also yield an appropriate approximation for differential reflectivity.

4.4.3 Specific Differential Phase

Recall from Section 2.4.6 that specific differential phase is the difference between the phase shifts in the horizontal and vertical channels. Like reflectivity, the specific differential phase is a random variable. The one-way expected specific differential phase, K_{DP}, given in units of $\frac{\text{rad}}{\text{km}}$, is

$$K_{DP} = \frac{2\pi}{k} \int_0^\infty \int_0^\infty \Re\{S_{hh}(r, D_e, 0) - S_{vv}(r, D_e, 0)\} N(D_e; X)\, p_{r|D_e}(r|D_e)\ dr\, dD_e. \tag{100}$$

Small, spherical raindrops do not contribute greatly to the specific differential phase, whereas the larger, more oblate that a raindrop is, the greater the relative phase shift it induces.

4.4.4 Co-polar Correlation Coefficient

Recall from Section 2.4.5 that the CC is the magnitude of the statistical correlation coefficient between the received horizontally and vertically polarized signals. Given a DSD, $N(D_e; X)$, and axis ratio PDF, $p_{r|D_e}(r|D_e)$, the expected value of the CC is

$$\rho = \frac{\text{num}(\rho)}{\sqrt{\eta_h \eta_v}}, \tag{101}$$

where the numerator of ρ, denoted as $\text{num}(\rho)$, is

$$\text{num}(\rho) = 4\pi \int_0^\infty \int_0^\infty S_{hh}(r, D_e, \pi)\, S_{vv}(r, D_e, \pi)\, N(D_e; X)\, p_{r|D_e}(r|D_e)\ dr\ dD_e. \tag{102}$$

The CC is generally not considered very useful for DSD estimation since it maintains a value close to unity for the realistic range of DSDs. However, it is considered here for completeness.

4.5 Proposed Mathematical Formulation

While Section 4.4 mapped DSD parameters to the radar measurements, the relationships are not closed-form expressions that are easily manipulated. This section seeks closed-form expressions relating the DSD parameters and rain rate to the expected value of the radar measurements.

First, we seek a closed-form expression for the unit volume RCS (in both polarization channels) since per unit volume RCS is proportional to reflectivity. Equation (99) for computing η_h and η_v may be rewritten as

$$\eta_\bullet = \frac{1}{\lambda^4} \int_0^\infty N(D_e; X) \left[\int_0^\infty \frac{\pi^5}{9} D_e^6 \alpha_\bullet^2(r)\, p_{r|D_e}(r|D_e)\, dr \right] dD_e, \tag{103}$$

where $\bullet$ is either h or v for horizontal and vertical polarizations, respectively. In (103) and throughout the remainder of this paper, $a_\bullet$, $b_\bullet$, and $c_\bullet$ with various subscripts represent fitting parameters. Due to the functional form of the inner integral in (103), which is a function of D_e, it must be integrated numerically. For mathematical

convenience, we propose the following approximation for the integral over r in (103):

$$\int_0^\infty \frac{\pi^5}{9} D_e^6 \alpha_\bullet^2 (r)\, p_{r|D_e}(r|D_e)\, dr \approx a_\bullet D_e^{b_\bullet} e^{-c_\bullet D_e}, \tag{104}$$

where, again, $\bullet$ is either h or v for horizontal and vertical polarizations, respectively. By substituting (2) for $N(D_e; X)$ and substituting the approximation in (104) for the integral over r in (103), reflectivity can be approximated with the following closed-form function of the DSD parameters:

$$\begin{aligned} \eta_\bullet &= \frac{a_\bullet N_o}{\lambda^4} \int_0^\infty D_e^{\mu+b_\bullet} e^{-(\Lambda+c_\bullet)D_e} dD_e \\ &= \frac{a_\bullet N_o}{\lambda^4 (\Lambda + c_\bullet)^{b_\bullet+\mu+1}} \Gamma(b_\bullet + \mu + 1). \end{aligned} \tag{105}$$

A similar analysis can be performed for the specific differential phase:

$$\begin{aligned} K_{DP} &= \frac{1}{\lambda} \int_0^\infty N(D_e; X) \left[\int_0^\infty \frac{\pi^2}{6} D^3 (\alpha_h(r) - \alpha_v(r))\, p_{r|D_e}(r|D_e)\, dr \right] dD_e \\ &= \frac{a_k N_o}{\lambda (\Lambda + c_k)^{\mu+b_k+1}} \Gamma(\mu + b_k + 1), \end{aligned} \tag{106}$$

where the following approximation has been made:

$$\int_0^\infty \frac{\pi^2}{6} D^3 (\alpha_h(r) - \alpha_v(r))\, p_{r|D_e}(r|D_e)\, dr \approx a_k D_e^{b_k} e^{-c_k D_e}, \tag{107}$$

where a_k, b_k, and c_k are the fitting parameters. Next, we consider the numerator of the CC:

$$\text{num}(\rho) = \frac{1}{\lambda^4} \int_0^\infty N(D_e; X) \left[\int_0^\infty \frac{\pi^5}{9} D_e^6 \alpha_h \alpha_v (r)(r)\, p_{r|D_e}(r|D_e)\, dr \right] dD_e, \tag{108}$$

and approximate the integral over r as

$$\int_0^\infty \frac{\pi^5}{9} D_e^6 \alpha_h \alpha_v (r)\, p_{r|D_e}(r|D_e)\, dr \approx a_\rho D_e^{b_\rho} e^{-c_\rho D_e}, \tag{109}$$

where a_ρ, b_ρ, and c_ρ are fitting parameters. The denominator of the CC in (101) is the square root of the product of the horizontal and vertical RCS. Substituting (105) into

the denominator for the horizontal and vertical RCS and replacing the approximation of (109) into the numerator, the CC may be approximated as

$$\rho = \frac{a_\rho}{\sqrt{a_h a_v}} \frac{(\Lambda + c_h)^{\frac{\mu+b_h+1}{2}} (\Lambda + c_v)^{\frac{\mu+b_v+1}{2}}}{(\Lambda + c_\rho)^{\mu+b_\rho+1}} \frac{\Gamma(\mu + b_\rho + 1)}{\sqrt{\Gamma(\mu + b_h + 1)\Gamma(\mu + b_v + 1)}}. \quad (110)$$

In the next section, we seek a set of "optimal" coefficients (i.e., a_h, b_h, c_h, etc.) for which these approximations of the axis ratio integral[4] term (of each data product) are reasonable.

While the wavelength dependence of the data products is not included in the axis ratio integral term, the axis ratio-dependent part of the polarizability terms (i.e., $\alpha_h(r)$ and $\alpha_h(r)$), which are part of the axis ratio integral, are dependent on the dielectric constant of water, which depends on temperature and radar transmit frequency. However, a dielectric constant value of $\epsilon_r = 81$, which is used in this dissertation, is valid for the relevant range of transmit frequencies and water temperatures.

4.6 Coefficient Estimation

This section seeks to find the optimal set of coefficients (i.e., a_h, b_h, c_h, etc.) for the approximations proposed in the previous section:

$$u_\bullet \approx a_\bullet D_e^{b_\bullet} e^{-c_\bullet D_e}, \quad (111)$$

where $a_\bullet$, $b_\bullet$, and $c_\bullet$ are the coefficients to be estimated; $\bullet$ is either h, v, k, or ρ, depending on the data product of interest, and $u_\bullet$ denotes the exact value of the integration over r that is obtained via numerical integration. Specifically, for the approaches described below, we seek an approximation that is "optimal" for values of $D_e \leq 6$ mm.

We consider to approaches for estimating these coefficients, both of which define optimal coefficients as those which minimize a cost function. These two approaches

[4]For the remainder of this chapter, the term "axis ratio integral" is used to refer to the "inner integral" over r for each of the four data products considered.

are nonlinear least-squares estimation (NLSE) and linearized least-squares estimation (LLSE). In the NLSE approach, the objective function to be minimized is

$$g_{nls}\left(a_\bullet, b_\bullet, c_\bullet\right) = \frac{1}{2}\sum_{i=1}^{N_u}\left[u_i - a_\bullet D_{e_i}^{b_\bullet} e^{-c_\bullet D_{e_i}}\right]^2 \tag{112}$$

where N_u is the number of discrete drop diameters for which the integral is evaluated, D_{e_i} is the the i^{th} drop diameter for which the integral is evaluated, and u_i is the corresponding integral value. In general, the NLSE approach does not have a closed solution and must be solved iteratively. The LLSE approach simplifies the problem by taking the natural logarithm of both sides of (111):

$$\begin{aligned}\ln\left(u_\bullet\right) &\approx \ln\left(a_\bullet D_e^{b_\bullet} e^{-c_\bullet D_e}\right) \\ &= \ln\left(a_\bullet\right) + b_\bullet \ln\left(D_e\right) - c_\bullet D_e\end{aligned} \tag{113}$$

so that the new objective function to be minimized is

$$g_{lls}\left(a_\bullet, b_\bullet, c_\bullet\right) = \frac{1}{2}\sum_{i=1}^{N_u}\left[\ln\left(u_i\right) - \left(\ln\left(a_\bullet\right) + b_\bullet \ln\left(D_{e_i}\right) - c_\bullet D_{e_i}\right)\right]^2. \tag{114}$$

This is a linear least-squares estimation problem. This solution, however, is generally considered suboptimal since applying the linearization transformation alters the influence of the data on the regression results.

For each combination of mean axis ratio models and axis ratio variance models, the coefficients resulting from these procedures are given in Appendix A in Tables 12 - 15, along with the coefficient of determination (CD) as a measure of the goodness of fit. The CD is defined as:

$$CD = 1 - \frac{\sum_{i=1}^{N_u}\left(u_i - f_{u_i}\right)^2}{\sum_{i=1}^{N_u}\left(u_i - \overline{u}\right)^2}, \tag{115}$$

where f_{u_i} denotes the value of the resulting approximation for u_i and

$$\overline{u} = \frac{1}{N_u}\sum_{i=1}^{N_u} u_i. \tag{116}$$

A CD of one implies that the approximation is perfect and results in no error. For each data product and possible combination of mean and standard deviation models,

the CD is between 0.99 and 1. The one exception is the LLSE fit for the axis ratio integral term of K_{DP}; however, the NLSE fit for the axis ratio integral term of K_{DP} is still between 0.99 and 1.

4.7 Results

The CDs in Appendix A provide a measure of the quality of fit of the proposed approximation to the axis ratio integral term given the coefficients estimated in Section 4.6. This section applies the computed coefficients to the approximations proposed in Section 4.5 (i.e., (105), (106), and (110)) for a uniform sampling over the following ranges of realistic (transformed) DSD parameters [15]:

$$\begin{aligned} &3 \leq \log_{10}(N_w) \leq 5 \quad \log_{10}\left(\frac{\text{mm}^{-1}}{\text{m}^3}\right) \\ &0.5 \leq D_o \leq 2.5 \ \text{ mm} \\ &-1 \leq \mu \leq 5, \end{aligned} \tag{117}$$

where

$$N_w = N_o \frac{3.67^4}{6} \frac{\Gamma(\mu+4)}{(3.67+\mu)^4} \Lambda^{-\mu} \tag{118}$$

and

$$D_o = \frac{3.67+\mu}{\Lambda}. \tag{119}$$

These results are compared to the exact numerical integration of (99), (100), and (101) to determine the quality of fit of the approximations to the data products themselves. The resulting CDs for each of the four data products (horizontal reflectivity, vertical reflectivity, specific differential phase, and the CC) are given in Tables 2 and 3. Additionally, using the developed approximations for horizontal and vertical reflectivity, the resulting approximation for differential reflectivity is computed and compared to the exact numerical calculations. Those results are also given in Tables

Table 2: Coefficients of determination for approximation of data products using LLSE coefficients

MM	SDM	ζ_h	Z_H	ζ_v	Z_V	ζ_{dr}	Z_{DR}	K_{DP}	ρ
A	Z	1.00	1.00	1.00	1.00	0.99	0.99	1.00	0.98
A	P	1.00	1.00	1.00	1.00	0.99	0.99	0.98	0.98
A	J	0.99	1.00	1.00	1.00	0.95	0.97	0.98	0.56
B&C	Z	1.00	1.00	1.00	1.00	1.00	1.00	1.00	0.99
B&C	P	1.00	1.00	1.00	1.00	1.00	1.00	0.98	0.99
B&C	J	0.99	1.00	1.00	1.00	0.95	0.97	0.98	0.54
B	Z	1.00	1.00	1.00	1.00	0.98	0.99	0.98	0.79
B	P	1.00	1.00	1.00	1.00	0.98	0.99	0.98	0.79
B	J	0.91	1.00	1.00	1.00	0.77	0.90	0.98	0.35

Table 3: Coefficients of determination for approximation of data products using NLSE coefficients

MM	SDM	ζ_h	Z_H	ζ_v	Z_V	ζ_{dr}	Z_{DR}	K_{DP}	ρ
A	Z	1.00	1.00	1.00	1.00	0.01	-1.72	1.00	-0.40
A	P	1.00	1.00	1.00	1.00	0.01	-1.72	1.00	-0.46
A	J	1.00	1.00	1.00	0.99	0.97	0.98	1.00	-22.51
B&C	Z	1.00	1.00	1.00	1.00	0.88	0.77	1.00	0.56
B&C	P	1.00	1.00	1.00	1.00	0.88	0.77	1.00	0.55
B&C	J	1.00	0.99	1.00	1.00	0.45	0.20	1.00	-21.92
B	Z	1.00	1.00	1.00	1.00	0.88	0.79	1.00	0.81
B	P	1.00	1.00	1.00	1.00	0.88	0.79	1.00	0.81
B	J	0.98	0.96	1.00	1.00	-6.43	-4.60	1.00	-21.38

2 and 3 as well. For horizontal, vertical, and differential reflectivity, the CD is evaluated for both linear reflectivities (i.e., ζ_h, ζ_v, and ζ_{dr}) and reflectivies on a decibel (or dBz) scale, i.e., Z_H, Z_V, and Z_{DR}, respectively.

For further visualization of results, refer to Appendix B. For the range of DSD parameters specified in (117), the value of the resulting approximation for each of the data products is plotted versus the exact value that is obtained via numerical integration.

4.8 Conclusions

For horizontal and vertical reflectivity, the coefficients that are estimated using the LLSE approach provide the best approximations over the range of realistic DSD parameters. Not only do they well approximate horizontal and vertical reflectivity, but they also provide a good approximation for differential reflectivity for the majority of the mean axis ratio and axis ratio variance models. Upon initial consideration, it may be surprising that the LLSE coefficient estimates provided a better overall approximation than the NLSE coefficient estimates. We hypothesize that this is because realistic DSDs are dominated by raindrops that are "small." Specifically, consider the drop diameter value corresponding to N_σ standard deviations beyond the mean of the DSD, i.e.,

$$E\left[D_e\right] + N_\sigma \sigma_{D_e}. \tag{120}$$

For the range of DSD parameters given in (117), the maximum value of (120) is not greater than 2.44, 3.14, and 3.85 mm for N_σ equal to one, two, and three, respectively. As previously mentioned, the linearization process alters the influence of the data on the regression results. Specifically, the linearization imposes a bias towards better fitting the axis ratio integral term at smaller drop diameters. This improves the overall approximation for the data products, but only for the range of DSDs considered. If these approximations were applied to a DSD with a much larger mean or standard deviation, this statement would likely no longer be accurate.

For specific differential phase, the coefficients estimated using the NLSE approach provide the best approximations over the range of realistic DSD parameters. We hypothesize that this is because, on average, small raindrops are modeled as spherical. Perfectly spherical drops do not induce a specific differential phase on an EM wave, i.e., $K_{DP} = 0$. As a result, small raindrops do not contribute significantly to the total specific differential phase. Thus, the bias towards better fitting the axis ratio integral term for smaller drop diameters, which occurs in the LLSE approach, is undesirable.

For the CC, the coefficients estimated using the LLSE approach provide the best approximations over the range of realistic DSD parameters. However, only the first two mean axis ratio models in combination with the first two axis ratio variance models provide a good fit. For rain, the CC varies very little and usually maintains a value close to unity. This small variation means that the CD will drop drastically for even small errors in the CC approximation. Nonetheless, these errors are significant relative to the variation of the CC over the realistic range of DSDs.

4.9 Summary

This chapter presented a closed-form mathematical formulation to suitably approximate the data products provided by a dual-pol radar as a function of the DSD parameters of rain. Further, this chapter estimated coefficients for various models of the PDF of the axis ratio of a raindrop. Overall, the presented formulations well approximate the data products. More specifically, the coefficients estimated using the LLSE approach provide a good approximation for horizontal reflectivity, vertical reflectivity, and the CC, while the NLSE coefficients yield better approximations for specific differential phase. The one exception is the approximation of the CC for some of the axis ratio PDF models considered. Thus, throughout this dissertation, the estimated LLSE coefficients are used to approximate horizontal reflectivity, vertical reflectivity, and the CC, whereas the NLSE coefficients are used to approximate the specific differential phase.

CHAPTER V

VARIANCE BOUNDS FOR ESTIMATION OF DROP SIZE DISTRIBUTION PARAMETERS

5.1 Overview

While multiple approaches have been suggested for DSD estimation, and studies have been performed to evaluate these estimators, no fundamental limit has yet been established for how well these estimators could perform given the available dual-pol data. The objective of this chapter is to derive fundamental bounds for the variance of any unbiased estimator of the DSD parameters given the standard dual-pol data products recorded by operational weather radars.

This chapter is organized as follows. Section 5.2 begins by discussing the dual-pol signal model. Based on this model, Section 5.3 derives the CRLB of the DSD parameters. Then, Section 5.4 proposes a method for computing the MLE of the DSD parameters so that the existence of an efficient estimator, which achieves the CRLB, can be tested. Subsequently, Section 5.5 tests for the existence of an efficient estimator by computing and comparing the CRLB to the variance of the MLE for a typical value of the DSD parameters.

5.2 Signal Model

5.2.1 Model for a Single Resolution Volume

Consider a dual-pol weather radar that simultaneously transmits and receives horizontally and vertically linearly polarized waves. In a given dwell, N_p pulses are transmitted and received. For a single resolution volume, the received dual-pol data sample from the i^{th} pulse is denoted as $x_i = [x_{h_i}\ x_{v_i}]^T$, where x_h and x_v are the

radar returns in the horizontal and vertical channels, respectively. The received dual-pol signal from an ensemble of elementary scatterers (e.g., raindrops) with random interference fading (i.e., Rayleigh fading) is modeled with a multivariate zero-mean, circular, complex Gaussian distribution [27, 76, 85]. Assuming pulses are independent and identically distributed (i.i.d.), the joint PDF of the pulse returns is

$$\begin{aligned} p_x\left(x_1, ..., x_{N_p}\right) &= \prod_{i=1}^{N_p} p_{x_i}\left(x_i\right) \\ &= \frac{1}{\pi^{2N_p}\left|\det\left(C_x\right)\right|^{N_p}} e^{-\mathrm{tr}\left(C_x^{-1}\sum_{i=1}^{N_p} x_i x_i^H\right)}, \end{aligned} \tag{121}$$

where C_x is the covariance matrix of the distribution and $\mathrm{tr}\left(\bullet\right)$ denotes the trace operator. The effects of noise are not considered in this model; it assumes that the SNR is sufficiently high that noise may be neglected. This assumption is valid in the majority of relevant applications and is generally considered a necessity to extract any reliable information from the dual-pol data products [76].

While this model assumes independent samples, rain scatter only partially decorrelates from pulse to pulse at the PRF of most weather radars, including the WSR-88D (as discussed in Section 2.2.6). However, at a slow enough PRF, the pulses can be treated as independent. Additionally, if the autcorrelation function of the pulse sequence is known and no two pulses are perfectly correlated, a whitening filter can be applied to the data, resulting in N_p i.i.d. samples [76].

The terms in the covariance matrix,

$$C_x = \begin{bmatrix} C_{hh} & C_{hv} \\ C_{vh} & C_{vv} \end{bmatrix}, \tag{122}$$

fully characterize the PDF in (121). The sample covariance matrix,

$$\begin{aligned}\hat{C}_x &= \frac{1}{N_p}\sum_{i=1}^{N_p} x_i x_i^H \\ &= \frac{1}{N_p}\begin{bmatrix} \sum_{i=1}^{N_p} x_{h_i}x_{h_i}^* & \sum_{i=1}^{N_p} x_{h_i}x_{v_i}^* \\ \sum_{i=1}^{N_p} x_{v_i}x_{h_i}^* & \sum_{i=1}^{N_p} x_{v_i}x_{v_i}^* \end{bmatrix} \\ &= \frac{1}{N_p}\begin{bmatrix} \hat{C}_{hh} & \hat{C}_{hv} \\ \hat{C}_{hv}^* & \hat{C}_{vv} \end{bmatrix}\end{aligned} \tag{123}$$

is a sufficient statistic (and an efficient estimator [27, 76]) for the matrix C_x.

The matrix C_x can be rewritten as

$$C_x = \begin{bmatrix} P_h & \sqrt{P_h P_v}\rho e^{j\phi} \\ \sqrt{P_h P_v}\rho e^{-j\phi} & P_v \end{bmatrix}, \tag{124}$$

where P_h and P_v denote the received power in the horizontal and vertical channels, respectively. Recalling that reflectivity is proportional to power, it is evident that the four radar data products are a set of sufficient statistics for describing the joint PDF of the received dual-pol data sequence in an individual resolution volume.

5.2.2 Model for Multiple Resolution Volumes

Recall that in applications such as DSD and rain rate estimation, the instantaneous differential phase is not very useful, as it does not have a direct mapping to rain rate or the DSD parameters. Rather, an estimate of the specific differential phase is required. It is estimated as [42]

$$\hat{K}_{DP} = \frac{\hat{\phi}_a - \hat{\phi}_b}{2\Delta_R}, \tag{125}$$

where $\hat{\phi}_a$ and $\hat{\phi}_b$ denote the estimated instantaneous differential phase of resolution volumes at ranges R_a and R_b, respectively, and $\Delta_R = R_a - R_b$. The model in this paper assumes that the estimate of K_{DP} is derived from two resolution volumes with the same DSD (i.e., the same scattering properties) such that the signals received

for each of these range resolution cells are i.i.d., with the exception that they have different instantaneous differential phases with the following relation:

$$\phi_a - \phi_b = 2\Delta_R K_{DP}. \tag{126}$$

5.2.3 Mapping DSD Parameters to Radar Measurements

The received power estimates, which are proportional to reflectivity, can be related to the per unit volume RCS using the weather RRE [82]:

$$\begin{aligned} \eta_h &= \left[\frac{(1024 \ln 2)\, \pi^2 R^2 L^2 (R)}{P_t G^2 \lambda^2 \theta_3^2 c\tau}\right] P_h \\ &= C_{rre} P_h. \end{aligned} \tag{127}$$

The term C_{rre} is introduced as a convenient shorthand notation for the bracketed term in (127). The above RRE holds for vertical polarization as well, i.e., $\eta_v = C_{rre} P_v$.

There exists a mapping between the parameters of the DSD, $X = [N_o\ \mu\ \Lambda]^T$, and the observed values of η_h, η_v, K_{DP}, and ρ. Closed-form expressions that approximate these mappings for Rayleigh scattering were derived in Chapter 4 [67] as

$$\eta_h = \frac{a_h N_o}{\lambda^4 (\Lambda + c_h)^{b_h+\mu+1}} \Gamma (b_h + \mu + 1), \tag{128}$$

$$\eta_v = \frac{a_v N_o}{\lambda^4 (\Lambda + c_v)^{b_v+\mu+1}} \Gamma (b_v + \mu + 1), \tag{129}$$

$$K_{DP} = \frac{a_k N_o}{\lambda (\Lambda + c_k)^{b_k+\mu+1}} \Gamma (b_k + \mu + 1), \tag{130}$$

and

$$\rho = \frac{a_\rho}{\sqrt{a_h a_v}} \frac{(\Lambda + c_h)^{\frac{\mu+b_h+1}{2}} (\Lambda + c_v)^{\frac{\mu+b_v+1}{2}}}{(\Lambda + c_\rho)^{\mu+b_\rho+1}} \frac{\Gamma (\mu + b_\rho + 1)}{\sqrt{\Gamma (\mu + b_h + 1)\, \Gamma (\mu + b_v + 1)}}, \tag{131}$$

where the coefficients, a_h, b_h, c_h, a_v, b_v, c_v, a_k, b_k, c_k, a_ρ, b_ρ, and c_ρ, given in Appendix A, depend on the particular model used to describe the distribution of raindrop axis ratios.

5.3 Cramér-Rao Lower Bound of DSD Parameters

The CRLB states [45]:

$$\operatorname{cov}\left(\hat{X}\right) \geq J_F^{-1}(X), \tag{132}$$

where $\hat{X}$ denotes an unbiased estimator of X, $\operatorname{cov}\left(\hat{X}\right)$ denotes the covariance matrix of $\hat{X}$, $J_F(X)$ is the Fisher information matrix (FIM), and the $(i,j)^{th}$ element of the FIM is

$$\left[J_F(X)\right]_{ij} = -E_Y\left[\frac{\partial^2 \ln p_Y(Y;X)}{\partial X_i \partial X_j}\right], \tag{133}$$

where Y denotes the observed data. The inequality in (132) means that the matrix

$$\operatorname{cov}\left(\hat{X}\right) - J_F^{-1}(X) \tag{134}$$

is positive semi-definite; i.e., all its eigenvalues are non-negative, which means that the diagonal terms of the inverse FIM bound the variance of the unbiased estimator, $\hat{X}$, i.e.,

$$E\left[\left(\hat{X}_i - X_i\right)^2\right] \geq \left[J_F^{-1}(X)\right]_{ii}. \tag{135}$$

To derive the CRLB of the DSD parameters, we begin with the inverse FIM of

$$\beta_1 = \begin{bmatrix} C_{hh} \\ C_{vv} \\ |C_{hv}| \\ \arg(C_{hv}) \end{bmatrix}, \tag{136}$$

which is given in [76] as

$$J_F^{-1}(\beta_1) =$$
$$\frac{1}{N_p}\begin{bmatrix} C_{hh}^2 & |C_{hv}| & |C_{hv}|\,C_{hh} & 0 \\ |C_{hv}| & C_{vv}^2 & |C_{hv}|\,C_{vv} & 0 \\ |C_{hv}|\,C_{hh} & |C_{hv}|\,C_{vv} & \frac{1}{2}\left(C_{hh}C_{vv}+|C_{hv}|^2\right) & 0 \\ 0 & 0 & 0 & \frac{1}{2}|C_{hv}|^{-2}\left(C_{hh}C_{vv}-|C_{hv}|^2\right) \end{bmatrix}. \tag{137}$$

From here, we use the transformation property of the CRLB [45]:

$$J_F^{-1}(\beta) = \frac{\partial\beta}{\partial\alpha} J_F^{-1}(\alpha) \frac{\partial\beta}{\partial\alpha}^H, \tag{138}$$

where $\frac{\partial\beta}{\partial\alpha}$ denotes the Jacobian of the transformation $\beta = f_\beta(\alpha)$. By sequentially applying this property based on a series of variable transformations, we arrive at the CRLB of the DSD parameters, X.

5.3.1 CRLB of P_h, P_v, ρ, and ϕ

We start by seeking the CRLB of

$$\beta_2 = \begin{bmatrix} P_h \\ P_v \\ \rho \\ \phi \end{bmatrix} = \begin{bmatrix} C_{hh} \\ C_{vv} \\ |C_{hv}| C_{hh}^{-\frac{1}{2}} C_{vv}^{-\frac{1}{2}} \\ \arg(C_{hv}) \end{bmatrix}. \tag{139}$$

The Jacobian of the transformation from β_1 to β_2 is

$$\frac{\partial\beta_2}{\partial\beta_1} = \begin{bmatrix} 1 & 0 & 0 & 0 \\ 0 & 1 & 0 & 0 \\ -\frac{1}{2}|C_{hv}| C_{hh}^{-\frac{3}{2}} C_{vv}^{-\frac{1}{2}} & -\frac{1}{2}|C_{hv}| C_{hh}^{-\frac{1}{2}} C_{vv}^{-\frac{3}{2}} & C_{hh}^{-\frac{1}{2}} C_{vv}^{-\frac{1}{2}} & 0 \\ 0 & 0 & 0 & 1 \end{bmatrix}. \tag{140}$$

Substituting (137) and (140) into (138) and simplifying yields

$$J_F^{-1}(\beta_2) = \frac{\partial \beta_2}{\partial \beta_1} J_F^{-1}(\beta_1) \frac{\partial \beta_2}{\partial \beta_1}^H$$
$$= \frac{1}{N_p} \begin{bmatrix} P_h^2 & \rho^2 P_h P_v & \frac{1}{2}\rho P_h (1-\rho^2) & 0 \\ \rho^2 P_h P_v & P_v^2 & \frac{1}{2}\rho P_v (1-\rho^2) & 0 \\ \frac{1}{2}\rho P_h (1-\rho^2) & \frac{1}{2}\rho P_v (1-\rho^2) & \frac{1}{2}(1-\rho^2)^2 & 0 \\ 0 & 0 & 0 & \frac{1}{2}\rho^{-2}(1-\rho^{-2}) \end{bmatrix}, \tag{141}$$

which is the CRLB of β_2.

5.3.2 CRLB of P_h, P_v, ρ, and Δ_ϕ

Next, we find the CRLB of

$$\beta_3 = \begin{bmatrix} P_h \\ P_v \\ \rho \\ \Delta_\phi \end{bmatrix} = \begin{bmatrix} P_h \\ P_v \\ \rho \\ \phi_a - \phi_b \end{bmatrix}. \tag{142}$$

The calculation of β_3 requires data from two resolution volumes. As mentioned in Section 5.2, we presume that such estimates are formed from two resolution volumes with identical DSDs. As a result, the data received from the two resolution volumes are i.i.d., except they have different instantaneous differential phases. Thus, we define the vector

$$\beta_{2_{ab}} = \begin{bmatrix} \beta_{2_a} \\ \beta_{2_b} \end{bmatrix} \tag{143}$$

to be the concatenated set of parameters, β_{2_a}, which represents β_2 for range bin R_a, and β_{2_b}, which represents β_2 for range bin R_b. Based on these modeling assumptions, the CRLB of $\beta_{2_{ab}}$ is

$$J_F^{-1}(\beta_{2_{ab}}) = \begin{bmatrix} J_F^{-1}(\beta_{2_a}) & \mathbf{0} \\ \mathbf{0} & J_F^{-1}(\beta_{2_b}) \end{bmatrix}, \tag{144}$$

where $J_F^{-1}(\beta_{2_a}) = J_F^{-1}(\beta_{2_b}) = J_F^{-1}(\beta_2)$ and $\mathbf{0}$ denotes a zero matrix of appropriate size. The Jacobian of the transformation from $\beta_{2_{ab}}$ to β_3 is

$$\frac{\partial \beta_3}{\partial \beta_{2_{ab}}} = \begin{bmatrix} I_4 & M_{-1} \end{bmatrix}, \tag{145}$$

where I_4 is a 4×4 identity matrix and M_{-1} is a 4×4 matrix with all entries equal to 0 except the the lower right entry, which is equal to -1. This yields

$$\begin{aligned} J_F^{-1}(\beta_3) &= \frac{\partial \beta_3}{\partial \beta_{2_{ab}}} J_F^{-1}(\beta_{2_{ab}}) \frac{\partial \beta_3}{\partial \beta_{2_{ab}}}^H \\ &= \frac{1}{N_p} \begin{bmatrix} P_h^2 & \rho^2 P_h P_v & \frac{1}{2}\rho P_h (1-\rho^2) & 0 \\ \rho^2 P_h P_v & P_v^2 & \frac{1}{2}\rho P_v (1-\rho^2) & 0 \\ \frac{1}{2}\rho P_h (1-\rho^2) & \frac{1}{2}\rho P_v (1-\rho^2) & \frac{1}{2}(1-\rho^2)^2 & 0 \\ 0 & 0 & 0 & \rho^{-2}(1-\rho^{-2}) \end{bmatrix}, \end{aligned} \tag{146}$$

which is the CRLB of β_3.

5.3.3 CRLB of η_h, η_v, ρ, and K_{DP}

This sections seeks the CRLB of

$$\beta_4 = \begin{bmatrix} \eta_h \\ \eta_v \\ \rho \\ K_{DP} \end{bmatrix} = \begin{bmatrix} C_{rre} P_h \\ C_{rre} P_v \\ \rho \\ \frac{1}{2\Delta_R} \Delta_\phi \end{bmatrix}. \tag{147}$$

The Jacobian of the transformation from β_3 to β_4 is

$$\frac{\partial \beta_4}{\partial \beta_3} = \begin{bmatrix} C_{rre} & 0 & 0 & 0 \\ 0 & C_{rre} & 0 & 0 \\ 0 & 0 & 1 & 0 \\ 0 & 0 & 0 & \frac{1}{2\Delta_R} \end{bmatrix}. \tag{148}$$

Simple substitution yields

$$J_F^{-1}(\beta_4) = \frac{\partial \beta_4}{\partial \beta_3} J_F^{-1}(\beta_3) \frac{\partial \beta_4}{\partial \beta_3}^H$$
$$= \frac{1}{N_p} \begin{bmatrix} \eta_h^2 & \rho^2 \eta_h \eta_v & \frac{1}{2}\rho\eta_h(1-\rho^2) & 0 \\ \rho^2\eta_h\eta_v & \eta_v^2 & \frac{1}{2}\rho\eta_v(1-\rho^2) & 0 \\ \frac{1}{2}\rho\eta_h(1-\rho^2) & \frac{1}{2}\rho\eta_v(1-\rho^2) & \frac{1}{2}(1-\rho^2)^2 & 0 \\ 0 & 0 & 0 & \frac{1}{4\Delta_R^2}\rho^{-2}(1-\rho^{-2}) \end{bmatrix}, \tag{149}$$

which is the CRLB of β_4.

5.3.4 CRLB of N_o, μ, and Λ

This section computes the CRLB of the DSD parameters, $X = [N_o\ \mu\ \Lambda]^T$, from the radar measurements, i.e., β_4. As in the previous sections, the intent is to compute the CRLB using the transformation property of the inverse FIM. However, the calculation of the Jacobian $\frac{\partial X}{\partial \beta_4}$ is precluded by the fact that an explicit expression for the forward transformation from β_4 to X is not known. The reverse transformation from X to β_4 is provided in (128) - (131) in Section 5.2. This permits the calculation of $\frac{\partial \beta_4}{\partial X}$.[1] To compute the CRLB of X given β_4, we would need to solve the following equation for $J_F^{-1}(X)$:

$$J_F^{-1}(\beta_4) = \frac{\partial \beta_4}{\partial X} J_F^{-1}(X) \frac{\partial \beta_4}{\partial X}^H, \tag{150}$$

but this is an overdetermined equation with no solution. However, since ρ fluctuates very little in rain for a wide range of DSDs, it is not used in practice for estimating the DSD or rain rate. Thus, we consider the subset of measurements $Y = [\eta_h\ \eta_v\ K_{DP}]^T$ instead, discarding ρ and seeking the solution to the alternate problem:

$$J_F^{-1}(Y) = \frac{\partial Y}{\partial X} J_F^{-1}(X) \frac{\partial Y}{\partial X}^H, \tag{151}$$

[1] Since the dimensions of X and β_4 are not equal, $\frac{\partial X}{\partial \beta_4}$ is not square, and, as a result, $\frac{\partial X}{\partial \beta_4}$ cannot be computed as the inverse of $\frac{\partial \beta_4}{\partial X}$.

for $J_F^{-1}(X)$. From (149) in Section 5.3.3, it is evident that

$$J_F^{-1}(Y) = \frac{1}{N_p}\begin{bmatrix} \eta_h^2 & \rho^2\eta_h\eta_v & 0 \\ \rho^2\eta_h\eta_v & \eta_v^2 & 0 \\ 0 & 0 & \frac{1}{4\Delta_R^2}\rho^{-2}\left(1-\rho^{-2}\right) \end{bmatrix}. \tag{152}$$

Now, we must determine the Jacobian $\frac{\partial Y}{\partial X}$ and solve for $J_F^{-1}(X)$.

5.3.4.1 Jacobian of DSD Transformation

The Jacobian $\frac{\partial Y}{\partial X}$ is

$$\frac{\partial Y}{\partial X} = \begin{bmatrix} \frac{\partial \eta_h}{\partial N_o} & \frac{\partial \eta_h}{\partial \mu} & \frac{\partial \eta_h}{\partial \Lambda} \\ \frac{\partial \eta_v}{\partial N_o} & \frac{\partial \eta_v}{\partial \mu} & \frac{\partial \eta_v}{\partial \Lambda} \\ \frac{\partial K_{DP}}{\partial N_o} & \frac{\partial K_{DP}}{\partial \mu} & \frac{\partial K_{DP}}{\partial \Lambda} \end{bmatrix}. \tag{153}$$

Each term in $\frac{\partial Y}{\partial X}$ is computed using the relations in (128) - (130). Starting with (128), the equation for horizontal reflectivity, we find

$$\begin{aligned} \frac{\partial \eta_h}{\partial N_o} &= \frac{a_h}{\lambda^4(\Lambda+c_h)^{\mu+b_h+1}}\Gamma(\mu+b_h+1) \\ &= \frac{1}{N_o}\eta_h \\ &= \delta_n\eta_h, \end{aligned} \tag{154}$$

$$\begin{aligned} \frac{\partial \eta_h}{\partial \mu} &= \frac{N_o a_h}{\lambda^4(\Lambda+c_h)^{\mu+b_h+1}}\Gamma(\mu+b_h+1)\left[\Psi_0(\mu+b_h+1)-\ln(\Lambda+c_h)\right] \\ &= \left[\Psi_0(\mu+b_h+1)-\ln(\Lambda+c_h)\right]\eta_h \\ &= \delta_{h\mu}\eta_h, \end{aligned} \tag{155}$$

and

$$\begin{aligned} \frac{\partial \eta_h}{\partial \Lambda} &= -\frac{N_o a_h}{\lambda^4(\Lambda+c_h)^{\mu+b_h+1}}\Gamma(\mu+b_h+1)\frac{\mu+b_h+1}{\Lambda+c_h} \\ &= -\frac{\mu+b_h+1}{\Lambda+c_h}\eta_h \\ &= \delta_{hl}\eta_h, \end{aligned} \tag{156}$$

where Ψ_0 is the zero-order polygamma function and the terms δ_n, $\delta_{h\mu}$, and δ_{hl}, given in Table 4, are introduced as a convenient shorthand notation. The equation for

vertical reflectivity is analogous to that for horizontal reflectivity; hence, so are its partial derivatives:

$$\begin{aligned}\frac{\partial \eta_v}{\partial N_o} &= \frac{a_v}{\lambda^4 (\Lambda + c_v)^{\mu + b_v + 1}} \Gamma (\mu + b_v + 1) \\ &= \frac{1}{N_o} \eta_v \\ &= \delta_n \eta_v,\end{aligned} \tag{157}$$

$$\begin{aligned}\frac{\partial \eta_v}{\partial \mu} &= \frac{N_o a_v}{\lambda^4 (\Lambda + c_v)^{\mu + b_v + 1}} \Gamma (\mu + b_v + 1) \left[\Psi_0 (\mu + b_v + 1) - \ln (\Lambda + c_v)\right] \\ &= \left[\Psi_0 (\mu + b_v + 1) - \ln (\Lambda + c_v)\right] \eta_v \\ &= \delta_{v\mu} \eta_v,\end{aligned} \tag{158}$$

and

$$\begin{aligned}\frac{\partial \eta_v}{\partial \Lambda} &= -\frac{N_o a_v}{\lambda^4 (\Lambda + c_v)^{\mu + b_v + 1}} \Gamma (\mu + b_v + 1) \frac{\mu + b_v + 1}{\Lambda + c_v} \\ &= -\frac{\mu + b_v + 1}{\Lambda + c_v} \eta_v \\ &= \delta_{vl} \eta_v.\end{aligned} \tag{159}$$

Similarly, the partial derivatives of K_{DP} are

$$\begin{aligned}\frac{\partial K_{DP}}{\partial N_o} &= \frac{a_k}{\lambda (\Lambda + c_k)^{\mu + b_k + 1}} \Gamma (\mu + b_k + 1) \\ &= \frac{1}{N_o} K_{DP} \\ &= \delta_n K_{DP},\end{aligned} \tag{160}$$

$$\begin{aligned}\frac{\partial K_{DP}}{\partial \mu} &= \frac{N_o a_k}{\lambda (\Lambda + c_k)^{\mu + b_k + 1}} \Gamma (\mu + b_k + 1) \left[\Psi_0 (\mu + b_k + 1) - \ln (\Lambda + c_k)\right] \\ &= \left[\Psi_0 (\mu + b_k + 1) - \ln (\Lambda + c_k)\right] K_{DP} \\ &= \delta_{k\mu} K_{DP},\end{aligned} \tag{161}$$

and

$$\begin{aligned}\frac{\partial K_{DP}}{\partial \Lambda} &= -\frac{N_o a_k}{\lambda (\Lambda + c_k)^{\mu + b_k + 1}} \Gamma (\mu + b_k + 1) \frac{\mu + b_k + 1}{\Lambda + c_k} \\ &= -\frac{\mu + b_k + 1}{\Lambda + c_k} K_{DP} \\ &= \delta_{kl} K_{DP}.\end{aligned} \tag{162}$$

Table 4: Terms in $\boldsymbol{\delta}$ Matrix

Term	Value
δ_n	$\frac{1}{N_p}$
δ_{hl}	$-\frac{\mu+b_h+1}{\Lambda+c_h}$
δ_{vl}	$-\frac{\mu+b_v+1}{\Lambda+c_v}$
δ_{kl}	$-\frac{\mu+b_k+1}{\Lambda+c_k}$
$\delta_{h\mu}$	$\Psi_0(\mu+b_h+1)-\ln(\Lambda+c_h)$
$\delta_{v\mu}$	$\Psi_0(\mu+b_v+1)-\ln(\Lambda+c_v)$
$\delta_{k\mu}$	$\Psi_0(\mu+b_k+1)-\ln(\Lambda+c_k)$

With equations (153) - (162), we arrive at the Jacobian $\frac{\partial Y}{\partial X}$:

$$\begin{aligned}\frac{\partial Y}{\partial X} &= \begin{bmatrix} \delta_n\eta_h & \delta_{h\mu}\eta_h & \delta_{hl}\eta_h \\ \delta_n\eta_v & \delta_{v\mu}\eta_v & \delta_{vl}\eta_v \\ \delta_n K_{DP} & \delta_{k\mu}K_{DP} & \delta_{kl}K_{DP} \end{bmatrix} \\ &= \begin{bmatrix} \eta_h & 0 & 0 \\ 0 & \eta_v & 0 \\ 0 & 0 & K_{DP} \end{bmatrix} \begin{bmatrix} \delta_n & \delta_{h\mu} & \delta_{hl} \\ \delta_n & \delta_{v\mu} & \delta_{vl} \\ \delta_n & \delta_{k\mu} & \delta_{kl} \end{bmatrix} \\ &= M_d\boldsymbol{\delta},\end{aligned} \tag{163}$$

where M_d and $\boldsymbol{\delta}$ are introduced for notational convenience and the entries in $\boldsymbol{\delta}$ are given in Table 4.

5.3.4.2 Computing the CRLB

To compute $J_F^{-1}(X)$, we substitute (163) into (151):

$$J_F^{-1}(Y) = M_d\boldsymbol{\delta}J_F^{-1}(X)\,\boldsymbol{\delta}^H M_d^H. \tag{164}$$

By moving M_d to the left side of the equation and noting that $M_d = M_d^H$, we have

$$M_d^{-1}J_F^{-1}(Y)\,M_d^{-1} = \boldsymbol{\delta}J_F^{-1}(X)\,\boldsymbol{\delta}^H. \tag{165}$$

The left side of (165) is then

$$M_d^{-1} J_F^{-1}(Y) M_d^{-1} = \frac{1}{N_p} \begin{bmatrix} 1 & \rho^2 & 0 \\ \rho^2 & 1 & 0 \\ 0 & & \frac{1}{4\Delta_R^2} \rho^{-2} (1-\rho^2) K_{DP}^{-2} \end{bmatrix}. \tag{166}$$

Therefore, the inverse FIM and CRLB of the DSD parameters is

$$J_F^{-1}(X) = \frac{1}{N_p} \boldsymbol{\delta}^{-1} \begin{bmatrix} 1 & \rho^2 & 0 \\ \rho^2 & 1 & 0 \\ 0 & & \frac{1}{4\Delta_R^2} \rho^{-2} (1-\rho^2) K_{DP}^{-2} \end{bmatrix} \left(\boldsymbol{\delta}^H\right)^{-1}, \tag{167}$$

where K_{DP} and ρ can be written in terms of the DSD parameters using (130) and (131), respectively.

5.4 Maximum Likelihood Estimate

The CRLB establishes a bound on the variance of any unbiased estimator, $\hat{X}$. An unbiased estimator that achieves the CRLB is the minimum-variance unbiased (MVUB) estimate of X and is referred to as an efficient estimator [45]. An efficient estimator is not guaranteed to exist, but if it does, it is the MLE, $\hat{X}_{mle}$ [45]. Recall from Chapter 3 that the MLE is the parameter value that maximizes the likelihood of the observed data [45], i.e.,

$$\hat{X}_{mle} = \arg\max_X p_Y(Y; X). \tag{168}$$

This section proposes a method for finding the MLE of X so that we may compare the covariance of $\hat{X}_{mle}$ to the CRLB. We evaluate the MLE bias and RMSE as well.

The MLE of $X = [N_o \; \mu \; \Lambda]^T$ is the value of X that maximizes (121) for the observed data, where the matrix C_x is expressed in terms of X. This is equivalent to maximizing the complex Wishart distribution [27, 76],

$$p_{\hat{C}_x}\left(\hat{C}_x\right) = \frac{1}{\pi^{2N_p} \left|\det(C_x)\right|^{N_p}} e^{-\mathrm{tr}\left(C_x^{-1}\hat{C}_x\right)}, \tag{169}$$

with respect to X, where the matrix C_x is expressed in terms of X. As explained in Section 5.3.4, we do not use ρ for the estimation of X; thus, (169) must first be marginalized with respect to ρ. This marginalization, combined with the nonlinear mapping from X to the terms in C_x, makes finding the MLE a nonlinear non-convex optimization problem.

To circumvent this potentially difficult non-convex optimization problem, we propose an alternate method for finding $\hat{X}_{mle}$. Since the number of measurements (i.e., $\dim(Y)$) is equal to the number of unknown parameters (i.e., $\dim(X)$), the MLE of X is the solution to the system of equations relating the DSD parameters to the radar measurements or, equivalently,

$$\hat{X}_{mle} = \arg\min_{\tilde{X}} G\left(\tilde{X}\right), \tag{170}$$

where $\min G(X) = 0$ and

$$G(X) = \frac{1}{2}\left(\left[\eta_h(X) - \hat{\eta}_h\right]^2 + \left[\eta_v(X) - \hat{\eta}_v\right]^2 + \left[K_{DP}(X) - \hat{K}_{DP}\right]^2\right). \tag{171}$$

This solution follows from the functional invariance property of the MLE [45], which states $\hat{\beta}_{mle} = f_\beta(\hat{\alpha}_{mle})$, where $\beta = f_\beta(\alpha)$ [45]. While the function $G(X)$ is still nonlinear and non-convex, this formulation can be reduced to a two-dimensional problem (versus a three-dimensional problem) before applying the Nelder-Mead simplex search (NMSS) method [50]. This is done as follows. Optimizing $G(X)$ with respect to N_o yields

$$\frac{\partial G}{\partial N_o} = \left[\eta_h(X) - \hat{\eta}_h\right]\frac{\partial \eta_h}{\partial N_o} + \left[\eta_v(X) - \hat{\eta}_v\right]\frac{\partial \eta_v}{\partial N_o} + \left[K_{DP}(X) - \hat{K}_{DP}\right]\frac{\partial K_{DP}}{\partial N_o} = 0. \tag{172}$$

Recall from Section 5.3.4.1 that

$$\eta_h = N_o \frac{\partial \eta_h}{\partial N_o}, \tag{173}$$

$$\eta_v = N_o \frac{\partial \eta_v}{\partial N_o}, \tag{174}$$

and

$$K_{DP} = N_o \frac{\partial K_{DP}}{\partial N_o}, \tag{175}$$

where the partial derivatives in (173) - (175) are only functions of μ and Λ (i.e., not N_o), e.g.,

$$\frac{\partial \eta_h}{\partial N_o} = \frac{\partial \eta_h}{\partial N_o}(\mu, \Lambda). \tag{176}$$

Substituting (173) - (175) into (172) yields the value of N_o that minimizes $G(X)$ for a given value of μ and Λ:

$$N_o(\mu, \Lambda) = \frac{\hat{\eta}_h \frac{\partial \eta_h}{\partial N_o} + \hat{\eta}_v \frac{\partial \eta_v}{\partial N_o} + \hat{K}_{DP} \frac{\partial K_{DP}}{\partial N_o}}{\left(\frac{\partial \eta_h}{\partial N_o}\right)^2 + \left(\frac{\partial \eta_v}{\partial N_o}\right)^2 + \left(\frac{\partial K_{DP}}{\partial N_o}\right)^2}. \tag{177}$$

Substituting this equation into (171) for N_o, or equivalently setting $X = [N_o(\mu, \Lambda) \ \mu \ \Lambda]^T$, allows us to write $G(X)$ as a function of only μ and Λ, i.e., $G(\mu, \Lambda)$. The NMSS algorithm is then applied to $G(\mu, \Lambda)$.

5.5 Results

In this section, we compute the CRLB for a particular value of the DSD parameters. In addition, we perform a set of Monte Carlo trials in which the radar measurements are simulated according to the signal model, and the MLE of the DSD parameters is computed from the simulated radar measurements. Based on the results of these Monte Carlo simulations, the statistics of the MLE are evaluated and compared against the CRLB.

5.5.1 Experimental Set-up

The functions in (128) - (131) depend on the transmit wavelength, λ, of the radar. All experiments presented in this paper use $\lambda = 10$ cm, which is within the frequency range of the WSR-88D (2.7-3 GHz) [60]. Additionally, the coefficients in (128) - (131) depend on the particular model used to described the distribution of raindrop axis ratios. We use those coefficients, found in Chapter 4, corresponding to Andsager's

[3] model for the mean axis ratio of a raindrop and a zero-variance model for the distribution of the axis ratio of a raindrop.

For this experiment, we select a single set of DSD parameters to examine the CRLB along with the variance and bias of $\hat{X}_{mle}$ in detail:

$$X = \begin{bmatrix} N_o \\ \mu \\ \Lambda \end{bmatrix} = \begin{bmatrix} 10^4 \\ 1 \\ 2.5 \end{bmatrix}. \tag{178}$$

The value of X selected here is well within the typical range of realistic DSD parameters considered in current literature [15].

The CRLB depends not only on the value of the DSD parameters, but also the number of pulses, N_p, and the range span, Δ_R, over which K_{DP} is estimated. Initially, we consider the case where $N_p = 256$ (typical values of N_p for the WSR-88D range from 40 to 280 [60]) and $\Delta_R = 10$ km. Applying (167), we find the CRLB for the value of X in (178) is

$$J_F^{-1}(X) = \begin{bmatrix} 3.5415 \times 10^8 & -3.5851 \times 10^5 & -1.1171 \times 10^5 \\ -3.5851 \times 10^5 & 364.42 & 113.60 \\ -1.1171 \times 10^5 & 113.60 & 35.412 \end{bmatrix}. \tag{179}$$

Taking the square root of the diagonal terms of $J_F^{-1}(X)$ gives a bound for the standard deviation of an unbiased estimator $\hat{X}$; i.e.,

$$\sigma_{\hat{N}_o} \geq 1.8819 \times 10^4, \tag{180}$$

$$\sigma_{\hat{\mu}} \geq 19.09, \tag{181}$$

and

$$\sigma_{\hat{\Lambda}} \geq 5.95. \tag{182}$$

Before continuing with a computation of the MLE, a brief discussion of these results with a focus on two main concepts is warranted.

First, the current literature deems the typical range of DSD parameters to be those given in (117) [15]. Further, it is common practice to assume a uniform prior distribution on $\log_{10}(N_w)$, D_o, and μ over the ranges given in (117). A simple Monte Carlo simulation gives the covariance matrix of the corresponding prior on $X = [N_o\ \mu\ \Lambda]^T$ as

$$\mathrm{cov}(X) = \begin{bmatrix} 7.9890 \times 10^{13} & 8.5640 \times 10^{6} & 2.5462 \times 10^{6} \\ 8.5640 \times 10^{6} & 7.2994 & 2.4139 \\ 2.5462 \times 10^{6} & 2.4139 & 3.0000 \end{bmatrix}. \tag{183}$$

Taking the square root of the diagonal terms of the $\mathrm{cov}(X)$ gives the standard deviation of the prior on X; i.e.,

$$\sigma_{N_o} \geq 9.0317 \times 10^{6}, \tag{184}$$

$$\sigma_{\mu} \geq 2.7040, \tag{185}$$

and

$$\sigma_{\Lambda} \geq 1.7307. \tag{186}$$

Interestingly, the variance of an unbiased estimator of μ and Λ is greater than the variance that arises from randomly selecting a value from their prior distributions. Also, while the standard deviation of an unbiased estimator of N_o is significantly less than that which results from the prior, it is still greater than the value of N_o itself.

Second, a challenge may arise in computing $\hat{X}_{mle}$ and its respective statistics. Specifically, (128) - (131) are equations that well approximate the relationship between the DSD parameters and radar measurements over what current literature considers a realistic range of values for the DSD parameters. However, these approximations could break down at DSD parameter values significantly outside this range. This is certainly true in the case where the argument inside $\Gamma(\bullet)$ becomes negative since the gamma function has a discontinuity when its argument equals zero. Therefore, we aim to prevent $\hat{X}_{mle}$ from extending far beyond the range of realistic DSD

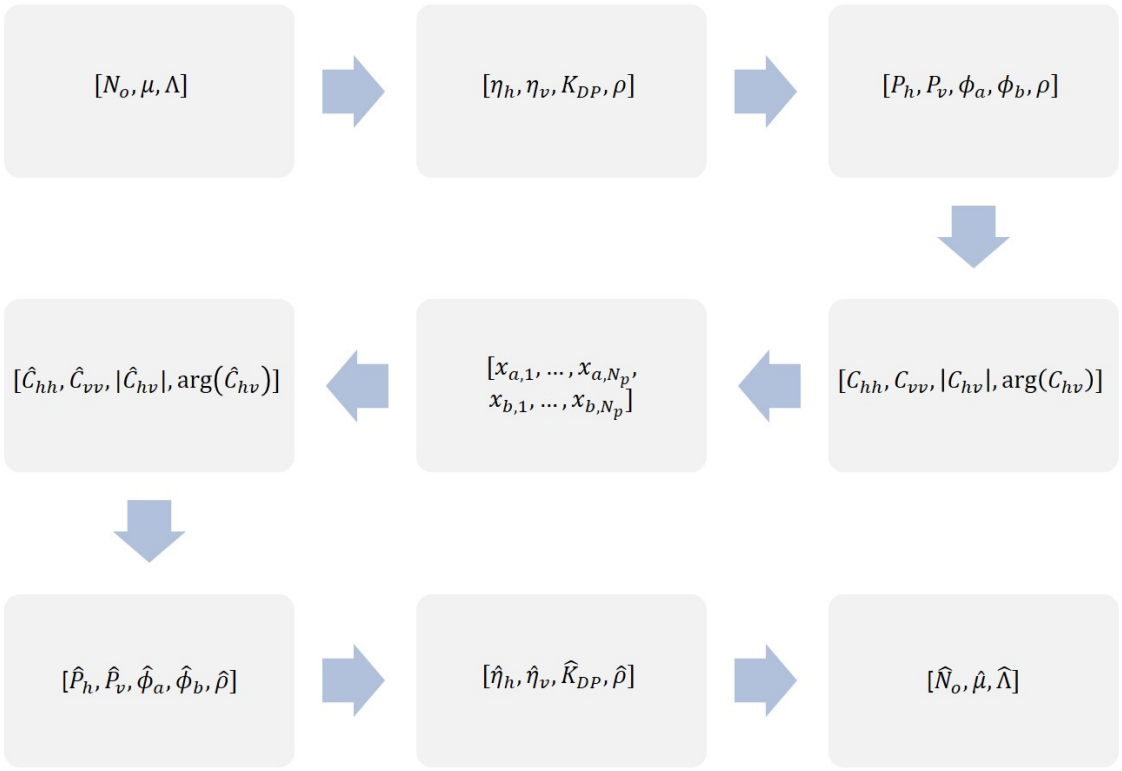

Figure 11: Flow diagram for data simulation and estimation

parameters for which the approximations of (128) - (131) have been validated. We also aspire to avoid the case where $\hat{\mu}_{mle}$ would result in (128) - (131) being evaluated at or near the gamma function discontinuities. Further, the gamma distribution, which is used to describe the DSD, is only valid for values of $\mu > -1$. Therefore, we require a value of N_p that reduces the variance of $\hat{X}_{mle}$ such that it is unlikely that $\hat{\mu}_{mle} < -1$. Based on the CRLB given in (179), the variance of $\hat{X}_{mle}$ will be large enough that these issues cannot be avoided when using a realistic value for N_p. Thus, we reduce the estimator variance by selecting $N_p = 2^{17}$. Again, we recognize such a value is impractical, but it permits the computation and comparison of $\hat{X}_{mle}$ to the CRLB.

For the parameters described above, $N_s = 100,000$ trials were generated according to the signal model of Section 5.2. For each trial, a dwell of i.i.d. pulses was simulated for two resolution volumes. The simulation flow is shown in Figure 11. Given a

Table 5: MLE Statistics

	N_o	μ	Λ
Value	10,000	1	2.5
$b\left(\hat{X}_{mle}\right)$	-283.13	0.3531	0.1102
$\sigma\left(\hat{X}_{mle}\right)$	1754.18	2.0329	0.6339
$RMSE\left(\hat{X}_{mle}\right)$	1776.88	2.0634	0.6434

Table 6: Square root of diagonal terms of CRLB of DSD parameters

	N_o	μ	Λ
Value	10,000	1	2.5
$\sqrt{\left[J_F^{-1}\right]_{ii}}$	1663.37	1.6873	0.5260

specified value of X, a sequence of transformations was applied to define the terms in the covariance matrix, C_x, in (121). A sequence of pulses with the distribution of (121) was generated for two resolution volumes. The sample covariance of the generated data sequence provides the MLE of the terms in C_x. Then, the same sequence of inverse transforms is applied in reverse to arrive at the MLE of $Y = [\eta_h \ \eta_v \ K_{DP}]^T$. Since a closed-form expression for the inverse transform of (128) - (130) does not exist, we used the approach described in Section 5.4 to find $\hat{X}_{mle}$ from $\hat{Y}_{mle}$.

5.5.2 Eigenanalysis of CRLB and MLE

The sample bias, standard deviation, and RMSE of $\hat{X}_{mle}$, denoted $b\left(\hat{X}_{mle}\right)$, $\sigma\left(\hat{X}_{mle}\right)$, and $RMSE\left(\hat{X}_{mle}\right)$, respectively, as determined from the $N_s = 100,000$ Monte Carlo simulations, are given in Table 5. Comparing the sample standard deviation for each parameter in X to the square root of their CRLB, given in Table 6, allows us to conclude that an efficient estimator for X does not exist for two reasons. First, the sample bias of the MLE, $b\left(\hat{X}_{mle}\right)$, is non-negligible. This implies $\hat{X}_{mle}$ is a biased estimator. Second, the variance of $\hat{X}_{mle}$ is significantly greater than that specified by the CRLB. However, while the CRLB is exceeded for this particular value of X, the

Table 7: Eigendecomposition of MLE sample covariance matrix of DSD parameters

$\sqrt{\lambda_v}$	1754.18	0.4465	0.0033
Sample EV	-1.0000	0.0012	0
	0.0011	0.9539	-0.3000
	0.0004	0.3000	0.9539

Table 8: Eigendecomposition of inverse FIM of DSD parameters

$\sqrt{\lambda_v}$	1663.37	0.1140	0.0009
CRLB EV	-1.0000	0.0011	0
	0.0010	0.9462	-0.3237
	0.0003	0.3237	0.9462

CRLB is only guaranteed to bound an unbiased estimator. Therefore, the variance of $\hat{X}_{mle}$ may very well be less than the CRLB for a different value of X. A similar bound on the RMSE of a biased estimator could be determined, but it requires knowledge of the estimator bias and the gradient of the estimator bias [86], and, hence, is not pursued here.

While the diagonal terms of the inverse FIM bound the variance of an unbiased estimator, $\hat{X}$, the inverse FIM also provides a bound on the "error volume" of an unbiased estimator. This error volume is referred to as a "concentration ellipse" (or ellipsoid, if the parameter set is greater than two dimensions) [86], and it accounts for the fact that the estimates, $\hat{N}_o$, $\hat{\mu}$, and $\hat{\Lambda}$, may be correlated. Given a sample covariance matrix, $\hat{C}_x$, the concentration ellipse of the data is determined by applying an eigendecomposition to the sample covariance matrix [36]:

$$\hat{C}_x = \boldsymbol{U}\boldsymbol{\Lambda}_{\boldsymbol{v}}\boldsymbol{U}^T, \tag{187}$$

where $\boldsymbol{U}$ is a unitary matrix such that each column corresponds to an eigenvector of $\hat{C}_x$ and $\boldsymbol{\Lambda}_{\boldsymbol{v}}$ is a diagonal matrix whose entries are the eigenvalues corresponding to each of the eigenvectors of $\hat{C}_x$. The eigenvectors correspond to the directions of the concentration ellipse's semi-principal axes (i.e., principal components), and the

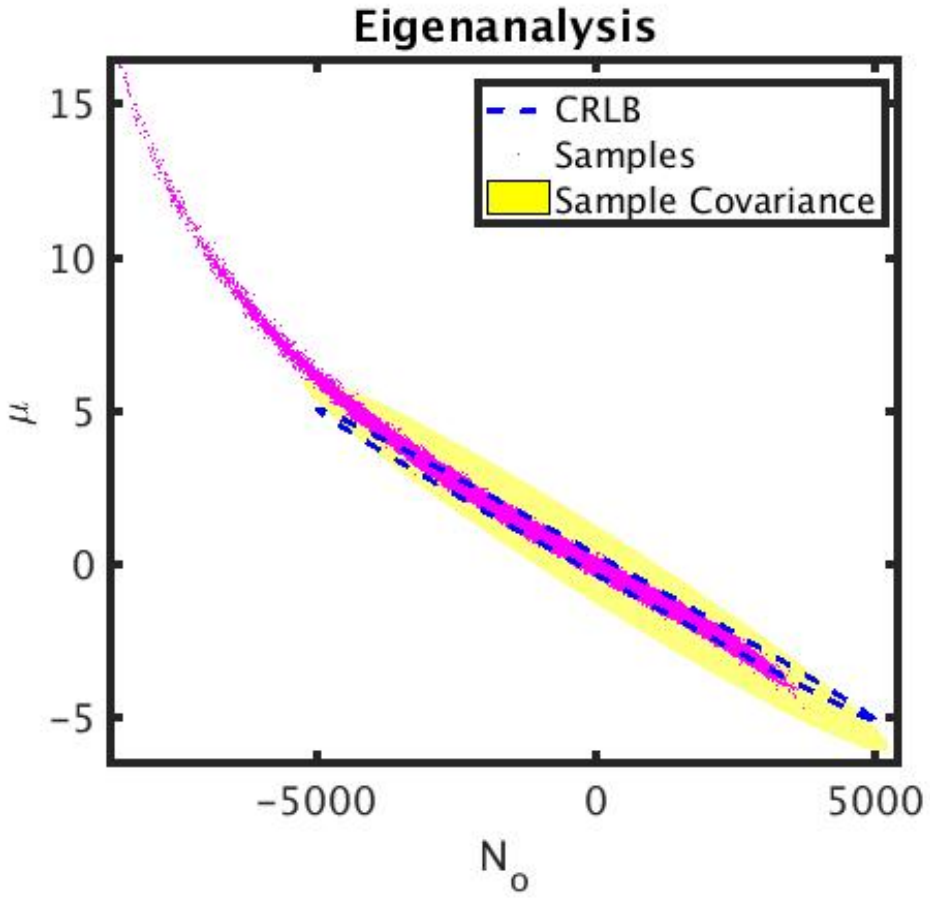

Figure 12: Concentration ellipses: N_o vs. μ.

square roots of the eigenvalues equal the length of the semi-principal axes, i.e., the estimator standard deviation in the direction of the principal components.

While performing an eigendecomposition on an estimator's sample covariance matrix gives the actual error volume of that estimator, performing an eigendecomposition on the inverse FIM establishes a lower bound on the error volume of an unbiased estimator. The eigenvalues and eigenvectors of both the MLE sample covariance matrix and the CRLB are given in Tables 7 and 8, respectively.

For ease of visualization, the eigendecompositions of the inverse FIM and sample covariance matrix, along with the associated concentration ellipses, are determined for each pair of parameters in X. The results are shown in Figures 12 - 14. In each

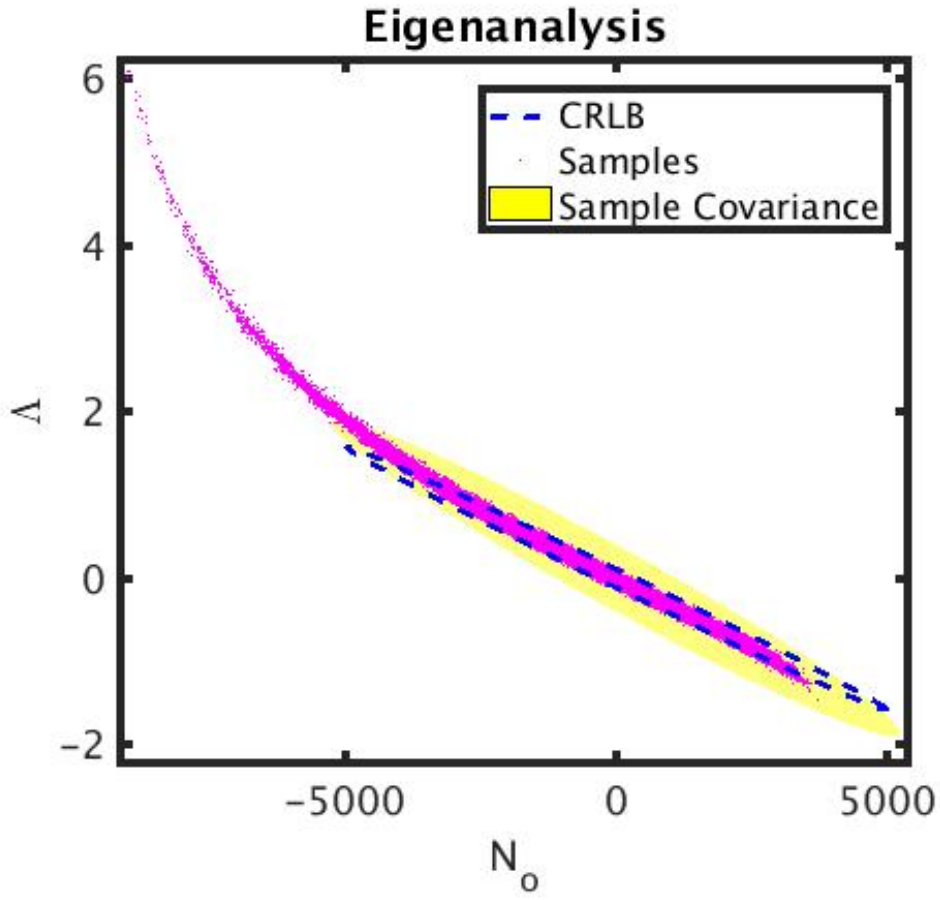

Figure 13: Concentration ellipses: N_o vs. Λ

figure, the drawn concentration ellipses correspond to three standard deviations from the estimator mean, i.e., $3\sqrt{\lambda_v}$, where λ_v is an eigenvalue of the covariance matrix. Additionally, the sample values of the MLE are plotted relative to the estimator mean.[2] The resulting plots show that the estimates of N_o, μ, and Λ are highly correlated.[3]

Some intuition regarding these results may be gained by considering a singular

[2]For better visualization, these plots have been zoomed in so that some sample outliers are not shown.

[3]Due to the high degree of correlation in the estimates of μ and Λ, the plots of the CRLB, sample covariance, and sample estimates in Figure 14 are difficult to visualize in a manner that they may all be distinguished.

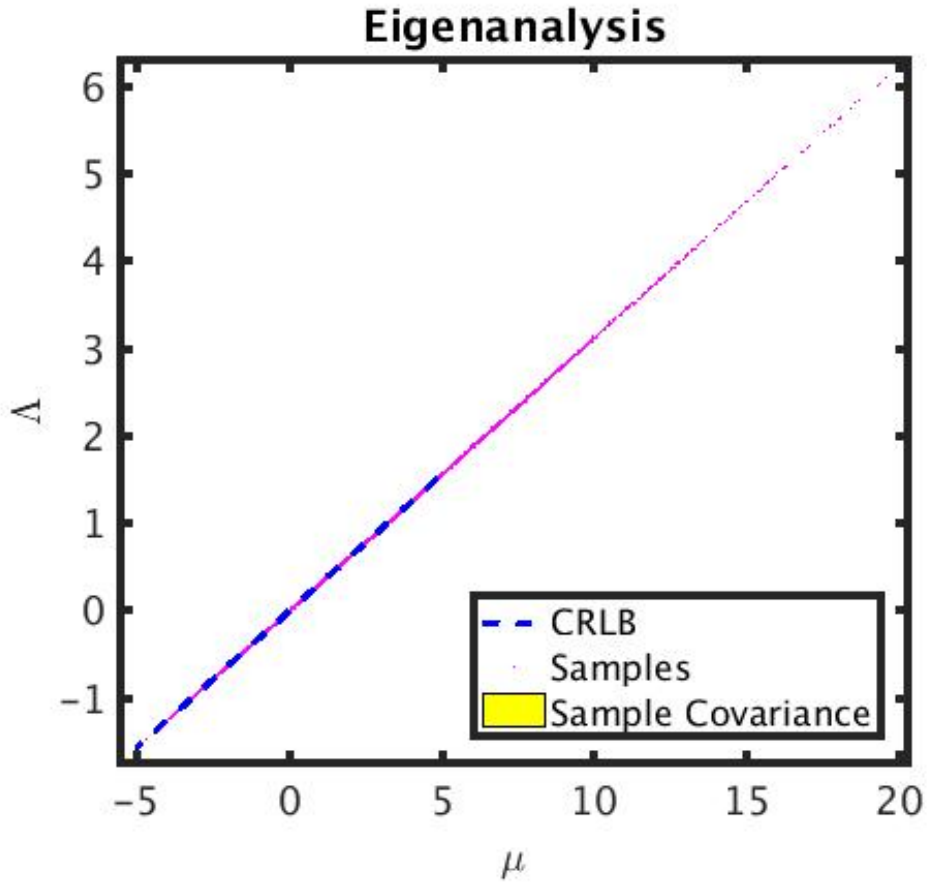

Figure 14: Concentration ellipses: μ vs. Λ

value decomposition (SVD) of the Jacobian $\frac{\partial Y}{\partial X}$ [80]:

$$\frac{\partial Y}{\partial X} = U \Sigma V^T, \tag{188}$$

where the columns of U are the eigenvectors of $\left(\frac{\partial Y}{\partial X}\frac{\partial Y}{\partial X}^T\right)$, the columns of V are the eigenvectors of $\left(\frac{\partial Y}{\partial X}^T\frac{\partial Y}{\partial X}\right)$, and Σ is a diagonal matrix containing the singular values of $\frac{\partial Y}{\partial X}$, which are equal to the square root of the eigenvalues of $\left(\frac{\partial Y}{\partial X}\frac{\partial Y}{\partial X}^T\right)$.

The Jacobian provides information regarding how each measurement varies as a result of changes in X. If all measurements have similar dependencies on X, then $\left(\frac{\partial Y}{\partial X}\frac{\partial Y}{\partial X}^T\right)$ will be near singular (i.e., the largest singular values of $\frac{\partial Y}{\partial X}$ will be significantly larger than the other singular values), and the estimates for the entries in X

Table 9: Singular values of the Jacobian $\frac{\partial Y}{\partial X}$

Σ_{11}	4.5027E-01
Σ_{22}	4.7404E-04
Σ_{33}	3.3028E-06

will be highly correlated. For the value of X considered in this paper, the singular values of $\frac{\partial Y}{\partial X}$ are given in Table 9. The second and third largest singular values, Σ_{22} and Σ_{33}, are four and six orders of magnitude smaller than the largest singular value, Σ_{11}, respectively. This suggests that, as the radar measurements relate to the parameters in X, there is not a high degree of independence between measurements, thus the significant correlation observed.

5.6 Summary

This chapter derived the CRLB of the parameters that describe the DSD of rain. To test the existence of an efficient estimator (i.e., an unbiased estimator that achieves the CRLB), we proposed an approach for finding the MLE of the DSD parameters. The experiments presented in this chapter suggest that an efficient estimator does not exist. Further, a detailed eigenanalysis of the CRLB and MLE was provided for the example value of X considered in this chapter. The results suggest that each measurement relates to the DSD parameters in very similar ways. As a result, parameter estimates are highly correlated.

To draw more extensive and substantial conclusions regarding the ability to estimate DSD parameters with dual-pol radar measurements, a more extensive parametric analysis of the CRLB and MLE properties is performed in Chapter 6. However, initial experiments suggest parameter estimates are highly correlated and that, unless additional (i.e., prior) information is incorporated into such estimates, the resulting estimates may have a high RMSE due to bias and high variance.

CHAPTER VI

PARAMETRIC ANALYSIS OF VARIANCE BOUNDS AND MAXIMUM-LIKELIHOOD ESTIMATOR PROPERTIES FOR DROP SIZE DISTRIBUTION PARAMETERS

6.1 Overview

While Chapter 5 examined the CRLB and statistics of the MLE,

$$\hat{X}_{mle} = \begin{bmatrix} \hat{N}_{o_{mle}} \\ \hat{\mu}_{mle} \\ \hat{\Lambda}_{mle} \end{bmatrix}, \tag{189}$$

in detail for a single value of the DSD parameters, this chapter presents a more extensive parametric analysis of the CRLB and MLE. To ascertain trends in the CRLB and MLE statistics as a function of the DSD parameters, we evaluate the CRLB and MLE statistics over an array of realistic DSD parameters for one of the nine raindrop axis ratio models presented in Chapter 4. Then, over the same range of DSD parameters, we compare and contrast the derived CRLB for all nine of the different axis ratio models to determine how the various models impact the derived bounds.

This chapter is organized as follows. Section 6.2 begins by describing the set-up for the experiments performed in this chapter, along with stipulating the value of relevant experimental parameters. Section 6.3 presents an evaluation of the CRLB of each of the DSD parameters over the designated range of DSD parameter values. In addition, a Monte Carlo analysis is performed in which the statistics of the MLE are computed and compared against the CRLB. Then, Section 6.4 compares and

contrasts the derived CRLB for the various PDF models for the axis ratio of rain drops.

6.2 Experimental Set-up

In Section 6.3, we calculate the CRLB for an array of DSD parameters to determine how the CRLB changes as a function of these parameters. Furthermore, for each set of parameter values, we perform $N_s = 1,000,000$ Monte Carlo trials to estimate the statistics of $\hat{X}_{mle}$. For each Monte Carlo trial, radar measurements are simulated according to the signal model described in Section 5.2, and, from those measurements, the MLE of the DSD parameters is determined. From these Monte Carlo trials, the bias, standard deviation, and RMSE of the MLE are estimated and plotted as a function of the DSD parameters.

Many of the parameters for this experiment are identical to those in the experiment presented in Section 5.5; i.e., $\Delta_R = 10$ km, $\lambda = 10$ cm, and the Andsager-Zero axis ratio model is used. The number of pulses per simulated dwell is $N_p = 2^{17}$.

The experiments use the following nominal value for the DSD parameters:

$$X_{nom} = \begin{bmatrix} N_{o_{nom}} \\ \mu_{nom} \\ \Lambda_{nom} \end{bmatrix} = \begin{bmatrix} 10^4 \\ 1 \\ 2.5 \end{bmatrix}. \tag{190}$$

In each of the three experiments presented in Section 6.3, two of the DSD parameters are kept constant at their nominal value, while the third is swept over a range of values. The first experiment varies N_o from $N_o = 10^{3.5}$ to $N_o = 10^5$; the second experiment varies μ from $\mu = 0$ to $\mu = 5$; and the third experiment varies Λ from $\Lambda = 1.75$ to $\Lambda = 3$.

The range of DSD parameter values used in these experiments is partially motivated by the typical ranges given in (117) [15]. Further, while we have selected $N_p = 2^{17}$ to avoid the computational concerns previously mentioned in Section 5.5.1,

it is also necessary to restrict the range of DSD parameters considered without significantly increasing the value of N_p even further. Thus, parameter values for these experiments are selected such that the probable range of the MLEs, as predicted by the computed CRLB of X, are such that this computational issue may be avoided.

6.3 CRLB and MLE Analysis

The results of the three experiments described in Section 6.2 are shown in Figures 15 - 17. In each figure, there are six plots, two for each of the three DSD parameters. For each DSD parameter, the first plot (on the left) shows the square root of the CRLB, the standard deviation of the MLE, and the RMSE of the MLE, while the second plot (on the right) displays the MLE bias.

Figure 15 shows how the CRLB and MLE statistics vary with the value of N_o while keeping the values of μ and Λ fixed at their nominal values. The results indicate that with increasing N_o, the measurements enable a better estimate of μ and Λ, but a worse estimate of N_o. Particularly, as N_o increases, the bias, variance, and, consequently, RMSE of $\hat{\mu}_{mle}$ and $\hat{\Lambda}_{mle}$ decrease. In contrast, the opposite trends are seen for $\hat{N}_{o_{mle}}$.

Figure 16 shows how the CRLB and MLE statistics vary with the value of μ while keeping the values of N_o and Λ fixed at their nominal values. The results indicate that with increasing μ, the measurements enable a better estimate of μ and Λ, whereas, when $\mu > 0.5$, the quality of $\hat{N}_{o_{mle}}$ becomes increasingly worse. Specifically, as μ increases, the bias, variance, and, consequently, RMSE of $\hat{\mu}_{mle}$ and $\hat{\Lambda}_{mle}$ decrease. In contrast, the bias and variance of $\hat{N}_{o_{mle}}$ has a local minimum around $\mu = 0.5$.

Figure 17 shows how the CRLB and MLE statistics vary with the value of Λ while keeping the values of N_o and μ fixed at their nominal values. The results indicate that with increasing Λ, the estimates of μ and Λ become increasingly worse. Particularly, as Λ increases, the bias, variance, and, consequently, RMSE of $\hat{\mu}_{mle}$ and $\hat{\Lambda}_{mle}$ increase. However, the quality of $\hat{N}_{o_{mle}}$ improves slightly with increasing Λ until

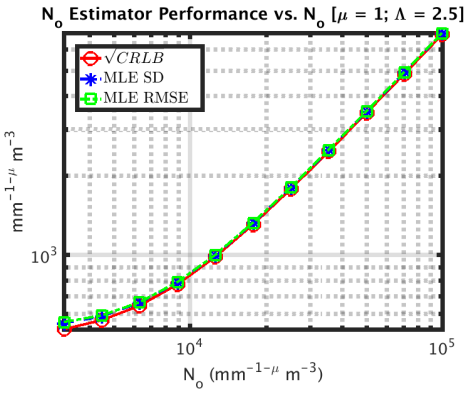

(a) CRLB and MLE statistics for N_o

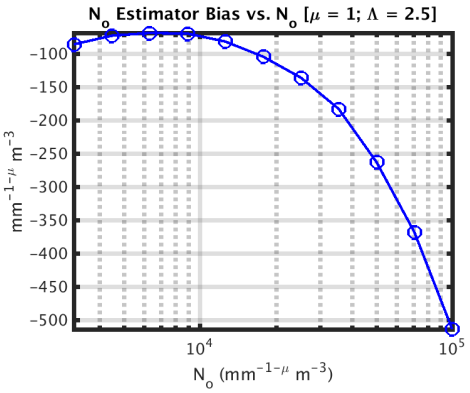

(b) MLE bias for N_o

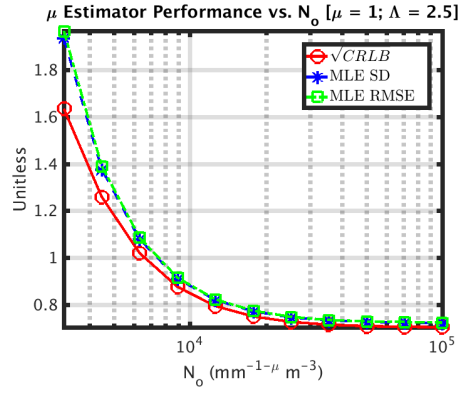

(c) CRLB and MLE statistics for μ

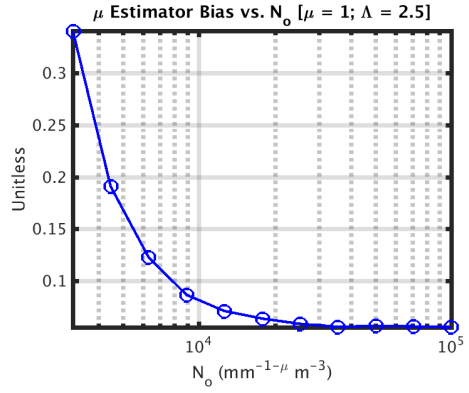

(d) MLE bias for μ

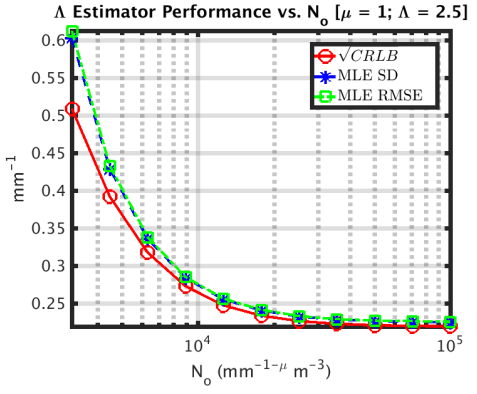

(e) CRLB and MLE statistics for Λ

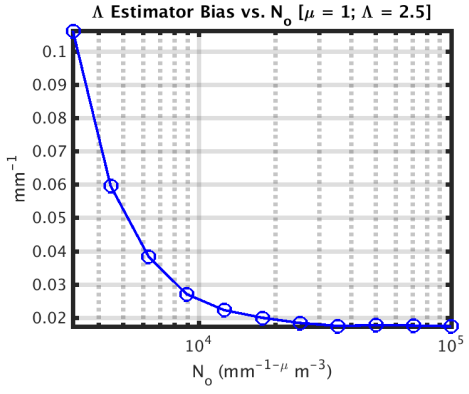

(f) MLE bias for Λ

Figure 15: CRLB and MLE statistics of DSD parameters versus N_o while keeping the values $\mu = 1$ and $\Lambda = 2.5$ fixed.

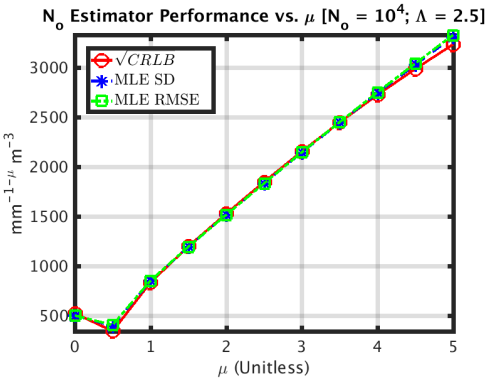

(a) CRLB and MLE statistics for N_o

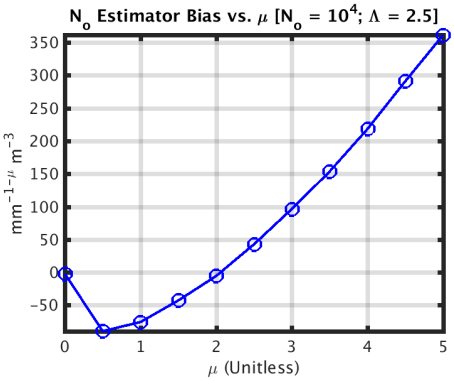

(b) MLE bias for N_o

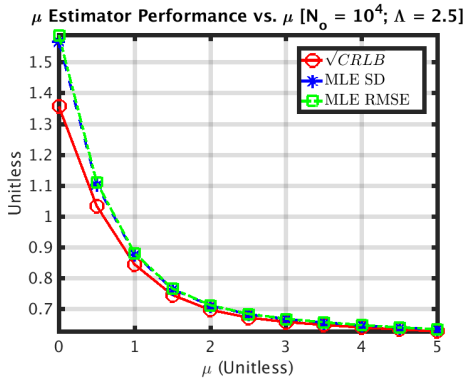

(c) CRLB and MLE statistics for μ

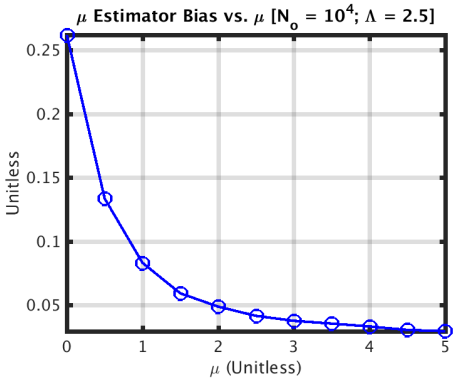

(d) MLE bias for μ

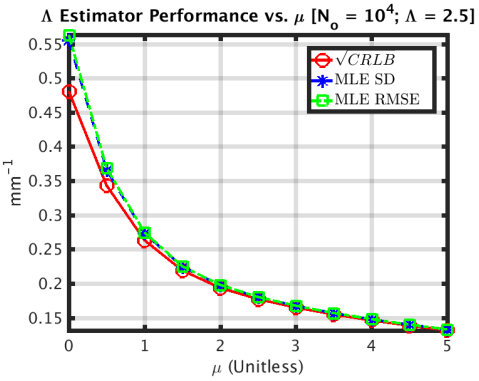

(e) CRLB and MLE statistics for Λ

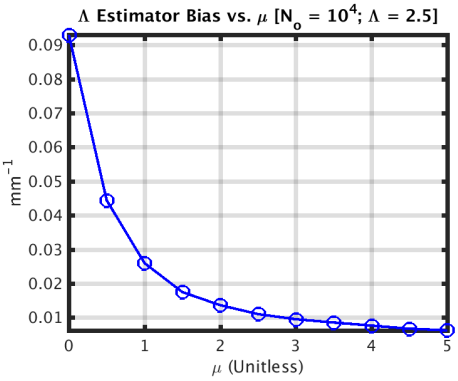

(f) MLE bias for Λ

Figure 16: CRLB and MLE statistics of DSD parameters versus μ while keeping the values $N_o = 10^4$ and $\Lambda = 2.5$ fixed.

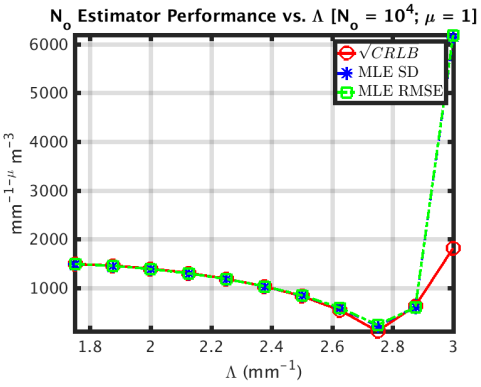

(a) CRLB and MLE statistics for N_o

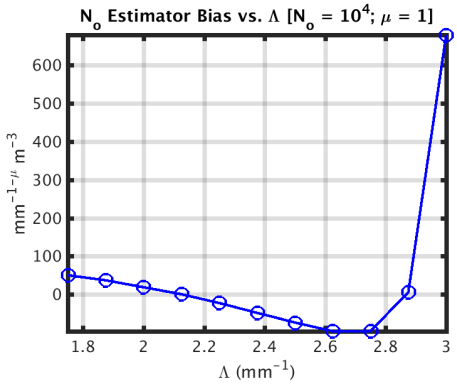

(b) MLE bias for N_o

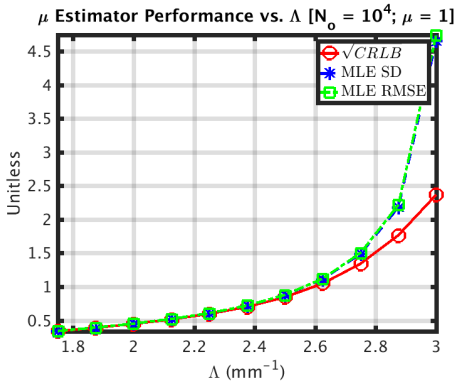

(c) CRLB and MLE statistics for μ

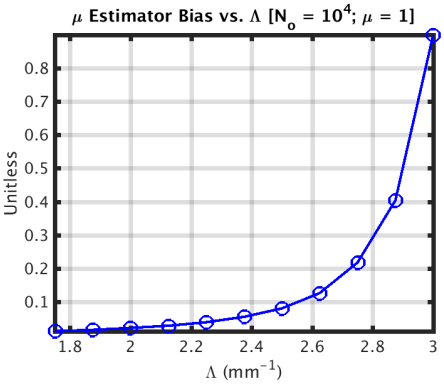

(d) MLE bias for μ

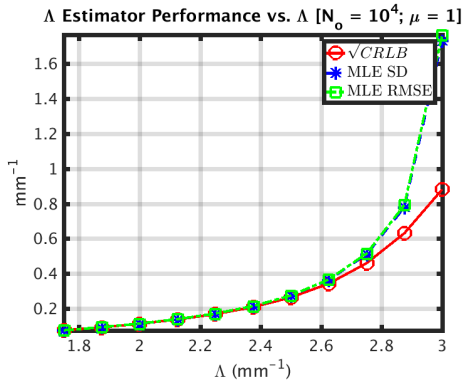

(e) CRLB and MLE statistics for Λ

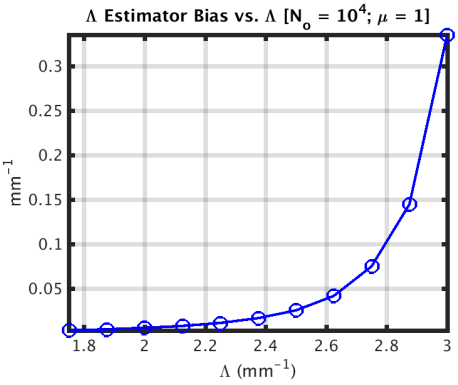

(f) MLE bias for Λ

Figure 17: CRLB and MLE statistics of DSD parameters versus Λ while keeping the values $N_o = 10^4$ and $\mu = 1$ fixed.

around $\Lambda = 2.75$, where estimator bias and variance increase drastically.

The results presented in this section are consistent with those in Chapter 5; the MLE is biased, and, in general, the variance exceeds the CRLB for a wide range of DSD parameters. Thus, the MLE of the DSD parameters is not an efficient estimator, and an efficient estimator does not exist.

Even if the MLE is not efficient, it is asymptotically efficient [45]; i.e., as $N_p \to \infty$, the MLE becomes unbiased and achieves the CRLB. Thus, while the experiments presented here for $N_p = 2^{17}$ indicate the CRLB is a relatively tight bound for the variance of $\hat{X}_{mle}$, the bound is likely much looser as N_p becomes smaller. Similarly, the bias of $\hat{X}_{mle}$ is likely to change as N_p decreases. These trends are a result of the nonlinear relationship that exists between the the DSD parameters and radar measurements, for which efficient estimators do exist [76, 27]. Consequently, the variance of the MLE does not scale with $\frac{1}{N_p}$ as the CRLB does.

6.4 CRLB for Different Raindrop Shape Models

To derive the CRLB in Chapter 5, we used (128) - (131), which assume a probabilistic model for the shape of raindrops. The different axis ratio models were distinguished by the exact expression used to define the mean and standard deviation of the axis ratio PDF. Three different models were considered for the mean axis ratio: Andsager et al. [3], Beard and Chuang [5], and Brandes et al.[9]. Further, three different models were considered for the standard deviation of the axis ratio: a zero standard deviation, the "proportional" model of Bringi et al. [14], and the model of Jameson [40]. Considering each combination of the three models for the mean and the three models for the standard deviation, there are nine possible models for the PDF of the axis ratio.

In this section, the CRLB is computed using all the same parameters as the experiments in Section 6.2 except $N_p = 256$, which is within the typical number of

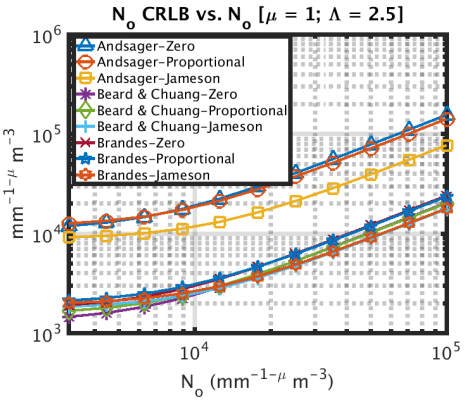

(a) CRLB of N_o

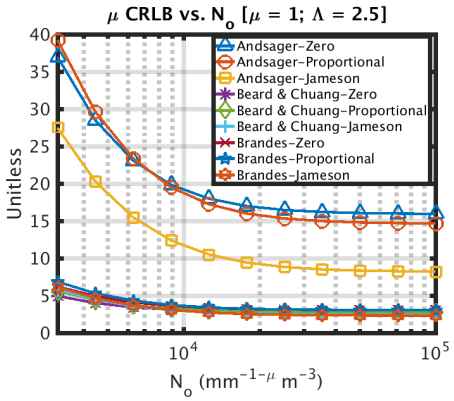

(b) CRLB of μ

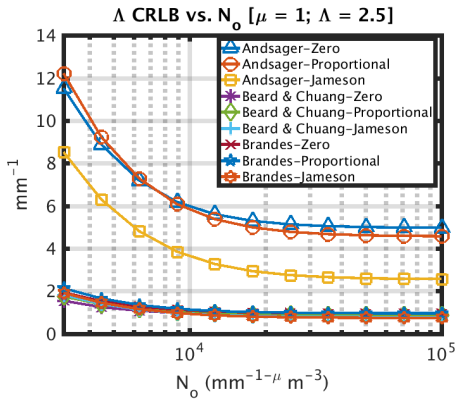

(c) CRLB of Λ

Figure 18: CRLB of DSD parameters for different axis ratio models versus N_o while keeping the values $\mu = 1$ and $\Lambda = 2.5$ fixed.

pulses used by the WSR-88D to estimate the dual-pol data products [60]. Figures 18 - 20 show the CRLB for each of the nine axis ratio models. Each figure contains three plots, one for each of the DSD parameters. In each figure, two of the DSD parameters are kept constant at their nominal value while the third is swept over an array of values. Figure 18 sweeps over N_o; Figure 19 sweeps over μ; and Figure 20 sweeps over Λ.

Interestingly, while the general trends of the CRLB are similar for each of the models, the Andsager model for the mean axis ratio of rain drops results in a significantly larger CRLB over the array of DSD parameter values considered in this chapter. Given that the three different models for $\mu_r\,(D_e)$ do not vary significantly

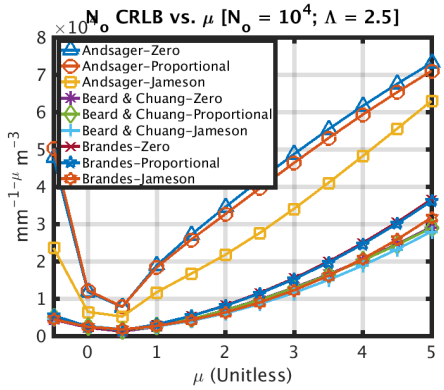

(a) CRLB of N_o

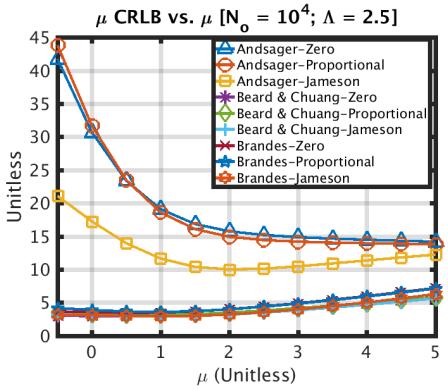

(b) CRLB of μ

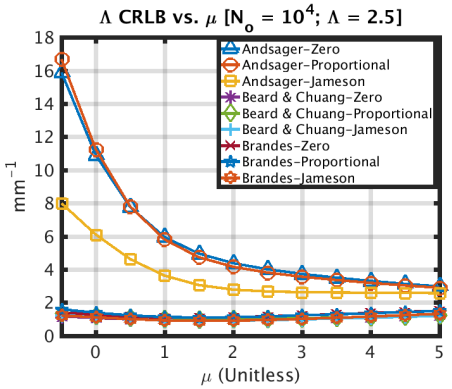

(c) CRLB of Λ

Figure 19: CRLB of DSD parameters for different axis ratio models versus μ while keeping the values $N_o = 10^4$ and $\Lambda = 2.5$ fixed.

in the span of realistic drop sizes ($D_e < 6$ mm), it may be surprising to see such differences in the CRLB for the various models. Some intuition regarding these results may be gained by considering an SVD of the Jacobian of the transformation, $Y = f_Y(X)$, which maps the DSD parameters, $X = [N_o\ \mu\ \Lambda]^T$, to the radar measurements, $Y = [\eta_h\ \eta_v\ K_{DP}]^T$. For each of the nine axis ratio models, Table 10 lists the singular values of the Jacobian, $\frac{\partial Y}{\partial X}$, evaluated at $X = X_{nom}$, along with the associated condition number. The condition number is the ratio of the largest singular value, Σ_{11}, to the smallest singular value, Σ_{33}, i.e.,

$$\kappa = \frac{\Sigma_{11}}{\Sigma_{33}}. \tag{191}$$

Large condition numbers indicate that the function $f_Y(X)$ is highly sensitive to small

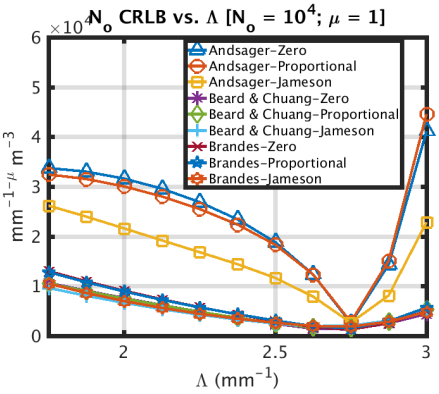

(a) CRLB of N_o

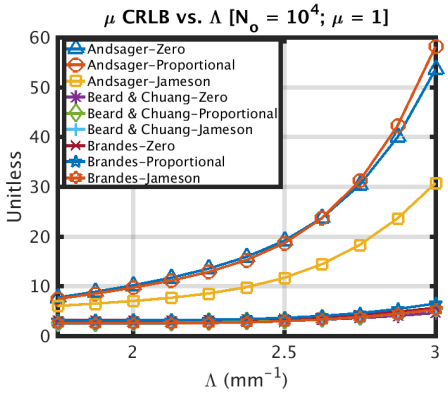

(b) CRLB of μ

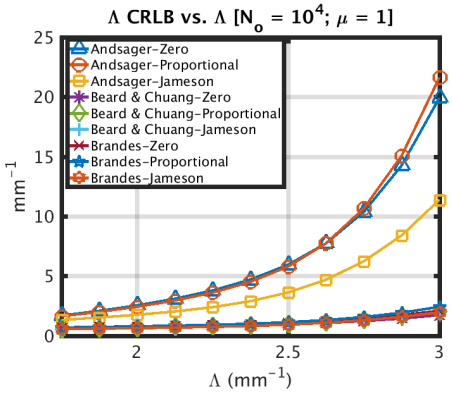

(c) CRLB of Λ

Figure 20: CRLB of DSD parameters for different axis ratio models versus Λ while keeping the values $N_o = 10^4$ and $\mu = 1$ fixed.

errors in X, *or*, in this case, the inverse function $f_Y^{-1}(Y)$ is highly sensitive to small errors in Y. Thus, large condition numbers associated with the Jacobian indicate that even small errors in the radar measurements translate to large errors in $\hat{X}_{mle}$. The condition numbers of the Jacobian associated with the Andsager models are largest. These results are consistent with the calculated CRLB of X, shown in Figures 18 - 20. Specifically, the larger the condition number of the Jacobian for a given model, the larger the CRLB of X.

Additionally, given the rather large condition numbers of the Jacobian, it is reasonable to conclude that even small changes to the Jacobian (i.e., changing the function

Table 10: Singluar values and condition numbers of the Jacobian $\frac{\partial Y}{\partial X}$ for all nine axis ratio models

Model	Σ_{11}	Σ_{22}	Σ_{33}	κ
Andsager-Zero	0.4503	4.7404E-04	3.3028E-08	1.3633E+07
Andsager-Proportional	0.4523	4.7697E-04	3.6722E-08	1.2318E+07
Andsager-Jameson	0.4604	5.2034E-04	6.7578E-08	6.8128E+06
Beard & Chuang-Zero	0.4514	4.4778E-04	2.6480E-07	1.7048E+06
Beard & Chuang-Proportional	0.4535	4.5130E-04	2.7294E-07	1.6616E+06
Beard & Chuang-Jameson	0.4617	5.0268E-04	3.2847E-07	1.4057E+06
Brandes-Zero	0.4549	5.1850E-04	2.2865E-07	1.9896E+06
Brandes-Proportional	0.4571	5.2221E-04	2.3642E-07	1.9333E+06
Brandes-Jameson	0.4668	5.8945E-04	3.2650E-07	1.4298E+06

coefficients even slightly based on different axis ratio models) could result in significant differences to both estimator quality (i.e., bias and variance) and the functional relationship between X and Y.

6.5 Summary

This chapter presented a parametric analysis of the CRLB and MLE for the DSD parameters of rain. The CRLB, for the DSD parameter values considered in this chapter, indicates that even if an efficient estimator existed, it would provide a poor estimate (i.e., high variance) of the DSD parameters, regardless of which axis ratio model is employed. The thorough parametric analysis of the MLE bias, variance, and RMSE are consistent with the results of Chapter 5, which suggest that an efficient estimator does not exist.

Additionally, this chapter examined how the different models for the axis ratio of raindrops impact the CRLB. Despite the fact that the different models for the mean axis ratio of a raindrop are very similar, the Andsager model for the mean axis ratio resulted in a significantly greater CRLB. This result was supported by the computed condition numbers of the Jacobian for each of the nine axis ratio models. Furthermore, the condition numbers of the Jacobian for all nine axis ratio models

were large, indicating that the measurements all depend on the DSD parameters in similar ways. As a result, the DSD parameter estimates have a high variance and are highly correlated.

Recall from Chapter 3 that a number of approaches have been proposed for the estimation of DSD parameters. However, all of these methods, in one way or another, effectively impose a constraining relationship [94, 10, 12, 93, 21, 22] or prior distribution [13, 29, 88] on the DSD parameters. The results in this chapter and the previous chapter suggest that these approaches must be highly dependent on the additional information introduced by the selected prior or constraining relationship. Furthermore, while several studies have been performed to evaluate the performance of various previously proposed estimation techniques [94, 88, 2], our results suggest that quantitative performance metrics such as RMSE are likely to be highly dependent upon the values of the DSD parameters that are represented in the test data, making it difficult to extrapolate estimator performance for a wider range of climatological conditions.

CHAPTER VII

VARIANCE BOUNDS FOR THE ESTIMATION OF RAIN RATE AND LIQUID WATER CONTENT

7.1 Overview

A number of approaches have been suggested for estimating rain rate and other intrinsic physical quantities of interest from dual-pol weather radars. Despite the extensive research done on this topic, no performance bounds for such estimators have been established. Thus, this chapter aims to establish such bounds. We begin with the CRLB of the DSD parameters, which was derived and analyzed in Chapters 5 and 6, and build on these results to establish the CRLBs of rain rate and LWC.

This chapter is organized as follows. Section 7.2 begins with a derivation of the CRLB of rain rate and LWC. This is followed with an extensive parametric analysis of the derived bounds. Section 7.3 describes the experiments performed for this analysis, and Section 7.4 presents the results, which include the CRLBs of rain rate and LWC over an array of DSD parameter values along with the statistics (i.e., bias, variance, and RMSE) of the MLE of each of these quantities. Next, Section 7.5 compares and contrasts the CRLBs of rain rate and LWC for the different PDF models for the shape (i.e., axis ratio) of rain drops. Lastly, Section 7.6 provides additional analysis and insight regarding the results presented in the previous sections.

7.2 Cramér-Rao Lower Bounds

Rain rate and LWC can both be expressed in terms of the DSD parameters, X. Thus, to derive the CRLB of each of these quantities, we begin with the CRLB of X and apply the transformation property of the CRLB, as given in (138) [45].

7.2.1 CRLB of Rain Rate

The instantaneous still-air rain rate, given in millimeters per hour, is [25]

$$R_r = 0.6\pi \times 10^{-3} \int_0^\infty v\left(D_e\right) D_e^3 N\left(D_e; X\right)\ dD_e, \tag{192}$$

where $v\left(D_e\right)$ is the terminal velocity of a raindrop of diameter D_e in meters per second. To compute rain rate, we require an expression for the terminal velocity of a raindrop, for which a common approximation is [26]

$$v\left(D_e\right) \approx a_t D_e^{b_t}, \tag{193}$$

where $a_t = 3.78$ and $b_t = 0.67$. This approximation is a power-law fit to the precise terminal velocity measurements of Gunn and Kinzer [34]. Substituting (2) and (193) into (192) and integrating yields a closed-form equation for rain rate in terms of the DSD parameters:

$$R_r = 0.6\pi \times 10^{-3} \frac{a_t N_o}{\Lambda^{\mu+b_t+4}} \Gamma\left(\mu + b_t + 4\right). \tag{194}$$

To apply (138), we find the Jacobian of (194):

$$\frac{\partial R_r}{\partial X} = \begin{bmatrix} \frac{\partial R_r}{\partial N_o} \\ \frac{\partial R_r}{\partial \mu} \\ \frac{\partial R_r}{\partial \Lambda} \end{bmatrix}, \tag{195}$$

which is

$$\frac{\partial R_r}{\partial X} = \begin{bmatrix} \frac{1}{N_o} R_r \\ \left[\Psi_0\left(\mu + b_t + 4\right) - \ln\left(\Lambda\right)\right] R_r \\ -\frac{(\mu+b_t+4)}{\Lambda} R_r \end{bmatrix}. \tag{196}$$

The CRLB of rain rate is then easily computed as

$$J_F^{-1}\left(R_r\right) = \frac{\partial R_r}{\partial X} J_F^{-1}\left(X\right) \frac{\partial R_r}{\partial X}^H, \tag{197}$$

where $J_F^{-1}\left(X\right)$ is given in (167) and $\frac{\partial R_r}{\partial X}$ is given in (196). Interestingly, the CRLB of rain rate cannot be expressed as a function of only itself. In other words, the

performance of an unbiased estimator of rain rate depends not only on the value of R_r, but on the DSD of the falling rain. This is not surprising since two different DSDs can yield identical rain rates, but different radar measurements.

7.2.2 CRLB of Liquid Water Content

LWC is a measure of the amount of cloud water in a unit volume and is given by [15]

$$W = \frac{\pi}{6}\rho_w \int_0^\infty D_e^3 N\left(D_e; X\right) dD_e, \tag{198}$$

where ρ_w is the density of water (10^3 kg/m^3). Substituting (2) into (198) and integrating yields a closed-form equation for LWC in terms of the DSD parameters:

$$W = \frac{\pi}{6}\rho_w \frac{N_o}{\Lambda^{\mu+4}}\Gamma\left(\mu+4\right). \tag{199}$$

To apply (138), we first find the Jacobian of (199):

$$\frac{\partial W}{\partial X} = \begin{bmatrix} \frac{\partial W}{\partial N_o} \\ \frac{\partial W}{\partial \mu} \\ \frac{\partial W}{\partial \Lambda} \end{bmatrix}, \tag{200}$$

which is

$$\frac{\partial W}{\partial X} = \begin{bmatrix} \frac{1}{N_o} W \\ \left[\Psi_0\left(\mu+4\right) - \ln\left(\Lambda\right)\right] W \\ -\frac{(\mu+4)}{\Lambda} W \end{bmatrix}. \tag{201}$$

Then, the CRLB of LWC is straightforwardly computed as

$$J_F^{-1}\left(W\right) = \frac{\partial W}{\partial X} J_F^{-1}\left(X\right) \frac{\partial W}{\partial X}^H, \tag{202}$$

where $J_F^{-1}\left(X\right)$ is given in (167) and $\frac{\partial W}{\partial X}$ is given in (201). Like rain rate, the CRLB of LWC cannot be expressed as a function of only itself; the performance of an unbiased LWC estimator also depends on the DSD of the liquid water aloft.

7.3 Experimental Set-up

In addition to deriving and examining the CRLB of the given quantities of interest, we investigate the statistics of the MLE for each of these quantities and compare the results to the CRLB. To find the MLE of R_r and W, we first find the MLE of X, denoted as $\hat{X}_{mle}$, using the approach described in Chapter 5. Then, $\hat{R}_{r_{mle}}$ and $\hat{W}_{mle}$ are found by substituting $\hat{X}_{mle}$ into (194) and (199), respectively. This follows from the functional invariance property of the MLE [45].

The parameters for this experiment are identical to those in the experiments presented in Section 6.3; i.e., $N_p = 2^{17}$, $\Delta_R = 10$ km, $\lambda = 10$ cm, and the Andsager-Zero axis ratio model is used.

As before, the experiments use the following nominal value for the DSD parameters:

$$X_{nom} = \begin{bmatrix} N_{o_{nom}} \\ \mu_{nom} \\ \Lambda_{nom} \end{bmatrix} = \begin{bmatrix} 10^4 \\ 1 \\ 2.5 \end{bmatrix}. \tag{203}$$

In each experiment, two of the DSD parameters are kept constant at their nominal value, while the third is swept over a range of values. As before, the first experiment varies N_o from $N_o = 10^{3.5}$ to $N_o = 10^5$; the second experiment varies μ from $\mu = 0$ to $\mu = 5$; and the third experiment varies Λ from $\Lambda = 1.75$ to $\Lambda = 3$.

For each set of DSD parameter values, the values of R_r and W are computed along with their respective CRLBs. In addition, a Monte Carlo analysis of $N_s = 1,000,000$ trials is performed to generate the statistics of the MLEs, i.e., $\hat{W}_{mle}$ and $\hat{R}_{r_{mle}}$. The bias, standard deviation, and RMSE of the MLEs are computed and plotted as a function of the DSD parameters.

7.4 CRLB and MLE Analysis

The results of these experiments are shown in Figures 21 - 23. In each figure, there are six plots, three for each quantity of interest. The first two plots (top) show the values of R_r and W, computed as a function of the DSD parameters; the next two plots (middle) show the bias of the MLEs; and the final two plots (bottom) give the square root of the CRLB along with the standard deviation and RMSE of the MLEs. Figure 21 shows the aforementioned quantities, plotted as a function of N_o while keeping μ and Λ fixed; Figure 22 shows the same quantities, plotted as a function of μ while keeping N_o and Λ fixed; and Figure 23 shows these quantities as a function of Λ while keeping N_o and μ fixed.

In general, as R_r and W increase, so do the CRLB and standard deviation and RMSE of the MLE. There are local minimums in the MLE bias as a function of the DSD parameters; however, the bias is not the primary contributer to the RMSE.

As evidenced by the results presented here, the MLEs of both rain rate and LWC are biased, and the variance exceeds the CRLB for at least some values of the DSD parameters. Thus, the MLE of the DSD parameters is not an efficient estimator, and an efficient estimator does not exist.

Recall that even if the MLE is not efficient, it is asymptotically efficient [45]; i.e., as $N_p \to \infty$, the MLE becomes unbiased and achieves the CRLB. Thus, while the experiments presented here for $N_p = 2^{17}$ indicate the CRLB is a relatively tight bound for the variance of $\hat{R}_{rmle}$ and $\hat{W}_{mle}$, the bound is likely much looser as N_p becomes smaller. Similarly, the bias is likely to change as N_p decreases. These trends are a result of the nonlinear relationship of rain rate and LWC with the radar measurements. Consequently, the variance of the MLE does not scale with $\frac{1}{N_p}$ as the CRLB does.

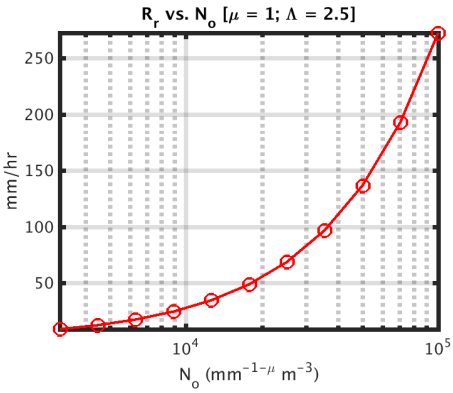

(a) Value of R_r

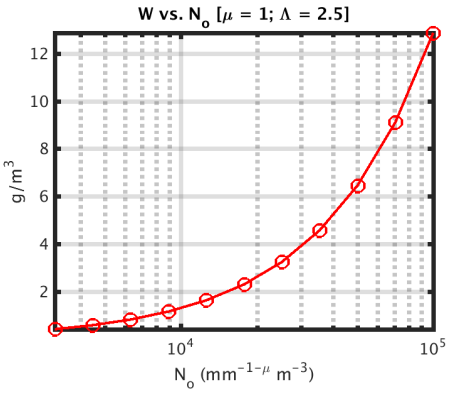

(b) Value of W

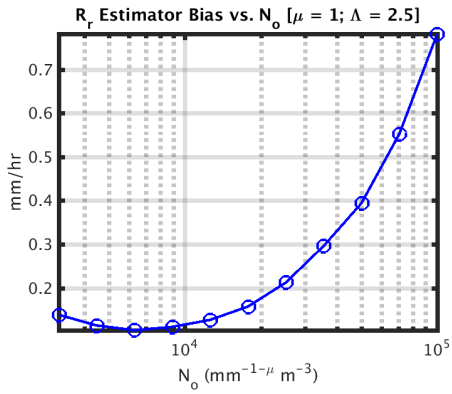

(c) MLE bias for R_r

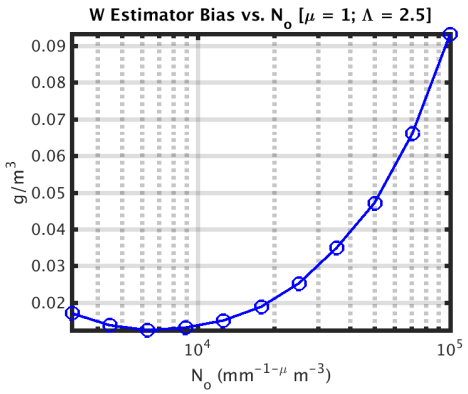

(d) MLE bias for W

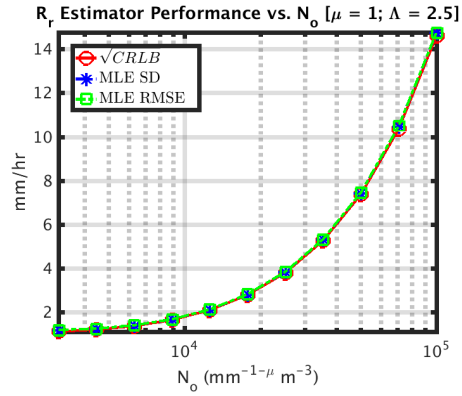

(e) CRLB and MLE statistics for R_r

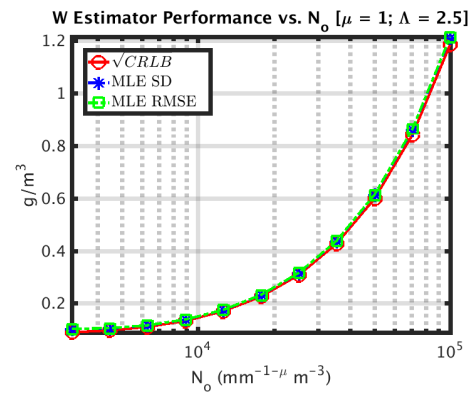

(f) CRLB and MLE statistics for W

Figure 21: CRLB and MLE statistics of rain rate and LWC versus N_o while keeping the values $\mu = 1$ and $\Lambda = 2.5$ fixed.

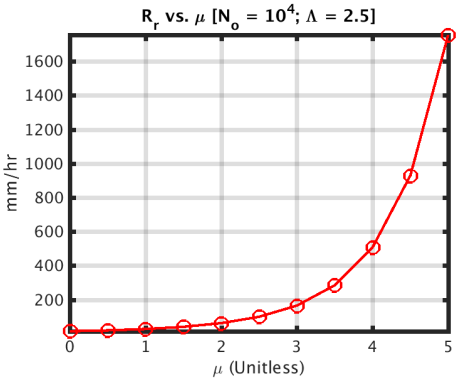

(a) Value of R_r

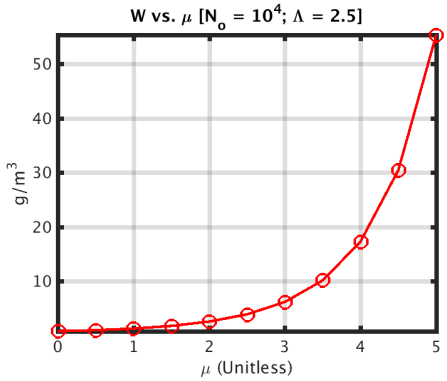

(b) Value of W

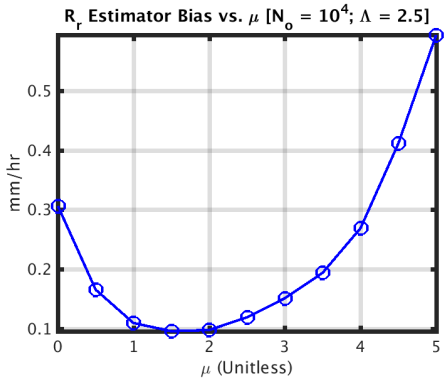

(c) MLE bias for R_r

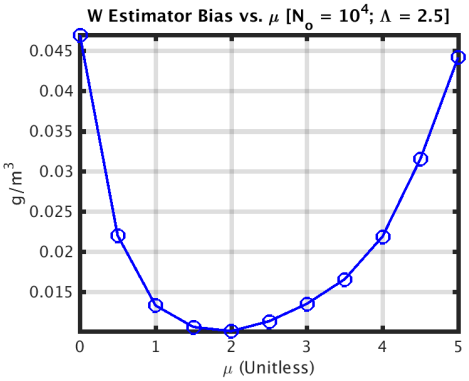

(d) MLE bias for W

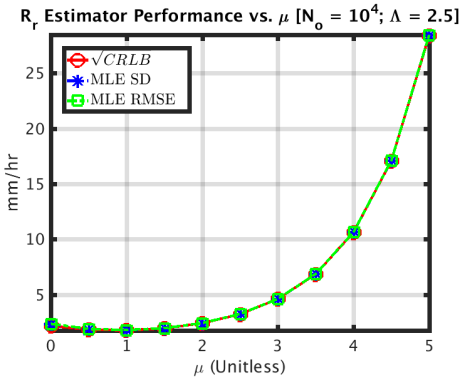

(e) CRLB and MLE statistics for R_r

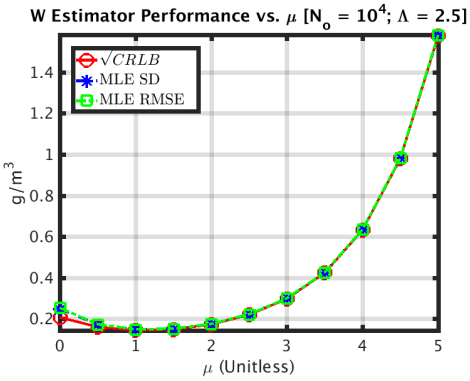

(f) CRLB and MLE statistics for W

Figure 22: CRLB and MLE statistics of rain rate and LWC versus μ while keeping the values $N_o = 10^4$ and $\Lambda = 2.5$ fixed.

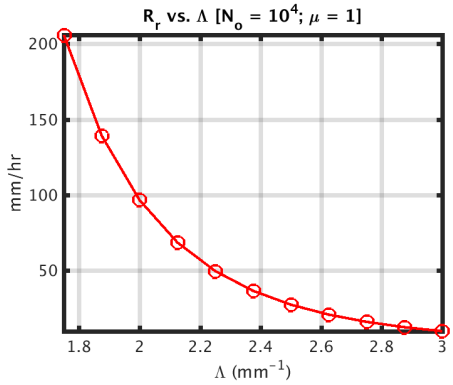

(a) Value of R_r

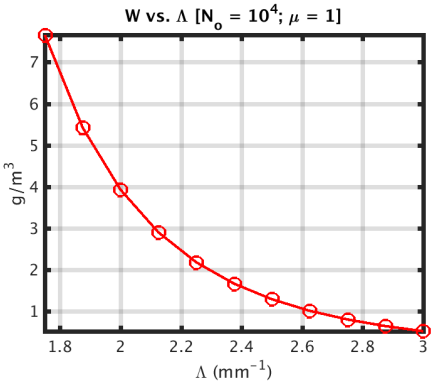

(b) Value of W

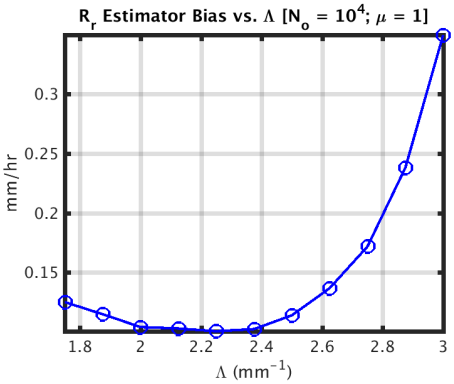

(c) MLE bias for R_r

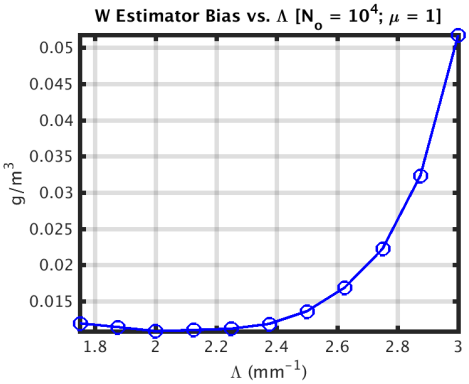

(d) MLE bias for W

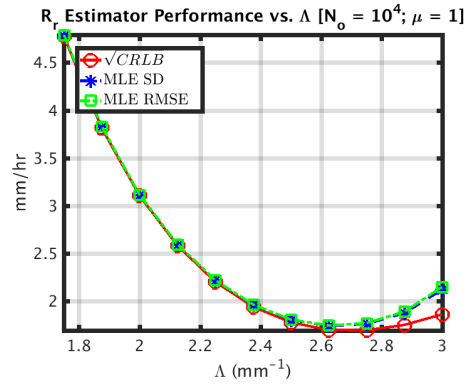

(e) CRLB and MLE statistics for R_r

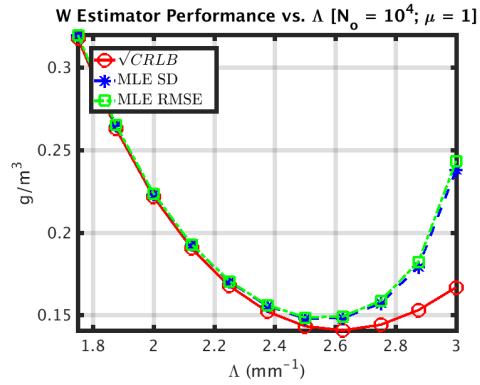

(f) CRLB and MLE statistics for W

Figure 23: CRLB and MLE statistics of rain rate and LWC versus Λ while keeping the values $N_o = 10^4$ and $\mu = 1$ fixed.

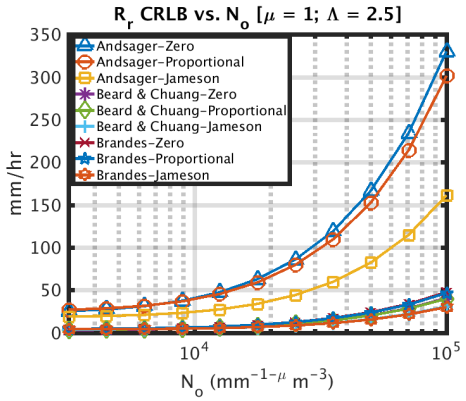

(a) CRLB of R_r versus N_o

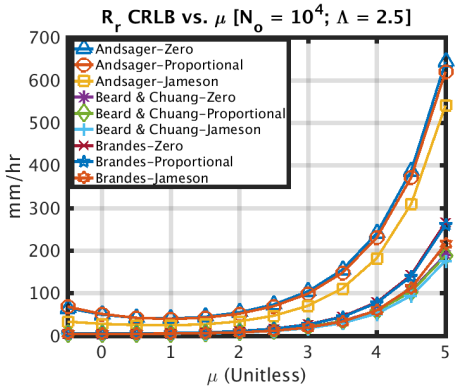

(b) CRLB of R_r versus μ

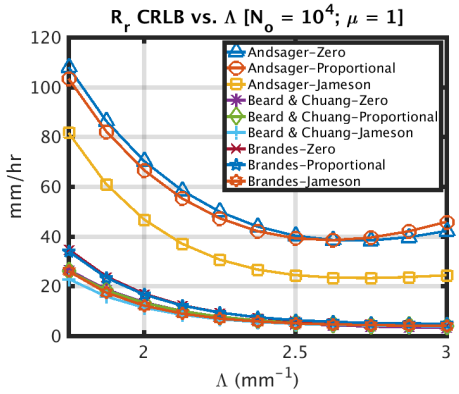

(c) CRLB of R_r versus Λ

Figure 24: CRLB of R_r for different axis ratio models versus each of the DSD parameters.

7.5 CRLB for Different Raindrop Shape Models

To derive the CRLBs of R_r and W, we used (128) - (131), which were derived in Chapter 4 and assume a probabilistic model for the axis ratio of raindrops. This section compares the CRLB of R_r and W for the nine different axis ratio models.

In this section, the CRLB is computed using all the same parameters as described in Section 7.3 except $N_p = 256$, which is within the typical range of the number of pulses used to estimate the dual-pol data products of the WSR-88D [60]. Figures 24 and 25 show the CRLB of R_r and W, respectively, for each of the nine axis ratio models. Each figure contains three plots, each one varying one of the DSD parameters while keeping the other DSD parameters set at their nominal values.

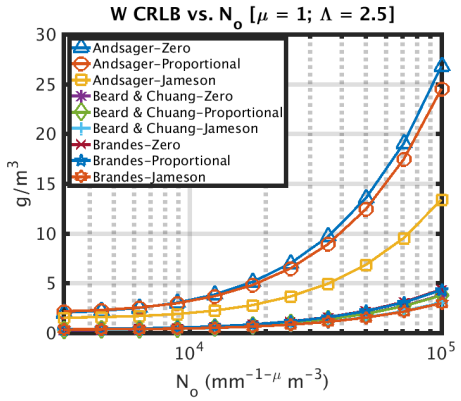

(a) CRLB of W versus N_o

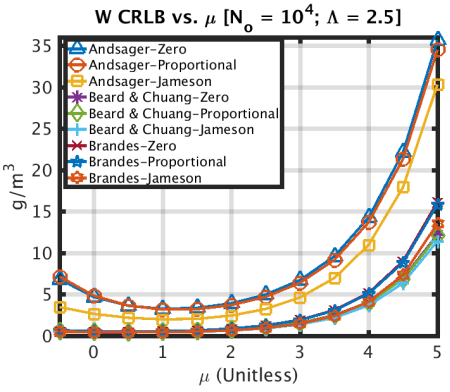

(b) CRLB of W versus μ

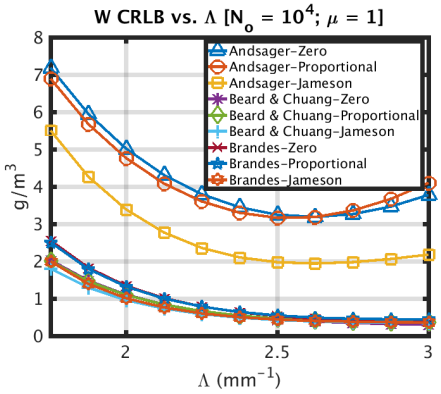

(c) CRLB of W versus Λ

Figure 25: CRLB of W for different axis ratio models versus each of the DSD parameters.

While the general trends of the CRLB are similar for each of the models, the Andsager model for the mean axis ratio of rain drops results in a significantly larger CRLB for both R_r and W. Recall that in Chapter 6 we found that the CRLB of the DSD parameters is largest when using Andsager's model for the mean axis ratio of raindrops. Further, the Andsager model for the mean axis ratio results in the most ill-conditioned Jacobian, which suggests that, under this model, the respective inverse transformation is the most sensitive to radar measurement errors. Given that this model results in the greatest CRLB for the DSD parameters, it is unsurprising to see similar results for rain rate and LWC.

7.6 Analysis of Results

Overall, the analysis of Chapters 5 and 6 suggest that the MLEs of the DSD parameters are biased, have a high standard deviation, and, therefore, have a high RMSE. Based on this fact, it might seem likely that estimators of quantities derived from such parameters (e.g., rain rate and LWC) will inevitably have similar properties. To test this hypothesis, this section strives to summarize the CRLB of R_r and W over the prior distribution of DSD parameters considered standard in the literature, which assumes independent uniform distributions for $\log_{10}(N_w)$, μ, and D_o over the ranges specified in (117). Using this distribution for the DSD parameters, $N_s = 10,000$ random realizations of DSD parameter sets are generated. For each realization, the value of R_r and W are computed along with their respective CRLBs. For two of the axis ratio models, the resulting CRLBs of R_r and W are plotted in Figures 26 and 27, respectively, as a function of their corresponding values. The two axis ratio models shown are the Andsager-Zero model and the Beard and Chuang-Jameson model, which correspond to the worst case (i.e., highest CRLB, in general) and best case (i.e., smallest CRLB, in general) for estimating the quantities of interest.

While the Andsager models result in the highest CRLBs, the other models result in much more desirable bounds on estimation performance. The ability to estimate rain rate and LWC from seemingly poor estimates of the DSD parameters is best understood by performing an eigendecomposition on the inverse FIM of the DSD parameters [36]:

$$J_F^{-1}(X) = \boldsymbol{U}\boldsymbol{\Lambda}_{\boldsymbol{v}}\boldsymbol{U}^T, \tag{204}$$

where $\boldsymbol{U}$ is a unitary matrix such that each column corresponds to an eigenvector and $\boldsymbol{\Lambda}_{\boldsymbol{v}}$ is a diagonal matrix whose entries are the eigenvalues corresponding to each of the eigenvectors of $J_F^{-1}(X)$. The eigenvectors of the inverse FIM correspond to the principle directions of variance, as predicted by the CRLB. The eigenvector, U_3, which corresponds to the minimum eigenvalue, is the principal direction of minimum

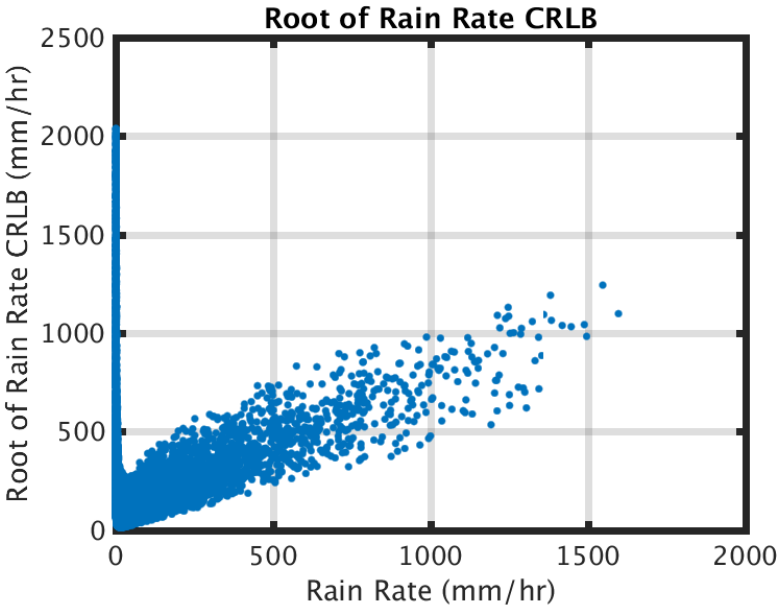

(a) Square root of CRLB of R_r versus R_r for the Andsager - Zero model

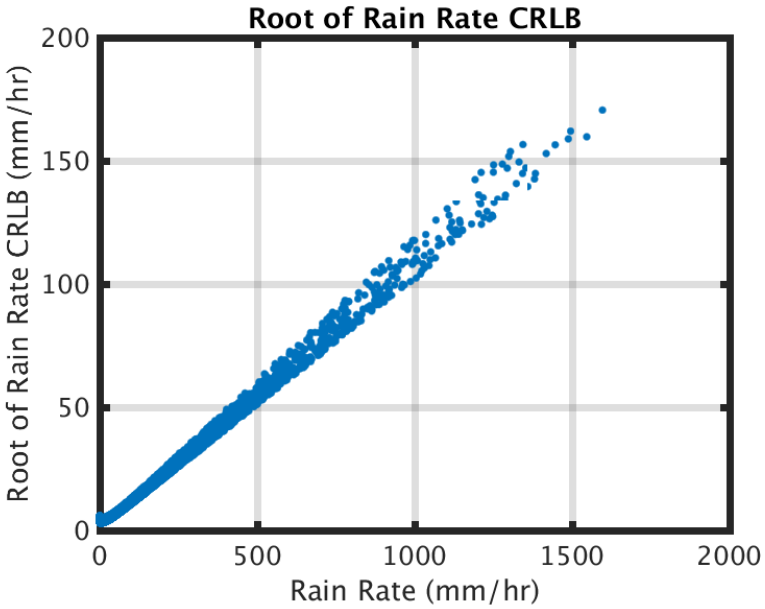

(b) Square root of CRLB of R_r versus R_r for the Beard and Chuang - Jameson model

Figure 26: Square root of CRLB of rain rate versus rain rate evaluated over the specified prior distribution of DSD parameters.

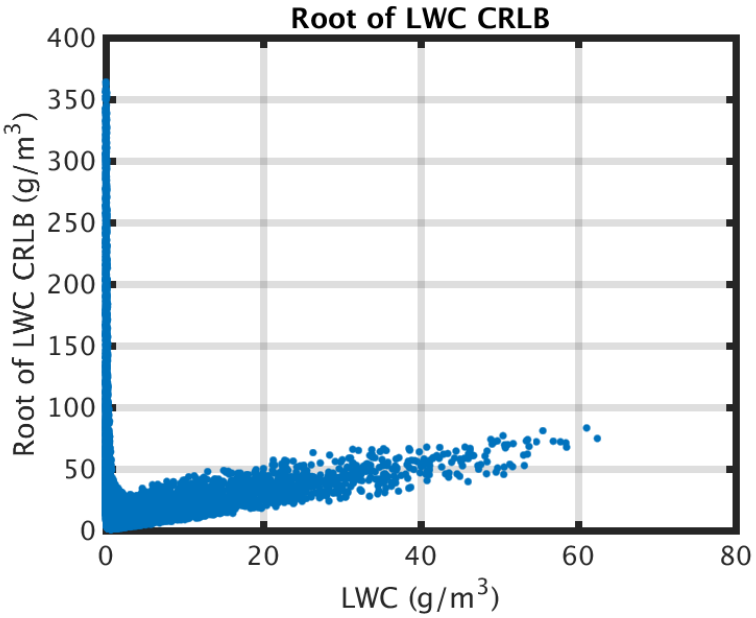

(a) Square root of CRLB of W versus W for the Andsager - Zero model

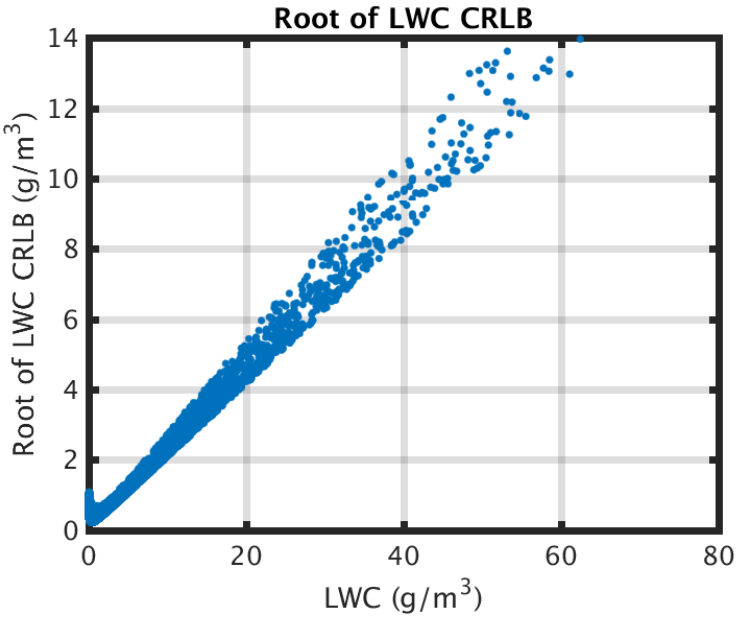

(b) Square root of CRLB of W versus W for the Beard and Chuang - Jameson model

Figure 27: Square root of CRLB of LWC versus LWC evaluated over the specified prior distribution of DSD parameters.

Table 11: Median angle of the Jacobians $\frac{\partial R_r}{\partial X}$ and $\frac{\partial W}{\partial X}$ with respect to the principle direction of minimum variance of the DSD CRLB

Model	med $\left(\angle_{R_r}^{U_3}\right)$	med $\left(\angle_{W}^{U_3}\right)$
Andsager-Zero	3.14	5.42
Andsager-Proportional	3.08	5.33
Andsager-Jameson	3.09	5.38
Beard & Chuang-Zero	2.66	5.05
Beard & Chuang-Proportional	2.76	5.08
Beard & Chuang-Jameson	2.66	4.98
Brandes-Zero	2.84	5.21
Brandes-Proportional	2.72	5.08
Brandes-Jameson	2.78	5.15

variance; i.e., it corresponds to the linear combination of parameters that can be estimated with the smallest variance.

Even if none of the individual DSD parameter estimates have a low variance, correlation of the individual parameter estimates may still permit some function of these parameters to be estimated with a "small" variance if the functional dependence corresponds to the direction of minimum variance. For rain rate, we consider the angle $\angle_{R_r}^{U_3}$, which is the angle between U_3 (i.e., the direction of minimum variance of $J_F^{-1}(X)$) and $\frac{\partial R_r}{\partial X}$. If this angle is small, then estimation of rain rate approximately corresponds to estimating a parameter in the direction of minimum variance. An analogous value, $\angle_{W}^{U_3}$, is considered for LWC. Using the same DSD parameter distribution as before, a Monte Carlo simulation of $N_s = 10,000$ trials is simulated. The median of the angles $\angle_{R_r}^{U_3}$ and $\angle_{W}^{U_3}$ (in degrees) over all Monte Carlo trials, is given in Table 11. For all nine axis ratio models, the dependence of both rain rate and LWC on the DSD parameters closely corresponds to the principal direction of minimum variance of the DSD parameter estimates (as computed using the CRLB), the median angles being within about three and five degrees for rain rate and LWC, respectively.

7.7 Summary

This chapter derived the CRLB of rain rate and LWC. Further, it presented a parametric analysis of the CRLB and MLE for the quantities of interest. The MLEs of both rain rate and LWC were found to be biased with a variance that exceeds the CRLB for a wide range of DSD parameters. Thus, we conclude that an efficient estimator does not exist for either quantity.

The CRLBs of these quantities depend on the model used for the axis ratio of raindrops. Specifically, the Andsager models resulted in much larger CRLBs than the other models. The other models considered all yielded CRLBs similar to each other.

By exploiting the CRLB of the DSD parameters, we demonstrate that rain rate and LWC are nearly proportional to the direction of minimum variance of the estimated DSD parameters for realistic values of the DSD parameters, suggesting that low variance (biased) estimates of rain rate could be possible.

While this chapter examined bounds for an unbiased estimator of rain rate and LWC, it is perfectly reasonable to conclude that better estimator performance (i.e., lower RMSE) could be achieved by incorporating prior knowledge, such as an appropriate prior on the DSD parameters. Many, if not all, methods that have been proposed for estimating these quantities do incorporate such information either explicitly or implicitly. With explicit knowledge of these priors, the work presented here could be expanded upon to establish similar performance bounds for biased estimators based upon these priors [85].

CHAPTER VIII

SUMMARY, CONCLUSIONS, AND FUTURE WORK

8.1 Summary of Contributions

The ultimate objective of this dissertation was to derive the CRLB of the DSD parameters of rain (and clouds), along with the CRLBs of both rain rate and LWC. In all, this dissertation documented a number of original contributions:

- A firm understanding of radar phenomenology, with an emphasis on applications in meteorology, as well as a comprehensive description of the parameters and operation of the WSR-88D were provided in Chapter 2 [70].
- To establish the current state of the field, proposed techniques for estimation of DSD parameters and rain rate were summarized in Chapter 3, along with the methods by which these estimators are usually evaluated.
- Closed-form expressions that approximate the complicated mathematical relationship between the dual-pol radar measurements of an S-band radar and the DSD parameters of rain were developed in Chapter 4. The quality of these approximations were evaluated for the full range of DSD parameters expected to occur in realistic climatological conditions [67].
- Using the closed-form expressions developed in Chapter 4, the CRLB of the DSD parameters of rain was derived in Chapter 5, assuming measurements from an S-band dual-pol radar were provided [69].
- An approach for finding the MLE of the DSD parameters of rain was presented and applied in Chapter 5 to examine the statistics of the MLE of the DSD parameters [69].

- An extensive parametric analysis of the CRLB and MLE statistics of the DSD parameters was performed in Chapter 6. This analysis served to establish the estimator properties as a function of the changing DSD parameters and determine whether an efficient estimator exists for the DSD parameters [68].

- As a natural extension of the previously listed contributions, the CRLB of rain rate and LWC was derived in Chapter 7 [66].

- A parametric analysis of the CRLB of rain rate and LWC is also performed in Chapter 7. Furthermore, the relation of rain rate and LWC to the estimated DSD parameters was examined in detail to discern the utility of the dual-pol measurements for estimation of rain rate and LWC [66].

8.2 Conclusions

Throughout this dissertation, multiple probabilistic models for the shape of raindrops were applied for establishing the relationship between the dual-pol radar measurements and the DSD parameters of rain (or clouds). These models were distinguished by how they define the mean and variance of raindrop axis ratios. Interestingly, while the three different mean axis ratio models differ only slightly over the range of realistic drop sizes, changing the mean axis ratio model significantly impacted the CRLB and MLE variance of the DSD parameters. Using the functional mappings derived in Chapter 4, we found that each of the three dual-pol radar measurements, most often used for DSD and rain rate estimation, relate to the DSD parameters in very similarly ways; i.e., the measurements are redundant with respect to measuring the DSD parameters. Consequently, the functional relationship between the radar measurements and DSD parameters is very sensitive to small changes in the model used to derive such a functional relationship. Futhermore, DSD parameter estimates, such as the MLE, are highly correlated and sensitive to small measurement errors. As a result, the MLE of the DSD parameters has a high variance, in addition to being

biased.

It is known that the radar measurements are efficient estimators for the parameters of the received radar signal. However, given the nonlinear transformation required to go from the radar measurements to the DSD parameters, rain rate, or LWC, the existence of an efficient estimator for each of these quantities is not guaranteed. By examining the properties of the MLE for each of these quantities, we confirmed that an efficient estimator does not exist for the DSD parameters, rain rate, or LWC. This was evidenced by the fact the MLE is both biased and frequently has a variance that exceeds the CRLB.

While an efficient estimator does not exist for the DSD parameters, rain rate, or LWC, the CRLB is still an excellent tool for determining the efficacy of the dual-pol radar measurements for estimating each of these quantities, especially in the absence of additional information that could be incorporated into the estimators. Thus, we used the CRLB to infer how useful the measurements might be in forming a biased estimator for rain rate or LWC. By applying an eigendecomposition to the inverse FIM of the DSD parameters and, then, comparing the direction of minimum variance (as predicted by the CRLB) to the gradient of rain rate (or LWC) with respect the DSD parameters, we found that very often rain rate (and LWC) estimation approximately corresponds to estimating a parameter in the direction of minimum variance that results when estimating the DSD parameters. As a result, poor estimation of the DSD parameters does not necessarily imply that poor estimation of rain rate or LWC is inevitable. As a matter of fact, it may be possible to estimate rain rate and LWC quite well.

8.3 Future Work

While this dissertation focuses on establishing performance bounds for unbiased estimators of DSD parameters, rain rate, and LWC, it also provides a starting point for

establishing similar bounds for biased estimators of these quantities, more specifically estimators that incorporate prior distributions on the DSD parameters. Establishing such a bound is extremely relevant in the context of many of the estimation techniques that were discussed in Chapter 3, as a vast array of these approaches assume a specific prior distribution on the DSD parameters, and their performance is inherently dependent on the selection of these priors. The Bayesian Cramér-Rao Lower Bound (BCRLB), also known as the posterior CRLB, establishes a bound on the MMSE of an estimator, $\hat{X}$, given a prior distribution, $p_X(X)$, on the unknown parameters [86]. Unlike the CRLB, the BCRLB makes no assumptions regarding the estimator bias.

Another avenue of research, related to this dissertation, that could also be explored is the computation of the CRLBs of the DSD parameters, rain rate, and LWC when using the CC (correlation coefficient) for estimation in place of one of the other radar measurements. The CC has long been discarded in these types of estimation problems due to its lack of variation when observing rain. However, given the singular nature of the other three radar measurements (as they relate to the DSD parameters), it may be advisable to consider the CC as a measurement that may provide information related to the DSD parameters that is not availabe from the other three radar measurements.

Lastly, the signal model employed in this dissertation ignores the impact of thermal noise. It would be a fairly straightforward extension to compute the CRLBs of the DSD parameters, rain rate, and LWC in the presence of thermal noise. While most estimation and inference algorithms that use the dual-pol data products only assume reliable performance for high SNRs, WSR-88D specifications require some of the more traditional single-polarization data products to be estimated at SNRs as low as -3 dB [91]. Thus, computing the CRLBs in the presence of thermal noise could provide the necessary information for determining at what SNRs such estimators would break down and become unreliable.

APPENDIX A

TABLES OF COEFFICIENTS

The tables in this section list the coefficients found in Chapter 4, along with the associated CDs as a metric for how well the axis ratio integrals are approximated. For all tables in this section, the mean models (MM) of Andsager, Beard and Chuang, and Brandes are denoted A, B&C, and B, respectively. Additionally the standard deviation models (SDM) are denoted as Z, P, and J for the zero, proportional, and Jameson models, respectively.

Table 12: Coefficients for axis ratio integral of horizontal reflectivity (ζ_h)

		LLSE Results				NLSE Results			
MM	SDM	a_h	b_h	c_h	CD	a_h	b_h	c_h	CD
A	Z	256.3690	5.9517	-0.0945	1.00	227.5522	6.0628	-0.0842	1.00
A	P	257.4120	5.9516	-0.0949	1.00	228.3439	6.0635	-0.0844	1.00
A	J	251.6199	5.9324	-0.1132	1.00	321.6675	5.2318	-0.2904	1.00
B&C	Z	260.5043	5.9613	-0.0892	1.00	256.2449	5.8922	-0.1155	1.00
B&C	P	261.5808	5.9611	-0.0895	1.00	257.2455	5.8922	-0.1158	1.00
B&C	J	255.7883	5.9422	-0.1078	1.00	362.0713	5.0624	-0.3213	1.00
B	Z	252.4484	5.9442	-0.1076	1.00	287.1870	5.5047	-0.2238	1.00
B	P	253.4640	5.9440	-0.1080	1.00	288.3833	5.5038	-0.2244	1.00
B	Jn	246.2604	5.9213	-0.1302	1.00	554.1162	4.0525	-0.5681	1.00

Table 13: Coefficients for axis ratio integral of vertical reflectivity (ζ_v)

		LLSE Results				NLSE Results			
MM	SDM	a_v	b_v	c_v	CD	a_v	b_v	c_v	CD
A	Z	328.4393	6.0633	0.1449	1.00	438.3372	5.5511	0.0403	1.00
A	P	329.7509	6.0635	0.1452	1.00	440.3782	5.5501	0.0404	1.00
A	J	328.1304	6.0559	0.1391	1.00	442.8122	5.4861	0.0180	1.00
B&C	Z	319.1734	6.0466	0.1354	1.00	359.0418	5.8398	0.0934	1.00
B&C	P	320.4272	6.0467	0.1357	1.00	360.5492	5.8394	0.0936	1.00
B&C	J	318.9078	6.0393	0.1296	1.00	363.3282	5.7722	0.0706	1.00
B	Z	333.2497	6.0695	0.1597	1.00	349.4382	6.0930	0.1780	1.00
B	P	334.5912	6.0697	0.1601	1.00	350.8991	6.0931	0.1784	1.00
B	J	332.8017	6.0619	0.1537	1.00	355.2631	6.0124	0.1519	1.00

Table 14: Coefficients for axis ratio integral of specific differential phase (K_{DP})

		LLSE Results				NLSE Results			
MM	SDM	a_k	b_k	c_k	CD	a_k	b_k	c_k	CD
A	Z	7.9868E-11	6.1890	0.4072	1.00	6.1461E-11	6.1515	0.3384	1.00
A	P	5.6218E-11	4.2183	-0.3232	0.84	6.3169E-11	6.1255	0.3343	1.00
A	J	6.5890E-11	3.6867	-0.4669	0.84	6.8909E-11	5.8058	0.2411	1.00
B&C	Z	1.1816E-10	6.0304	0.4326	0.99	1.3258E-10	5.0207	0.1282	1.00
B&C	P	8.5074E-11	4.3364	-0.2018	0.91	1.3556E-10	5.0024	0.1255	1.00
B&C	J	9.3758E-11	3.8128	-0.3572	0.90	1.4560E-10	4.7082	0.0374	1.00
B	Z	5.2569E-11	4.7155	-0.1988	0.87	1.1432E-10	5.0037	0.0751	1.00
B	P	6.1092E-11	4.1287	-0.3571	0.84	1.1698E-10	4.9842	0.0723	1.00
B	J	6.9166E-11	3.6752	-0.4839	0.85	1.3380E-10	4.5447	-0.0502	1.00

Table 15: Coefficients for axis ratio integral of the CC (ρ)

		LLSE Results				NLSE Results			
MM	SDM	a_ρ	b_ρ	c_ρ	CD	a_ρ	b_ρ	c_ρ	CD
A	Z	290.1752	6.0075	0.0252	1.00	315.8734	5.8066	-0.0221	1.00
A	P	290.4194	6.0075	0.0251	1.00	316.1178	5.8065	-0.0221	1.00
A	J	289.1973	6.0038	0.0216	1.00	329.2323	5.6919	-0.0523	1.00
B&C	Z	288.3506	6.0039	0.0231	1.00	304.8260	5.8581	-0.0126	1.00
B&C	P	288.5963	6.0039	0.0230	1.00	305.0905	5.8579	-0.0127	1.00
B&C	J	287.4028	6.0003	0.0195	1.00	318.1277	5.7415	-0.0432	1.00
B	Z	290.0488	6.0069	0.0261	1.00	315.0238	5.8076	-0.0212	1.00
B	P	290.2888	6.0068	0.0260	1.00	315.3300	5.8071	-0.0214	1.00
B	J	288.7690	6.0026	0.0219	1.00	339.8175	5.6193	-0.0684	1.00

APPENDIX B

GOODNESS OF FIT OF APPROXIMATIONS

These plots illustrate the goodness of fit of the data product approximations developed in Chapter 4. For the range of DSD parameters specified in (117), the value of the resulting approximation for each of the data products is plotted versus the exact value that is obtained via numerical integration.

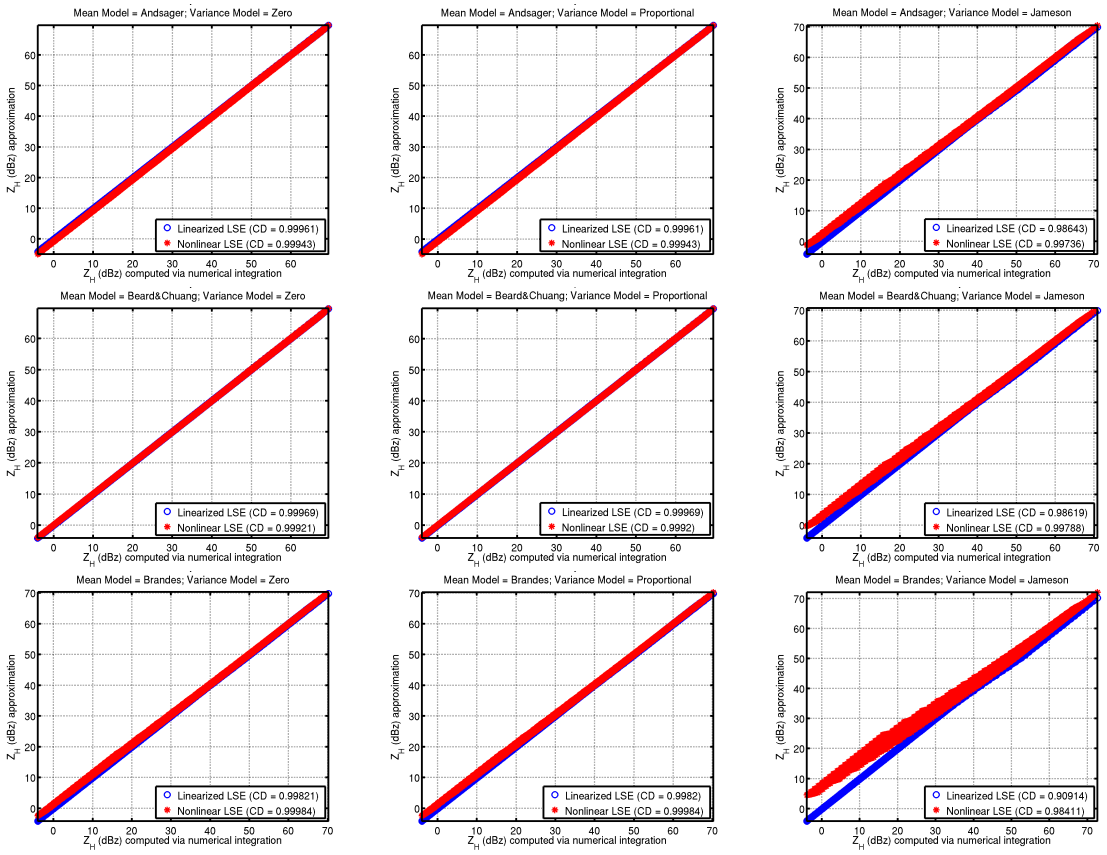

Figure 28: Goodness of fit of approximation for horizontal reflectivity (Z_H) for different axis ratio models

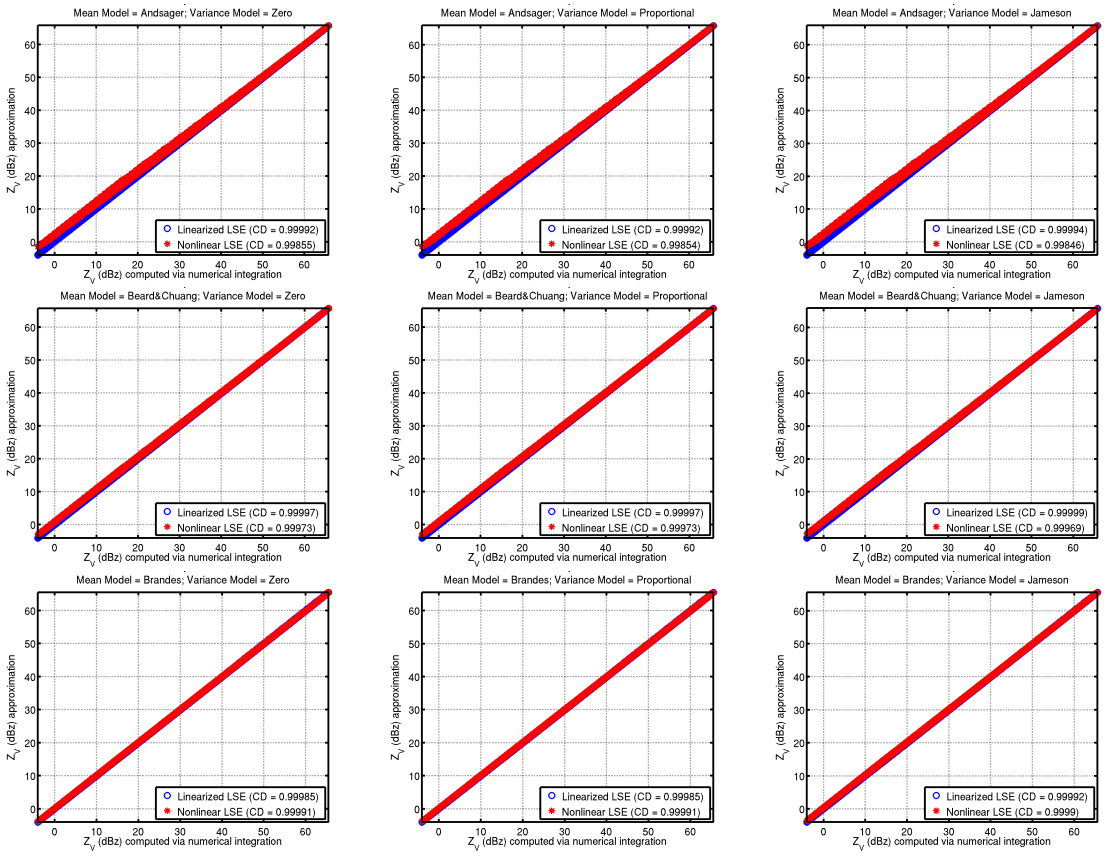

Figure 29: Goodness of fit of approximation for vertical reflectivity (Z_V) for different axis ratio models

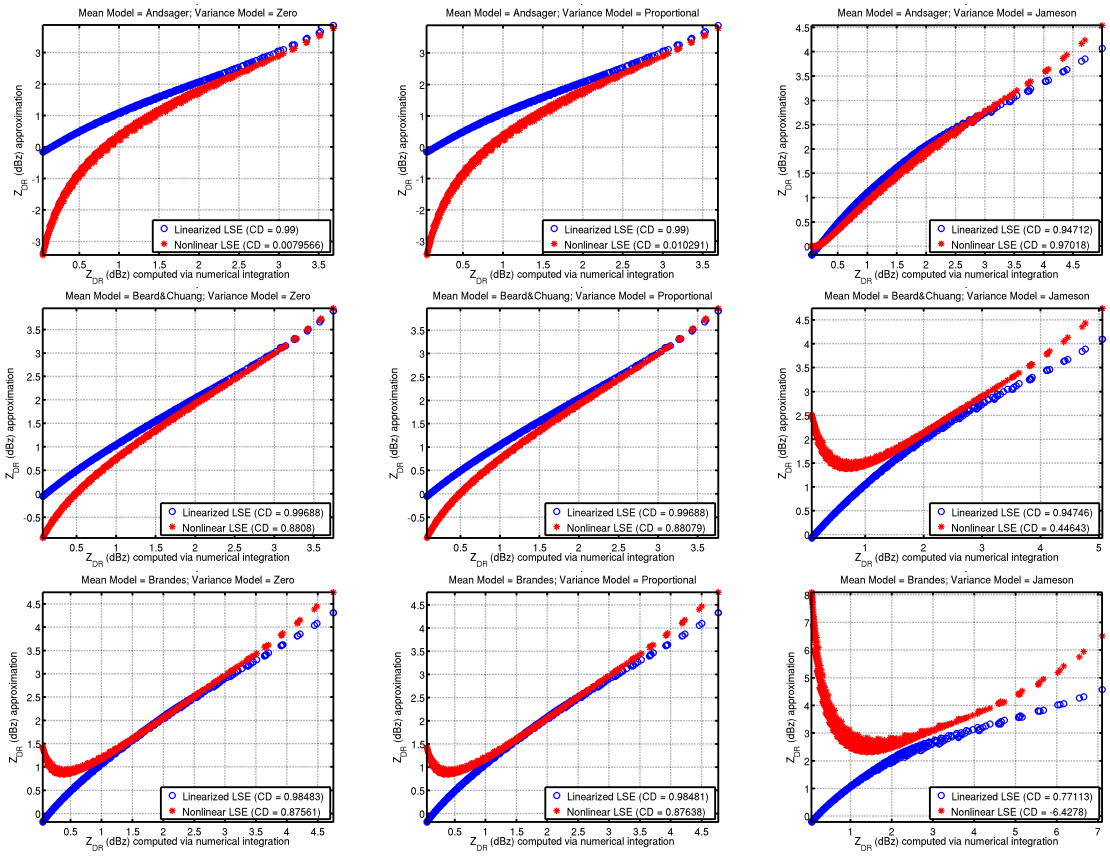

Figure 30: Goodness of fit of approximation for differential reflectivity (Z_{DR}) for different axis ratio models

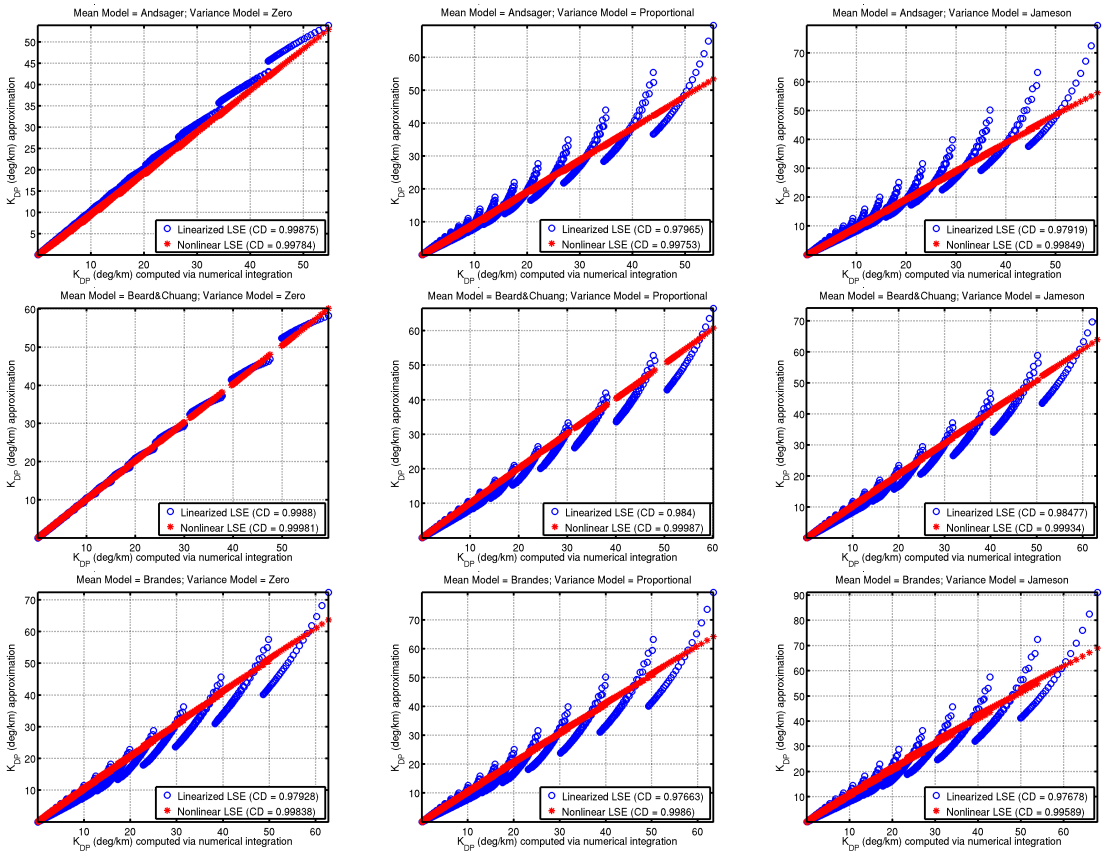

Figure 31: Goodness of fit of approximation for specific differential phase (K_{DP}) for different axis ratio models

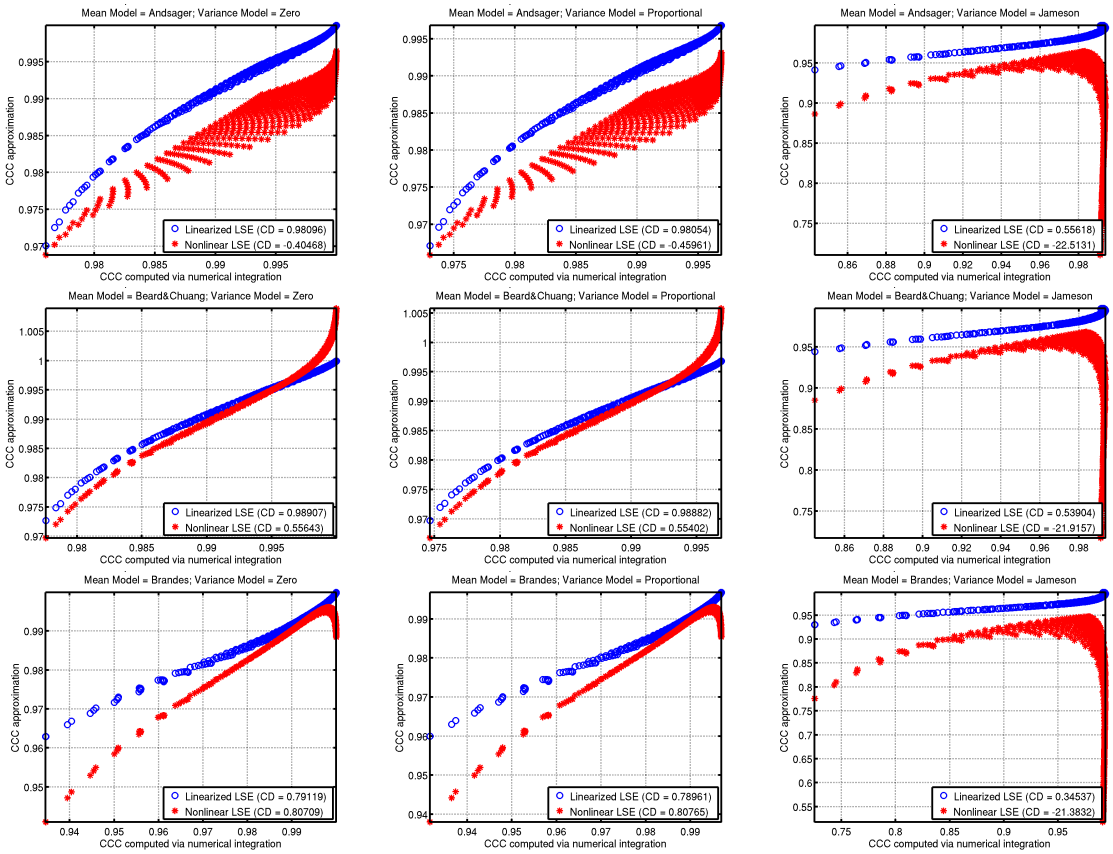

Figure 32: Goodness of fit of approximation for the CC (ρ) for different axis ratio models

REFERENCES

[1] "IEEE standard radar definitions," *IEEE Std 686-2008 (Revision of IEEE Std 686-1997)*, pp. 1–41, 2008.

[2] Anagnostou, M. N., Anagnostou, E. N., Vivekanandan, J., and Ogden, F. L., "Comparison of two raindrop size distribution retrieval algorithms for X-band dual-polarization observations," *Journal of Hydrometeorology*, vol. 9, no. 3, pp. 589–600, 2008.

[3] Andsager, K., Beard, K. V., and Laird, N. F., "Laboratory measurements of axis ratios for large raindrops," *Journal of the Atmospheric Sciences*, vol. 56, no. 15, pp. 2673–2683, 1999.

[4] Battan, L. J., *Radar Observation of the Atmosphere*. The University of Chicago Press, 1973.

[5] Beard, K. V. and Chuang, C., "A new model for the equilibrium shape of raindrops," *Journal of the Atmospheric Sciences*, vol. 44, no. 11, pp. 1509–1524, 1987.

[6] Beard, K. and Jameson, A., "Raindrop canting," *Journal of the Atmospheric Sciences*, vol. 40, no. 2, pp. 448–454, 1983.

[7] Bianchi, B., Jan van Leeuwen, P., Hogan, R. J., and Berne, A., "A variational approach to retrieve rain rate by combining information from rain gauges, radars, and microwave links," *Journal of Hydrometeorology*, vol. 14, no. 6, pp. 1897–1909, 2013.

[8] Brandes, E. A., Ryzhkov, A. V., and Zrnic, D. S., "An evaluation of radar rainfall estimates from specific differential phase," *Journal of Atmospheric and Oceanic Technology*, vol. 18, no. 3, pp. 363–375, 2001.

[9] Brandes, E. A., Zhang, G., and Vivekanandan, J., "Experiments in rainfall estimation with a polarimetric radar in a subtropical environment," *Journal of Applied Meteorology*, vol. 41, no. 6, pp. 674–685, 2002.

[10] Brandes, E. A., Zhang, G., and Vivekanandan, J., "An evaluation of a drop distribution-based polarimetric radar rainfall estimator," *Journal of Applied Meteorology*, vol. 42, no. 5, pp. 652–660, 2003.

[11] Brandes, E. A., Zhang, G., and Vivekanandan, J., "Comparison of polarimetric radar drop size distribution retrieval algorithms," *Journal of Atmospheric and Oceanic Technology*, vol. 21, no. 4, pp. 584–598, 2004.

[12] Brandes, E. A., Zhang, G., and Vivekanandan, J., "Drop size distribution retrieval with polarimetric radar: Model and application," *Journal of Applied Meteorology*, vol. 43, no. 3, pp. 461–475, 2004.

[13] Bringi, V., Huang, G.-J., Chandrasekar, V., and Gorgucci, E., "A methodology for estimating the parameters of a gamma raindrop size distribution model from polarimetric radar data: Application to a squall-line event from the TRMM/Brazil campaign," *Journal of Atmospheric and Oceanic Technology*, vol. 19, no. 5, pp. 633–645, 2002.

[14] Bringi, V. N., Chandrasekar, V., and Xiao, R., "Raindrop axis ratios and size distributions in Florida rainshafts: An assessment of multiparameter radar algorithms," *Geoscience and Remote Sensing, IEEE Transactions on*, vol. 36, no. 3, pp. 703–715, 1998.

[15] Bringi, V. and Chandrasekar, V., *Polarimetric Doppler Weather Radar: Principles and applications*. Cambridge University Press, 2001.

[16] Bringi, V., Tang, T., and Chandrasekar, V., "Evaluation of a new polarimetrically based Z-R relation," *Journal of Atmospheric and Oceanic Technology*, vol. 21, no. 4, pp. 612–623, 2004.

[17] Brown, R. A., Flickinger, B. A., Forren, E., Schultz, D. M., Sirmans, D., Spencer, P. L., Wood, V. T., and Ziegler, C. L., "Improved detection of severe storms using experimental fine-resolution WSR-88D measurements," *Weather and Forecasting*, vol. 20, no. 1, pp. 3–14, 2005.

[18] Brown, R. A., Wood, V. T., and Sirmans, D., "Improved tornado detection using simulated and actual WSR-88D data with enhanced resolution," *Journal of Atmospheric and Oceanic Technology*, vol. 19, no. 11, pp. 1759–1771, 2002.

[19] Browning, K. and Wexler, R., "The determination of kinematic properties of a wind field using Doppler radar," *Journal of Applied Meteorology*, vol. 7, no. 1, pp. 105–113, 1968.

[20] Calheiros, R. and Zawadzki, I., "Reflectivity-rain rate relationships for radar hydrology in Brazil," *Journal of Climate and Applied Meteorology*, vol. 26, no. 1, pp. 118–132, 1987.

[21] Cao, Q., Zhang, G., Brandes, E. A., and Schuur, T. J., "Polarimetric radar rain estimation through retrieval of drop size distribution using a Bayesian approach," *Journal of Applied Meteorology and Climatology*, vol. 49, no. 5, pp. 973–990, 2010.

[22] Cao, Q., Zhang, G., and Xue, M., "A variational approach for retrieving raindrop size distribution from polarimetric radar measurements in the presence of attenuation," *Journal of Applied Meteorology and Climatology*, vol. 52, no. 1, pp. 169–185, 2013.

[23] Chandrasekar, V., Gorgucci, E., and Scarchilli, G., "Optimization of multiparameter radar estimates of rainfall," *Journal of Applied Meteorology*, vol. 32, no. 7, pp. 1288–1293, 1993.

[24] Doviak, R., "Comparison of weather and aircraft surveillance radar to determine key features for a MPAR (A basis for a cylindrical polarimetric phase array radar design)," tech. rep., The National Severe Storms Laboratory, 2014.

[25] Doviak, R. J. and Zrnic, D. S., *Doppler Radar and Weather Observations*. Academic Press, second ed., 1993.

[26] Doviak, R. J., Zrnic, D. S., and Sirmans, D. S., "Doppler weather radar," *Proceedings of the IEEE*, vol. 67, no. 11, pp. 1522–1553, 1979.

[27] Goodman, J., *Statistical Optics*. New York: Wiley, 1985.

[28] Gorgucci, E., Scarchilli, G., and Chandrasekar, V., "A robust estimator of rainfall rate using differential reflectivity," *Journal of Atmospheric and Oceanic Technology*, vol. 11, pp. 586–592, 1994.

[29] Gorgucci, E., Chandrasekar, V., Bringi, V., and Scarchilli, G., "Estimation of raindrop size distribution parameters from polarimetric radar measurements," *Journal of the Atmospheric Sciences*, vol. 59, no. 15, pp. 2373–2384, 2002.

[30] Gorgucci, E., Chandrasekar, V., and Scarchilli, G., "Radar and surface measurement of rainfall during CaPE: 26 July 1991 case study," *Journal of Applied Meteorology*, vol. 34, no. 7, pp. 1570–1577, 1995.

[31] Gorgucci, E., Scarchilli, G., Chandrasekar, V., and Bringi, V., "Measurement of mean raindrop shape from polarimetric radar observations," *Journal of the Atmospheric Sciences*, vol. 57, no. 20, pp. 3406–3413, 2000.

[32] Gorgucci, E., Scarchilli, G., Chandrasekar, V., and Bringi, V., "Rainfall estimation from polarimetric radar measurements: Composite algorithms immune to variability in raindrop shape-size relation," *Journal of Atmospheric and Oceanic Technology*, vol. 18, no. 11, pp. 1773–1786, 2001.

[33] Green, A., "An approximation for the shapes of large raindrops," *Journal of Applied Meteorology*, vol. 14, no. 8, pp. 1578–1583, 1975.

[34] Gunn, R. and Kinzer, G. D., "The terminal velocity of fall for water droplets in stagnant air," *Journal of Meteorology*, vol. 6, no. 4, pp. 243–248, 1949.

[35] Hastie, T., Tibshirani, R., and Friedman, J., *The Elements of Statistical Learning: Data Mining, Inference, and Prediction*. Springer Series in Statistics, 2001.

[36] Hayes, M. H., *Statistical Digital Signal Processing and Modeling*. John Wiley & Sons, 1996.

[37] Holt, A., "Some factors affecting the remote sensing of rain by polarization diversity radar in the 3- to 35-GHz frequency range," *Radio Science*, vol. 19, no. 5, pp. 1399–1412, 1984.

[38] Ice, R., "Private communication." 2014.

[39] (JAG/PARP), J. A. G. F. P. A. R. P., "Federal research and development needs and priorities for phased array radar," tech. rep., Office of the Federal Coordinator for Meteorological Services and Supporting Research, 2006.

[40] Jameson, A., "Microphysical interpretation of multi-parameter radar measurements in rain. Part I: Interpretation of polarization measurements and estimation of raindrop shapes," *Journal of the Atmospheric Sciences*, vol. 40, no. 7, pp. 1792–1802, 1983.

[41] Jameson, A., "The interpretation and meteorological application of radar backscatter amplitude ratios at linear polarizations," *Journal of Atmospheric and Oceanic Technology*, vol. 6, no. 6, pp. 908–919, 1989.

[42] Jameson, A. and Mueller, E., "Estimation of propagation-differential phase shift from sequential orthogonal linear polarization radar measurements," *Journal of Atmospheric and Oceanic Technology*, vol. 2, no. 2, pp. 133–137, 1985.

[43] Jameson, A., "Microphysical interpretation of multiparameter radar measurements in rain. Part III: Interpretation and measurement of propagation differential phase shift between orthogonal linear polarizations," *Journal of the Atmospheric Sciences*, vol. 42, no. 6, pp. 607–614, 1985.

[44] Janssen, L. H., Van Der Spek, G., and others, "The shape of Doppler spectra from precipitation," *Aerospace and Electronic Systems, IEEE Transactions on*, no. 2, pp. 208–219, 1985.

[45] Kay, S. M., *Fundamentals of Statistical Signal Processing: Estimation Theory*. Prentice Hall Signal Processing Series, 1993.

[46] Kumjian, M. R., "Principles and applications of dual-polarization weather radar. Part I: Description of the polarimetric radar variables," *Journal of Operational Meteorology*, vol. 1, no. 19, pp. 226–242, 2013.

[47] Kumjian, M. R., "Principles and applications of dual-polarization weather radar. Part II: Warm and cold season applications," *Journal of Operational Meteorology*, vol. 1, pp. 243–264, 2013.

[48] Kumjian, M. R., "Principles and applications of dual-polarization weather radar. Part III: Artifacts," *Journal of Operational Meteorology*, vol. 1, pp. 266–274, 2013.

[49] Laboratory, T. N. S. S., "Research tools: Multi-function phased array radar." http://www.nssl.noaa.gov/tools/radar/mpar/, January 2016.

[50] Lagarias, J., Reeds, J., Wright, M., and Wright, P., "Convergence properties of the Nelder-Mead simplex search method in low dimensions," *SIAM Journal of Optimization*, vol. 9, no. 1, pp. 112–147, 1998.

[51] Li, Z., Ligthart, L., Huang, P., Lu, W., van der Zwan, W., and Krasnov, O., "Simulation of the PARSAX dual-channel FMCW polarimetric agile radar system," in *Radar Conference (EuRAD), 2010 European*, pp. 168–171, IEEE, 2010.

[52] Liu, H., Chandrasekar, V., and Xu, G., "An adaptive neural network scheme for radar rainfall estimation from WSR-88D observations," *Journal of Applied Meteorology*, vol. 40, no. 11, pp. 2038–2050, 2001.

[53] Marshall, J. and Palmer, W., "The distribution of raindrops with size," *Journal of Meteorology*, vol. 5, pp. 165–166, 1948.

[54] Melnikov, V., Zrnic, D., Doviak, R., and Carter, J., "Calibration and performance analysis of NSSLs polarimetric WSR-88D," *NOAA/NSSL Rep*, vol. 77, 2003.

[55] Mishchenko, M. I., Travis, L. D., and Mackowski, D. W., "T-matrix computations of light scattering by nonspherical particles: a review," *Journal of Quantitative Spectroscopy and Radiative Transfer*, vol. 55, no. 5, pp. 535–575, 1996.

[56] Mudukutore, A. S., Chandrasekar, V., and Keeler, R. J., "Pulse compression for weather radars," *Geoscience and Remote Sensing, IEEE Transactions on*, vol. 36, no. 1, pp. 125–142, 1998.

[57] Naishadham, K., *Principles of Modern Radar: Advanced Techniques*, ch. 2: Introduction to Radar Polarimetry, pp. 589–629. SciTech Publishing, 2013.

[58] NOAA's National Weather Service Radar Operations Center, "NEXRAD network sites." https://www.roc.noaa.gov/wsr88d/Program/NetworkSites.aspx, Jan. 2016.

[59] NOAA's NWS ROC, "WSR-88D dual polarization background and status." http://roc.noaa.gov/WSR88D/dualpol/DualPolOverview.aspx, Sept 2014.

[60] Office of the Federal Coordinator for Meteorological Services and Supporting Research, *Federal Meteorological Handbook No. 11, Doppler Radar Meteorological Observations: Part B, Doppler Radar Theory and Meteorology*. U.S. Department of Commerce / National Oceanic and Atmospheric Administration, 2005.

[61] Office of the Federal Coordinator for Meteorological Services and Supporting Research, *Federal Meteorological Handbook No. 11, Doppler Radar Meteorological Observations: Part D WSR-88D Unit Description and Operational Applications.* U.S. Department of Commerce / National Oceanic and Atmospheric Administration, 2006.

[62] Office of the Federal Coordinator for Meteorological Services and Supporting Research", *Federal Meteorological Handbook No. 11, Doppler Radar Meteorological Observations: Part A System Concepts, Responsiblities, and Procedures.* U.S. Department of Commerce / National Oceanic and Atmospheric Administration, 2013.

[63] Office of the Federal Coordinator for Meteorological Services and Supporting Research, *Federal Meteorological Handbook No. 11, Doppler Radar Meteorological Observations: Part C WSR-88D Products and Algorithms.* U.S. Department of Commerce / National Oceanic and Atmospheric Administration, 2013.

[64] Oguchi, T., "Electromagnetic wave propagation and scattering in rain and other hydrometeors," *Proceedings of the IEEE*, vol. 71, no. 9, pp. 1029–1078, 1983.

[65] Pruppacher, H. and Beard, K., "A wind tunnel investigation of the internal circulation and shape of water drops falling at terminal velocity in air," *Quarterly Journal of the Royal Meteorological Society*, vol. 96, no. 408, pp. 247–256, 1970.

[66] Reed, J. L. and Lanterman, A. D., "CRLB of rain rate and liquid water content," *IEEE Transactions on Aerospace and Electronic Systems*, submitted for publication.

[67] Reed, J. L. and Lanterman, A. D., "Mapping drop size distribution parameters to radar measurements," *IEEE Transactions on Aerospace and Electronic Systems*, submitted for publication.

[68] Reed, J. L. and Lanterman, A. D., "Parametric analysis of CRLB and MLE of DSD parameters," *IEEE Transactions on Aerospace and Electronic Systems*, submitted for publication.

[69] Reed, J. L. and Lanterman, A. D., "Variance bounds for estimation of drop size distribution parameters," *IEEE Transactions on Aerospace and Electronic Systems*, submitted for publication.

[70] Reed, J. L., Lanterman, A. D., and Trostel, J. M., "Operation and phenomenology of the NEXRAD (WSR-88D) weather radar," *IEEE Aerospace and Electronics Systems Magazine*, to be published.

[71] Richards, M. A., *Fundamentals of Radar Signal Processing.* McGraw-Hill, 2 ed., 2014.

[72] Richards, M. A., Scheer, J. A., and Holm, W. A., eds., *Principles of Modern Radar: Basic Principles*. SciTech Publishing, 2010.

[73] Richards, W. and Crozier, C., "Precipitation measurement with a C-band weather radar in southern ontario," *Atmosphere-Ocean*, vol. 21, no. 2, pp. 125–137, 1983.

[74] Rosenfeld, D., Wolff, D. B., and Amitai, E., "The window probability matching method for rainfall measurements with radar," *Journal of Applied Meteorology*, vol. 33, no. 6, pp. 682–693, 1994.

[75] Sachidananda, M. and Zrnic, D., "Rain rate estimates from differential polarization measurements," *Journal of Atmospheric and Oceanic Technology*, vol. 4, no. 4, pp. 588–598, 1987.

[76] Schulz, T. J. and Kostinski, A., "Variance bounds on the estimation of reflectivity and polarization parameters in radar meteorology," *Geoscience and Remote Sensing, IEEE Transactions on*, vol. 35, no. 2, pp. 248–255, 1997.

[77] Seliga, T. and Bringi, V., "Potential use of radar differential reflectivity measurements at orthogonal polarizations for measuring precipitation," *Journal of Applied Meteorology*, vol. 15, no. 1, pp. 69–76, 1976.

[78] Sirmans, D. and Doviak, R., "NOAA technical memorandum ERL NSSL 64, meteorological radar signal intensity estimation," tech. rep., National Severe Storms Laboratory, 1973.

[79] Skolnik, M. I., ed., *Radar Handbook*. McGraw-Hill, 1990.

[80] Strang, G., *Linear Algebra and its Applications*. Harcourt College Publishers, third ed., 1988.

[81] Testud, J., Oury, S., Black, R. A., Amayenc, P., and Dou, X., "The concept of normalized distribution to describe raindrop spectra: A tool for cloud physics and cloud remote sensing," *Journal of Applied Meteorology*, vol. 40, no. 6, pp. 1118–1140, 2001.

[82] Trostel, J., *Principles of Modern Radar. Volume III: Radar Applications*, ch. 13. Raleigh, NC, USA: SciTech Publishing, 2014.

[83] Ulbrich, C. W., "Natural variations in the analytical form of the raindrop size distribution," *Journal of Climate and Applied Meteorology*, vol. 22, no. 10, pp. 1764–1775, 1983.

[84] van de Hulst, H., *Light Scattering by Small Particles*. Dover Publications, Inc., 1981.

[85] Van Trees, H. L., *Detection, Estimation, and Modulation Theory, Part III: Radar-Sonar Signal Processing and Gaussian Signals in Noise*. New York: Wiley, 1968.

[86] Van Trees, H. and Bell, K., *Bayesian Bounds for Parameter Estimation and Nonlinear Filtering/Tracking*. Wiley-IEEE Press, 2007.

[87] van Zyl, J. and Kim, Y., *Synthetic Aperture Radar*. John Wiley and Sons, Inc., 2011.

[88] Vulpiani, G., Marzano, F. S., Chandrasekar, V., Berne, A., and Uijlenhoet, R., "Polarimetric weather radar retrieval of raindrop size distribution by means of a regularized artificial neural network," *Geoscience and Remote Sensing, IEEE Transactions on*, vol. 44, no. 11, pp. 3262–3275, 2006.

[89] Weber, M. E., Cho, J. Y., Herd, J. S., Flavin, J. M., Benner, W. E., and Torok, G. S., "The next-generation multimission US surveillance radar network," *Bulletin of the American Meteorological Society*, vol. 88, no. 11, pp. 1739–1751, 2007.

[90] Willis, P. T., "Functional fits to some observed drop size distributions and parameterization of rain," *Journal of the Atmospheric Sciences*, vol. 41, no. 9, pp. 1648–1661, 1984.

[91] WSR-88D Radar Operations Center, "WSR-88D system specification," tech. rep., WSR-88D Radar Operations Center, 2001.

[92] Xiao, R. and Chandrasekar, V., "Development of a neural network based algorithm for rainfall estimation from radar observations," *Geoscience and Remote Sensing, IEEE Transactions on*, vol. 35, no. 1, pp. 160–171, 1997.

[93] Zhang, G., Sun, J., and Brandes, E. A., "Improving parameterization of rain microphysics with disdrometer and radar observations," *Journal of the Atmospheric Sciences*, vol. 63, no. 4, pp. 1273–1290, 2006.

[94] Zhang, G., Vivekanandan, J., and Brandes, E., "A method for estimating rain rate and drop size distribution from polarimetric radar measurements," *Geoscience and Remote Sensing, IEEE Transactions on*, vol. 39, no. 4, pp. 830–841, 2001.

[95] Zrnić, D., "Spectrum width estimates for weather echoes," *Aerospace and Electronic Systems, IEEE Transactions on*, no. 5, pp. 613–619, 1979.

VITA

Jenny Reed graduated *summa cum laude* with her B.S. degree in Electrical Engineering from Florida Atlantic University (FAU) in 2006 and graduated with highest honors with her M.S. degree in Electrical and Computer Engineering (ECE) from the Georgia Institute of Technology (GIT) in 2007. She began her career at the Georgia Tech Research Institute (GTRI) in 2008 as a Research Engineer I. In 2011, she was promoted to Research Engineer II, and, in 2015, she was promoted to Senior Research Engineer. Her work at GTRI includes radar digital signal processing; data analysis; modeling and simulation; meteorological radar applications; electronic protection; algorithm development; radar performance analysis and assessment; ground, airborne, and surface moving target indication; and data fusion and integration.